EUROPEAN COMMISSION

Community Research

NF-PRO

Contract Number: FI6W-CT-2003-02389

DELIVERABLE (D-N°:2.5.9)

Author(s): Georg Houben

Reporting period: e.g. **2004-2006**

Date of issue of this report: **2006/09/29**

Version : **final**

NF-PRO RTD Component: 1

NF-PRO Work Package : WP 2.5

Start date of project : **01/01/2004** Duration : 48 Months

	Name	Date	Signature for approval
Author[1]:	Georg Houben	Sept 29, 2006	
Verified by[2]:			
Approved by[3]:			
Verified by RTD Leader			

[1] Name and signature of the person responsible for drafting the deliverable

[2] Name and signature of the reviewer (member of applicable Work Package)

[3] Name and signature of the Work Package Leader

[4] Name of the RTDC Leader. The RTDC Leader is informed on the availability of the deliverable and verifies whether the introduction, formulation of objectives, interfaces to other project activities and conclusions are sufficiently clear to allow integration of the deliverable into the overall work programme of NF-PRO.

Project co-funded by the European Commission under the Euratom Research and Training Programme on Nuclear Energy within the Sixth Framework Programme (2002-2006)

Dissemination Level		
PU	Public	
RE	Restricted to a group specified by the partners of the [NF-Pro] project	
CO	Confidential, only for partners of the [NF-Pro] project	

DISTRIBUTION LIST

Name	Number of copies	Comments
AYNAL (Project Officer European Commission)	2	
Luc van Loon (Work package Leader)	1	
(RTDC Leader)	1	
Alain SNEYERS Coordinator NF-PRO	1	

Final Report

Work Package 2.5

Hyperfiltration of metal solutions through low-permeability material

This project is performed with the European Commission in the sixth framework of its programme on Management of Radioactive Waste:

Understanding and Physical and Numerical Modelling of the Key Processes in the Near-Field and their Coupling for Different Host Rocks and Repository Strategies (NF-PRO)

September 2006

Hyperfiltration of metal solutions through low-permeability material

Summary

Hyperfiltration (reverse osmosis) and precipitation of minerals from the hyperfiltrated solution are processes that potentially decrease radionuclide output from leaking radioactive waste disposal and lower the hydraulic conductivity of the near-field. Hydrogen gas emanating from corroding containers is envisaged to be the pressure source and bentonite clay the low-permeability membrane.

The processes of hyperfiltration and mineral precipitation were successfully demonstrated using substitute low-permeability material, Obernkirchen Sandstone. The precipitates occur in very small (mm sized) layers at the high-pressure side of the samples where they create zones of lowered hydraulic conductivity (2 to 3 orders of magnitude lower than initial) through precipitation of minerals in the pore spaces. The total amount of precipitates is very small compared to the dissolved amount which was passed through the membrane.

Hyperfiltration-induced precipitates and the resulting lowering of hydraulic conductivities were observed at solute saturations as low as 10 %. Nevertheless, at saturations higher than 50 % the damage strongly increased. Full reversibility of the hydraulic conductivity damage was only obtained at low saturations (10 %). This indicates that in many pores precipitated minerals are inaccessible to solution and thus protected from re-dissolution.

Hyperfiltration is thus considered a process which can potentially counteract transport of contaminants away from the near-field of leaky radioactive waster disposal sites through mineral precipitation and lowering of hydraulic conductivity. The quantitative aspect of this phenomenon is yet to be assessed. Experiments with clay membranes are currently under way.

Contents

1 Aim and scope of this study ..... - 7 -

2 Background ..... - 8 -

2.1 Hydraulic conductivity ..... - 8 -
2.2 Hyperfiltration (reverse osmosis) ..... - 11 -
2.3 Generation of hyperfiltration pressure ..... - 23 -

3 Methods and materials ..... - 25 -

3.1 Sample material ..... - 25 -
3.2 General set-up of the experiments ..... - 29 -
3.3 Solute analysis ..... - 32 -
3.4 Analysis of solid samples ..... - 32 -

4 Experiments ..... - 37 -

4.1 Experimental programme ..... - 37 -
4.2 Experimental work: general schedule ..... - 37 -

5 Post-mortem study of samples ..... - 51 -

5.1 Mass gain ..... - 51 -
5.2 Imaging with environmental scanning electron microscope ..... - 53 -
5.3 Element mapping ..... - 55 -
5.4 Porosity distribution ..... - 56 -

6 General interpretation of results ..... - 59 -

6.1 Occurrence of hyperfiltration precipitates ..... - 59 -
6.2 Porosity and permeability damage caused by precipitates ..... - 59 -
6.3 Reversibility of permeability damage ..... - 59 -

7 Outlook ..... - 61 -

8 References ..... - 62 -

Annex ..... - 66 -

1 Aim and scope of this study

The activities envisaged in this work aimed at the assessment of the importance of geochemical processes on the high-pressure side of membranes. High pressures can be generated in the near-field of nuclear waste repositories by hydrogen gas formed during corrosion of steel canisters or by elevated formation pressures. They can cause high, outwardly directed pressure gradients which may force radionuclide-containing fluids of higher salinity to flow through clay backfill material - even against osmotic counter-pressures. While water molecules may pass the clay membrane freely, dissolved ions remain behind and are thus concentrated as a brine at the high-pressure side. This process is called hyperfiltration and is commercially used e.g. for desalination of seawater.

Observations in desalination plants have shown that often precipitates, e.g. halite (NaCl) form on the membrane surface at the high-pressure side, although the overall brine may still be undersaturated. This is attributed to the development of a concentration polarisation layer (CPL) where the ion concentrations on the membrane surface exceed the dissolution product of certain minerals. Aim of this study was to check the behaviour of radionuclide homologue solutions during hyperfiltration.

Possible hyperfiltration precipitates may act as a buffering sink and could thus be essential for the retardation of radionuclides. Additionally the precipitation of minerals in the pore space leads to a decrease in porosity and thus also in hydraulic conductivity. This may lead to a hydraulic self-sealing which further limits radionuclide propagation.

The potential for re-dissolution of the precipitates after a pressure-drop shall be assessed.

2 Background

2.1 Hydraulic conductivity

The coefficient of saturated hydraulic conductivity K of porous samples can be computed after DARCY

$$K = \frac{Q}{I \cdot A} \qquad [2.1]$$

where:

K	=	coefficient of saturated hydraulic conductivity	[m/s]
Q	=	flow rate	[m³/s]
I	=	hydraulic gradient (= Δh / l)	[-]
Δh	=	pressure head across sample	[m]
l	=	height of sample	[m]
A	=	area of sample	[m²]
	=	$\pi \cdot r^2$ = here: $\pi \cdot (0.025\ m)^2$	= $1.9635 \cdot 10^{-3}$ m²
r	=	radius of sample	[m]

The intrinsic hydraulic conductivity k of porous samples which explicitly considers fluid properties is computed after

$$k = K \cdot \frac{\eta}{\rho \cdot g} \qquad [2.2]$$

where:

k	=	intrinsic permeability	[m²]
η	=	viscosity of fluid	[kg/m*s]
(water $0.92 \cdot 10^{-3}$ kg/(m*s) at 23° C)			
ρ	=	density of fluid	[kg/m³]
g	=	acceleration of gravity	[9.81 m/s²]

Intrinsic permeabilities are often given in the unit Darcy instead of square meters (1 Darcy = $9.87 \cdot 10^{-9}$ cm²).

From DARCY's law we can derive the DARCY velocity v_f which has the unit of a velocity. It is sometimes referred to as solution flux J_v or specific flux q.

$$v_f = \frac{Q}{A} = K \cdot I \qquad [2.3]$$

where

v_f	=	DARCY velocity (specific flux)	[m/s]

To obtain the actual average flow velocity v_a we have to correct the DARCY velocity for the effective porosity n_e

$$v_a = \frac{K \cdot I}{n_e} \qquad [2.4]$$

where

v_a	=	flow velocity	[m/s]
n_e	=	effective porosity	[-]

The total vertical hydraulic conductivity of a layered system with differing hydraulic conductivities may be calculated using Equation [2.5].

$$K_v = m \cdot \frac{1}{\sum_{i=1}^{n} \frac{m_i}{K_i}} \qquad [2.5]$$

where

K_v	=	total vertical hydraulic conductivity	[m/s]
m	=	total thickness	[m]
m_i	=	thickness of individual layer	[m]
K_i	=	hydraulic conductivity of individual layer	[m/s]

DARCY's law is only valid in fully laminar (non turbulent) flow regimes. The degree of turbulence of a flow regime can be described by the dimensionless REYNOLDS number Re, defined as the ratio between inertial and viscous forces. There is no distinct value of Re which separates the laminar and the turbulent realm. Usually, flow at Re < 1 is assumed to be fully laminar and flow at Re > 10 to be fully turbulent.

$$\mathrm{Re} = \frac{2 \cdot r \cdot v \cdot \rho}{\eta} \qquad [2.6]$$

where:

r	=	typical dimension of flow path (radius of pore)	[m]
v	=	velocity of flow	[m/s]
ρ	=	density of fluid	[kg/m³]
η	=	viscosity of fluid	[kg/m*s]

The classical equations developed by HAGEN (1839) and POISEUILE describe the amount and velocity of flow through capillaries (Eq. 2.7). They found that the flow rate Q shows a cubic and the coefficient of hydraulic conductivity K a square dependency on the radius r of the capillary. Any build-up of precipitates in such pores will thus lead to a reduction in hydraulic conductivity.

$$K = k \cdot \frac{\rho \cdot g}{\eta} = \frac{r^2}{12} \cdot \frac{\rho \cdot g}{\eta} \qquad [2.7]$$

where

r	=	radius of capillary	[L]
η	=	dynamic viscosity of fluid	[M/(L·T)]
ρ	=	density of fluid	[M/L³]
g	=	acceleration of gravity	[L/T²]
k	=	intrinsic permeability	[L²]
K	=	coefficient of hydraulic conductivity	[L/T]

The HAGEN-POISEUILE concept is only applicable to small and uniform capillaries and is therefore difficult to use in realistic porous media.

Another way to describe the permeability as a function of porosity is the KOZENY-CARMAN equation (see CHAPUIS & AUBERTIN (2003) and HANSEN (2004) for a detailed description of the equation and its application range).

$$K = \left[\frac{n^3}{(1-n)^2}\right] \cdot \left[\frac{\rho_w \cdot g}{\tau^2 \cdot (\rho_s \cdot S)^2 \cdot C_s \cdot \eta_w}\right] \qquad [2.8]$$

where:

K	=	coefficient of hydraulic conductivity	[L/T]
n	=	porosity	
ρ_s, ρ_w	=	density of solid and water	[M/L³]
g	=	acceleration of gravity	[L/T²]
S	=	specific surface area of granular material	[L²/M]
τ	=	tortuosity (τ < 1)	[-]
η_w	=	dynamic viscosity of water	[M/(L·T)]
C_s	=	geometry factor	[-]
		(C_s = 2 for tubular pores, C_s = 3 for pores between platelets)	

The KOZENY-CARMAN equation again postulates a cubic dependency of hydraulic conductivity on porosity but applies more to realistic porous media. It is not in wide-spread use due to the fact that it requires parameters that are difficult - or at least tedious - to measure (porosity, surface area, tortuosity).

2.2 Hyperfiltration (reverse osmosis)

The pore spaces in low permeability materials such as clays are generally larger than the largest hydrated ions. Since most silicate mineral surfaces are negatively charged at neutral pH, they attract cations and repulse anions such as chloride. A so-called double layer develops in which the ions are inhibited in their movement due to interactions with the charged surface (Fig. 2.1). Due to the requirement of charge balance, cations cannot move without their anionic counterparts.

The width of influence of a charged mineral surface is of course a function of the distance between two mineral surfaces. In highly compacted clays, the double layers of both surfaces may overlap (Fig. 2.2) which renders the pore channel between them basically impermeable to charged dissolved constituents whilst the relatively lowly charged water molecules may pass. The possibility of the passage of water whilst simultaneously ions are excluded causes the membrane properties of low permeability media.

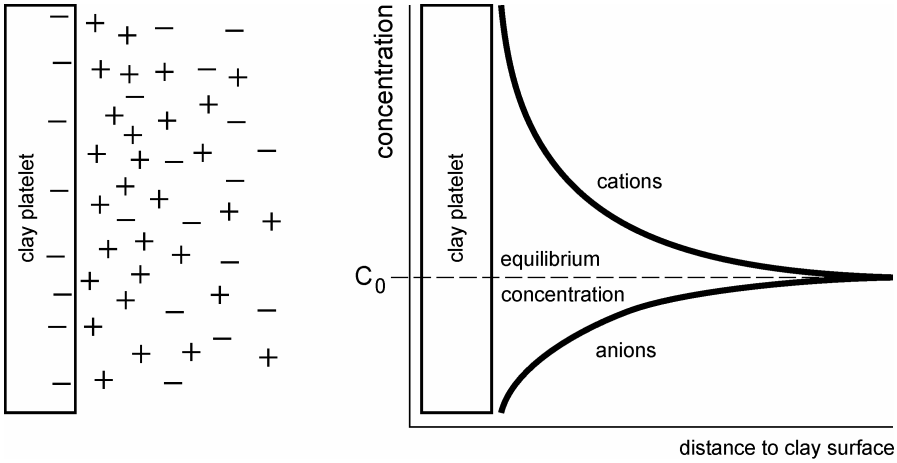

Figure 2.1: *Distribution of charged ions around a negatively charged clay platelet surface (double layer) (KEIJZER 2000).*

The movement of water in low permeability media is thus not only a function of the hydraulic (DARCY) gradient. Potentials which cause mass or solute fluxed can also stem from differing salt contents (osmosis) and electrical or thermal gradients. If two solutions of differing salinity are separated by a membrane (any body permeable to water but not to dissolved salts), water will flow from the low salinity to the high salinity side until the chemical gradient is overcome. This process is called osmosis and is well known from biology. The hydraulic head developing as a function of the chemical gradient is called osmotic pressure (Fig. 2.3, left and middle).

If we apply a pressure in excess of the osmotic pressure at the high salinity side, water molecules will pass the membrane while the dissolved constituents become enriched in the remaining solution (Fig. 2.3, right). This process is called reverse osmosis or hyperfiltration (sometimes the term ultrafiltration is also used). It is commercially used on large scale for the desalinisation of sea water and the removal of any types of undesired dissolved constituents from water.

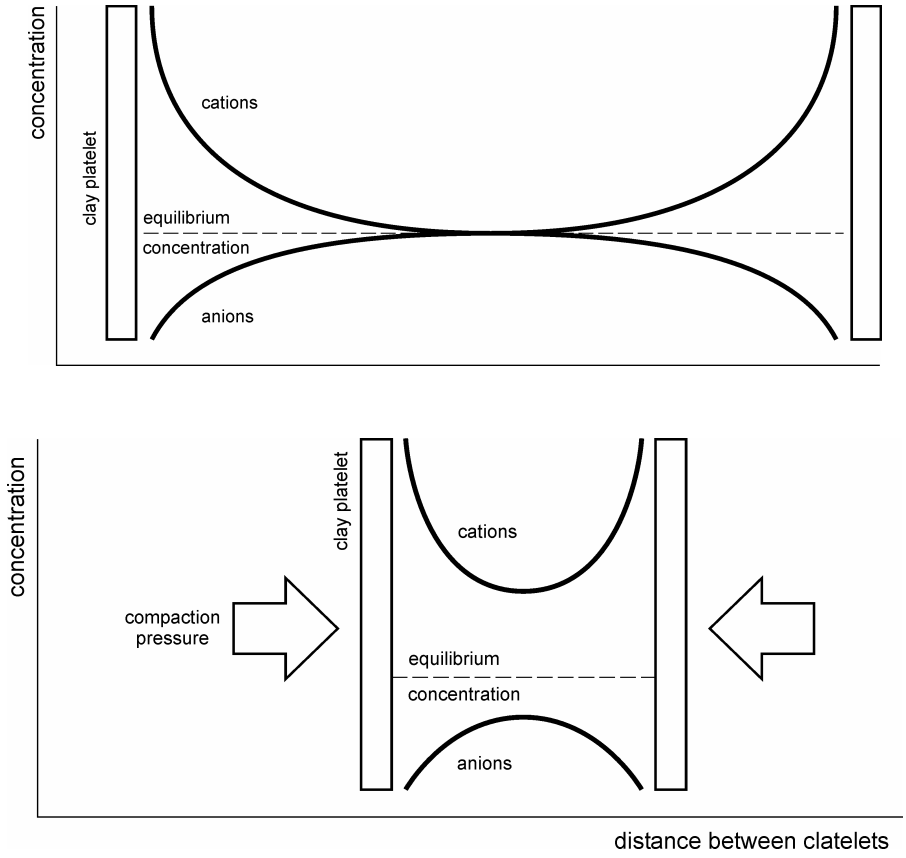

Fig. 2.2: *Compaction of clays causes an overlap of the individual double layers of the mineral surfaces and thus membrane properties (KEIJZER 2000).*

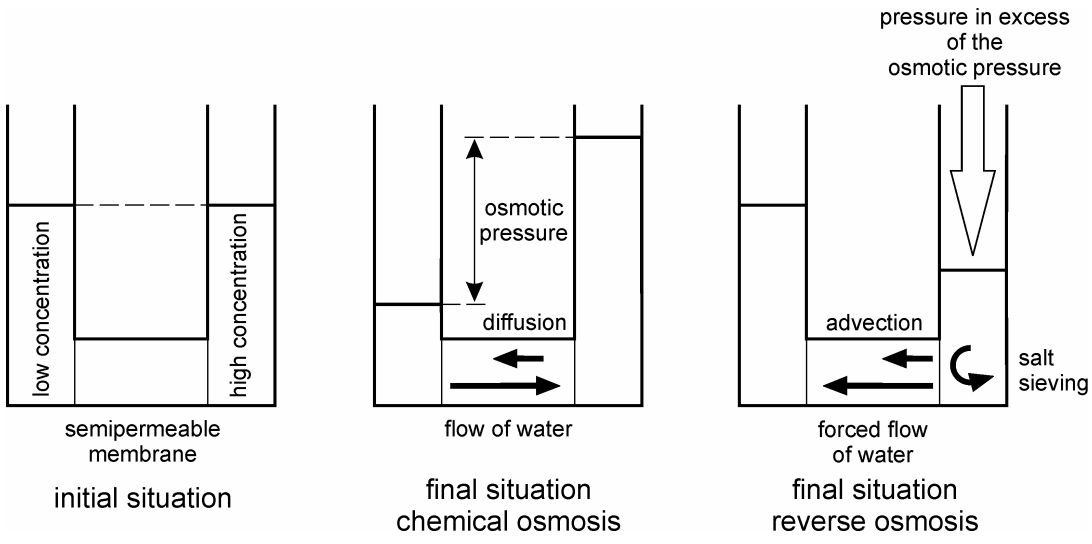

Fig. 2.3: *The principle of osmotic pressure generation as a result of the salinity contrast of two solutions separated by a membrane (left and middle) and the reversal of this process (reverse osmosis, hyperfiltration) (KEIJZER 2000).*

Osmotic processes have long been suspected to also occur in geological environments, especially in and around low permeability media such as clay formations. Their potential for the generation of highly saline brine which commonly occur in the deep subsurface has been widely discussed in literature (DICKEY 1969; KHARAKA & BERRY 1973; GRAF 1982).

The potential role of osmosis for the generation of abnormally high subsurface pressures was also discussed (PRICHETT 1980). DOMENICO & SCHWARTZ (1990) stated that a salinity contrast of 1000 mg/l (NaCl) across an effective natural membrane may cause differences in hydraulic heads of up to 10 m.

In the ideal case water molecules but not dissolved constituents will move through the membrane. In reality we often observe an infiltration of the solute into and finally through the membrane. A measure of the membrane efficiency (ideality) is the dimensionless **reflection coefficient** σ ($0 < \sigma < 1$; STAVERMAN 1952). Ideal membranes have $\sigma = 1$, meaning electrolytes will not be able to pass. At $\sigma = 0$ there is no membrane effect, electrolytes can freely pass the membrane. Figure 2.4 shows the dependency of the reflection coefficient on different parameters.

Membrane efficiency increases with decreasing porosity (or increasing degree of compaction) as well as with increasing cation exchange capacity (CEC). The latter is caused by the increasing surface charge of the mineral surfaces which promotes repulsion of ions (KHARAKA & BERRY 1973; BENZEL & GRAF 1984). For solutions of higher salinity, membrane efficiency decreases because of the shrinkage of the electrical double layer (WHITWORTH & FRITZ 1994). This decreases the repulsive forces.

For salts with identical cation and anion molarity (e.g. NaCl or $NiSO_4$)

$$\sigma_{cation} = \sigma_{anion}$$

For salts like $MgCl_2$

$$\sigma_{cation} \neq \sigma_{anion}$$

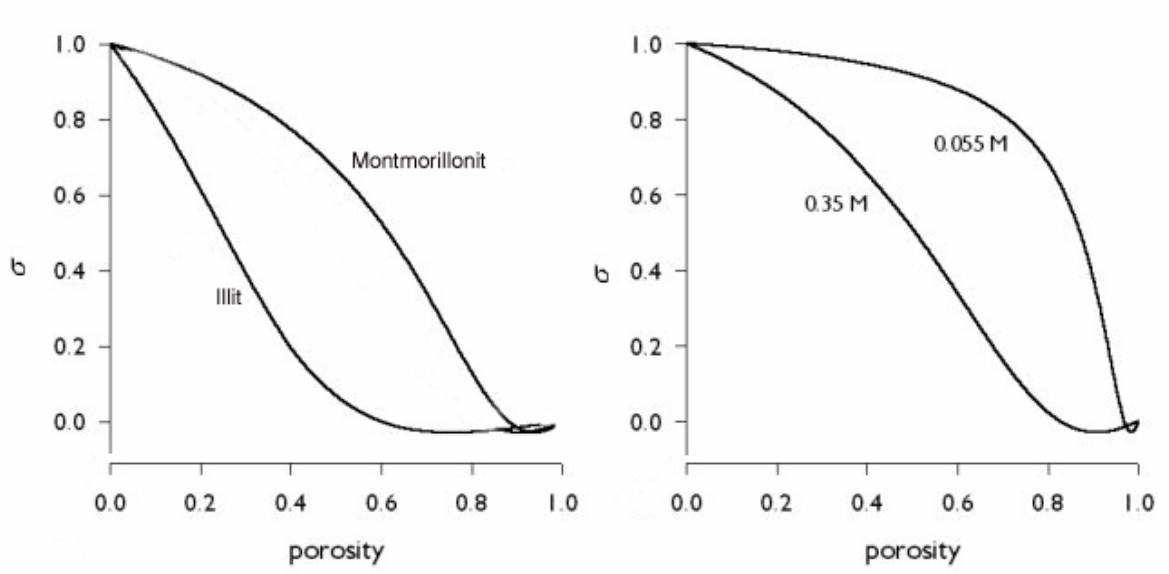

Fig. 2.4: *Reflection coefficient of clay membranes as function of porosity, mineralogy and salinity (modified after KEIJZER 2000).*

In membrane applications, the **hydraulic permeability coefficient** L_p is often used instead of the coefficient of hydraulic conductivity K. It describes the mechanical filtration capacity of a membrane, that is the fluid flow according to some pressure gradient. It differs from the coefficient of saturated hydraulic conductivity K by incorporating the membrane thickness x, acceleration of gravity g and fluid density ρ and is defined as follows (FRITZ & WHITWORTH 1993; WHITWORTH & FRITZ 1994):

$$L_p = \frac{Q}{A \cdot \Delta P} = \frac{v_f}{\Delta P} = \frac{K}{\rho \cdot g \cdot x} \qquad [2.9]$$

where:

Q	=	flow rate	[m³/s]
A	=	area of membrane	[m²]
ΔP	=	pressure difference	[m]
v_f	=	Darcy velocity (= Q/A)	[m/s]
K	=	coefficient of saturated hydraulic conductivity	[m/s]
ρ	=	density of fluid	[kg/m³]
g	=	acceleration of gravity	[9.81 m/s²]
x	=	thickness of membrane	[m]

L_p thus has the units (length² * time)/mass [(L²·T)/M].

The **solute permeability coefficient** ω of a membrane describes the diffusion of an ion inside the membrane. ω is not equivalent to the aquatic diffusion coefficient D_0 (after FICK) since it also takes into account the physical and electrical impedance of the membrane towards the diffusive flow of the solute. The solute permeability coefficient ω is defined as follows (FRITZ & WHITWORTH 1994):

$$\omega = \frac{D_0}{R \cdot T \cdot x \cdot \tau} \qquad [2.10]$$

where:

D_0	=	aquatic diffusion coefficient (FICK)	[m²/s]
R	=	gas constant	[8.31451 $J \cdot K^{-1} \cdot mol^{-1}$]
T	=	absolute temperature	[° K]
x	=	thickness of the membrane	[m]
τ	=	tortuosity (ratio of length of the diffusive path through the membrane relative to the membrane thickness x)	[$\tau > 1$]

ω thus has the units (mole/(seconds² * Joule) [mole/(sec²*J)].

Generally, low values for L_p are an indicator of high reflection coefficients σ since lower porosities and permeability usually increase the membrane efficiency. For an ideal membrane the solute permeability coefficient becomes $\omega = 0$. With an ideal membrane, no salt can pass. The solution flux (or DARCY velocity) v_f then becomes Equation [2.11 a] (FRITZ & WHITWORTH 1993).

$$v_f = L_p \cdot \Delta P - L_p \cdot \Delta \Pi \qquad [2.11\ a]$$

$$\Delta \Pi = v \cdot R \cdot T \cdot \Delta C \qquad [2.11\ b]$$

where:

ΔC	=	concentration difference across the membrane	[mole/cm³]
v	=	number of component ions of the dissolved salt (e.g. NaCl = 2)	
ΔΠ	=	osmotic back pressure.	

Since L_p is a constant and v_f prescribed by the pump, ΔP is bound to rise continually (FRITZ & WHITWORTH 1993). There is of course an upper limit imposed on the pressure rise by the structural integrity of the sample. In reality some solute will enter the sample. Taking into account the measure of ideality, the reflection coefficient σ, we obtain for the water flux v_f and the solute flux v_{solute}:

$$v_f = L_p \cdot \Delta P - \sigma \cdot L_p \cdot \Delta\Pi \qquad [2.12\ a]$$

$$v_{solute} = c_s \cdot (1-\sigma) \cdot v_f - \omega \cdot \Delta\Pi \qquad [2.12\ b]$$

$$c_s = \frac{(c_0 + c_i)}{2} \qquad [2.12\ c]$$

where:

c_s = average solute concentration on both sides of membrane

c_0 = solute concentration on high pressure side of membrane

c_i = solute concentration on low pressure side of membrane (at steady state = initial concentration), all in [mole/cm³]

The term $c_s \cdot (1-\sigma) \cdot v_f$ in Equation [2.12 b] describes the advective and the term $\omega \cdot \Delta\Pi$ the diffusive flux through the membrane.

The most important phenomenological coefficients describing membrane behaviour, including L_p and σ, can be calculated from measurements in the laboratory. Experimental set-ups are described in for example in KHARAKA & BERRY (1973), FRITZ & WHITWORTH (1993) and MALUSIS et al. (2001) in much detail. Triaxial cells are commonly used to contain the sample. Syringe pumps are employed to push water (or a solute solution) through the sample at a constant rate or pressure. Pressure is recorded by means of a differential pressure transducer. The quality of the passing solution can be monitored, usually until the exiting solution equals the composition of the input solution.

WHITWORTH & DE ROSA (1997) present a formula to calculate the reflection coefficient σ at steady state (influent concentration equals effluent concentration). To obtain this, Equation 2.12 a and 2.12 b have to be combined. Assuming $J_{solute} = v_f \cdot c_e$ and $c_e = c_i$ we finally obtain after some rearrangements:

$$\sigma = \frac{-(v_f - L_p \cdot \Delta P)}{(L_p \cdot v \cdot R \cdot T \cdot c_0 - L_p \cdot v \cdot R \cdot T \cdot c_i)} \qquad [2.13]$$

where:

v_f	=	Darcy velocity (specific flux)	[m/s]
L_p	=	hydraulic permeability coefficient	[m²·sec/kg]
ΔP	=	pressure difference	[m]
v	=	number of component ions of the dissolved salt (e.g. NaCl = 2)	
R	=	gas constant	[8.31451 $J \cdot K^{-1} \cdot mol^{-1}$]
T	=	absolute temperature	[° K]
c_0	=	solute concentration on high pressure side of membrane	[mole/cm³]
c_i	=	effluent solute concentration on low pressure side of membrane (at steady state = initial concentration)	[mole/cm³]

C_0 can be measured after an experiment when sampling the reservoir adjacent to the high pressure side of the membrane.

A simpler way to calculate the reflection coefficient is given by FRITZ & MARINE (1983). The second summand (ω·ΔΠ) on the right-hand side of Equation 2.12 b is often very small and can be omitted. Substituting Equation 2.12 c into the simplified Equation 2.12 b yields at steady state (effluent concentration c_e equals initial concentration c_i)

$$\sigma \approx \frac{C_0 - C_i}{C_0 + C_i} \qquad [2.14]$$

where:

σ	=	reflection coefficient	[-]
C_o	=	initial concentration	[mg/l]
C_i	=	$C_{effluent}$ = at steady state	[mg/l]

During hyperfiltration through a membrane dissolved salts which cannot pass will accumulate at the high pressure side (Fig. 2.5). This small area of accumulation is called concentration polarization layer (CPL, Fig. 2.6). Even undersaturated input

solutions may result in local oversaturations leading to a subsequent precipitation of minerals.

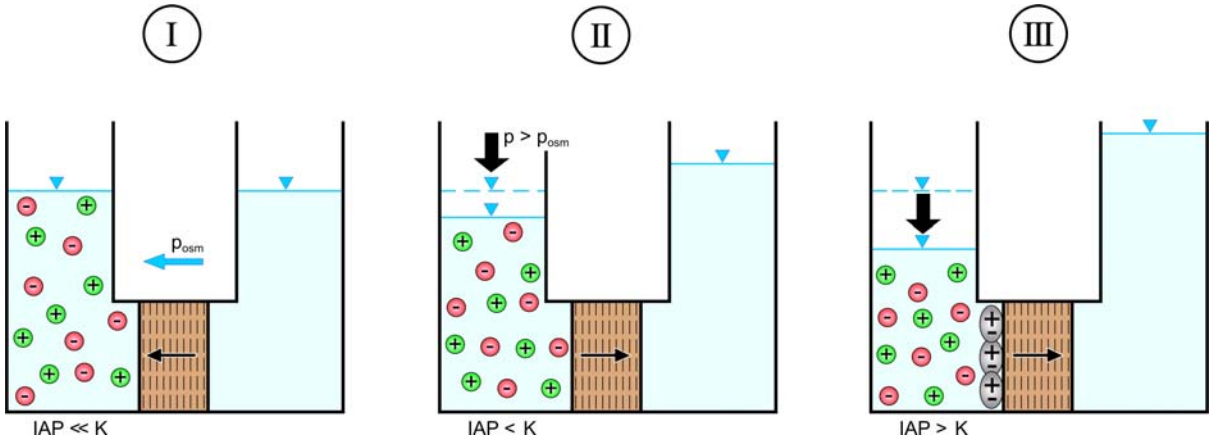

Figure 2.5: *Principle of reverse osmosis: (I) two solutions of differing salinity separated by a semi-permeable membrane, (II) pressure exceeding the osmotic pressure is applied on the high salinity side, water flows to low salinity side, ions become concentrated, (III) concentration increase at membrane exceeds mineral saturation leading to precipitation of salts (grey).*

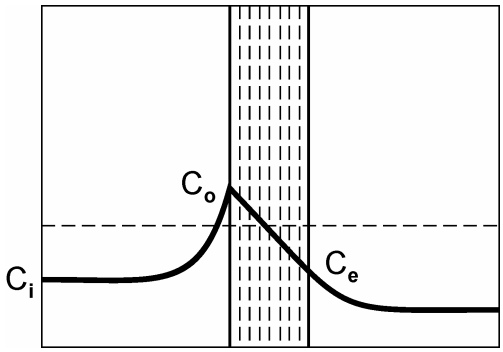

Fig. 2.6: *Concentration polarization layer (CPL) at a clay membrane where saturation (dashed line) is locally achieved (C_i = concentration input; C_e = concentration effluent; C_0 = maximum concentration at CPL) (WHITWORTH & FRITZ 1994; modified).*

In laboratory experiments, precipitation of sodium chloride (NaCl), calcite ($CaCO_3$) and several different heavy metal salts has been observed (FRITZ & EADY 1985; WHITWORTH et al. 1999). In nature this precipitation could be the cause behind the cementation of fine-grained fault zones or even for the genesis of metal deposits

(WHITWORTH et al. 1999; LUETH & WHITWORTH 2001). The required pressure gradients to induce such precipitations are surprisingly low (< 1), even with membranes of low ideality (σ = 0.25; WHITWORTH et al. 1999). The effective length x_i of a CPL can be estimated after FRITZ & WHITWORTH (1994) by

$$x_i \approx 10\ D_0 / v_f \qquad [2.15]$$

MARINE & FRITZ (1983) derived a steady-state solution for the concentration profile within a free solution adjacent to the high-pressure side of the membrane:

$$c_x = (c_0 - c_i) \cdot \left[\exp\left(\frac{-v_f \cdot x}{D_0} \right) - \exp\left(\frac{v_f \cdot x_i}{D_0} \right) \right] + c_i \qquad [2.16]$$

where:

D_0	=	aquatic diffusion coefficient (Fick)	[m²/s]
x	=	distance from membrane surface	[m]
c_0	=	concentration on high pressure side of membrane	[mole/cm³]
c_i	=	initial concentration	[mole/cm³]
c_x	=	concentration at distance x	[mole/cm³]
x_i	=	distance where $c_x = c_i$	[m]
v_f	=	Darcy velocity (= Q/A)	[m/s]

The second exponential term in equation [2.16] can be ignored if the length of the test cell is relatively large compared to D_0/J_s.

Whitworth & Gu (2001) present a formula to compute the maximum solute concentration c_0 on the high pressure side of the membrane:

$$c_0 = -c_i \cdot \frac{v_f \cdot \Delta x \cdot \tau \cdot (1-\sigma) + 2v \cdot D_0}{v_f \cdot \Delta x \cdot \tau \cdot (\sigma - 1) - 2v \cdot D_0} \qquad [2.17]$$

where:

D_0	=	aquatic diffusion coefficient (Fick)	[m²/s]
Δx	=	thickness of the membrane	[m]
τ	=	tortuosity (ratio of length of the diffusive path through the membrane relative to the membrane thickness x)	[-, $\tau > 1$]
c_0	=	concentration on high pressure side of membrane	[mole/cm³]
c_i	=	concentration on low pressure side of membrane	[mole/cm³]
c_e	=	effluent concentration	[mole/cm³]
σ	=	reflection coefficient	[-]
v_f	=	Darcy velocity (=Q/A)	[m/s]
v	=	number of component ions of the dissolved salt (e.g. NaCl = 2)	

and assuming $J_{solute} = v_f \cdot c_e$ and $c_e = c_i$.

Solving for c_0 in Equation 2.14 gives us a simpler relationship between c_0 and σ (WHITWORTH & DE ROSA 1997)

$$c_0 \approx \frac{-(\sigma \cdot c_i + c_i)}{\sigma - 1} \qquad [2.18]$$

This formula can be used to calculate the ability of a membrane to concentrate a solution according to its reflection coefficient. Figure 2.7 shows the relationship between the two parameters. Membranes of lower efficiency ($\sigma < 0.2$) - such as our sandstones - will only cause concentration increases of less than a factor of two.

Hyperfiltration through a clay membrane may lead to a fractionation of isotopes (COPLEN & HANSHAW 1973 a; BENZEL & GRAF 1984; HAYDON & GRAF 1986; FRITZ et al. 1987; DEMIR 1988; FRITZ & WHITWORTH 1994; WHITWORTH et al. 1994). The heavier isotopes usually become enriched at the high pressure side and in the CPL.

The accumulation of solutes at the high-pressure side of the membrane will of course increase the ionic strength on this side. This will decrease the membrane efficiency (compare Fig. 2.4, right) and will lead to decreasing head difference with time (Fig. 2.8).

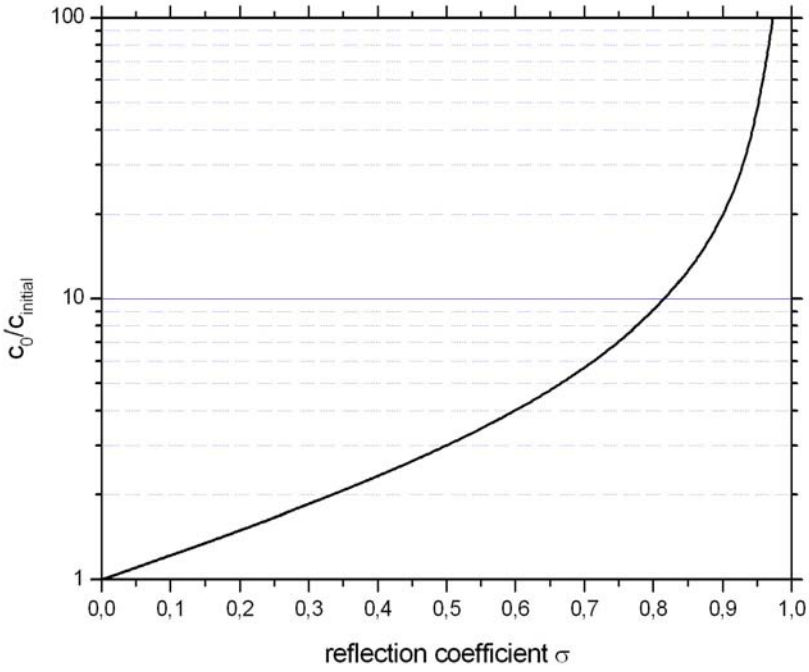

Fig. 2.7: *Ratio of concentration on high pressure side of a membrane (c_0) and the initial concentration (c_i) as a function of membrane reflection coefficient (calculated after Equation 2.18; modified after WHITWORTH & DE ROSA 1997).*

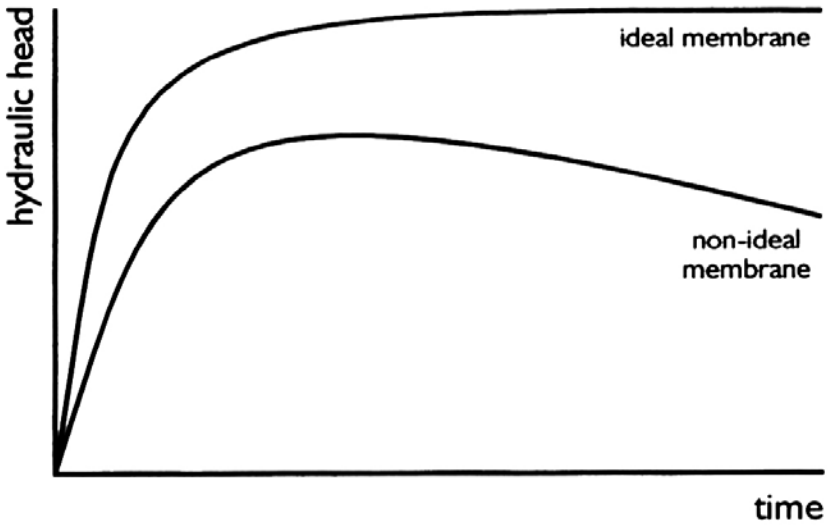

Fig. 2.8: *Temporal development of hydraulic head for ideal and non-ideal membranes (KEIJZER 2000, modified after KATCHALSKY & CURRAN 1965).*

The life-span of a geological osmotic cell was investigated by FRITZ & WHITWORTH (1993). For a spherical cell of radius r they derived the half-life $t_{½}$ needed to decay the osmotically induced pressure to be

$$t_{1/2} = \log_e(2) \cdot r / 3 \cdot \omega \cdot v \cdot R \cdot T \qquad [2.19]$$

The most important parameters are the solute permeability coefficient ω and the size of the cell. For smectite-rich clays with high ideality (σ close to 1), the solute permeability coefficient ω becomes close to zero. The life span of such an osmotic cell with geological dimensions can therefore easily reach ten thousands to hundred thousands of years.

2.3 Generation of hyperfiltration pressure

Pressures in excess of the osmotic pressure between the radionuclide solution and the surrounding pore water are needed to induce hyperfiltration. Such pressures may be generated in a waste repository site by:

- settlement (compaction, convergence of tunnels and shafts)
- tectonic activities (compression)
- swelling of bentonite buffer material
- gas generation

The latter process is the most probable. RÜBEL et al. (2004) list the following possible processes of gas generation:

- metal corrosion
- radiolysis (disintegration of water through radioactive irradiation)
- disintegration of organic matter (only for low and medium level waste)

Radiolysis can probably be ignored safely due to the small amounts of gas created compared to corrosion and organic matter decay.

It is well known that steel surfaces in contact with water generate hydrogen gas according to Equation [2.20]. The iron is converted into magnetite. Metal corrosion is strongly enhanced in the presence of a conductive medium, e.g. a saline (chloride-rich) solution.

$$3\ Fe + 4\ H_2O \rightarrow Fe_3O_4 + 4\ H_2 \qquad [2.20]$$

For one mole of iron 4/3 mole hydrogen gas are being produced which translates into 29.9 litre of gas for each 55.85 g iron corroded. The total amount of gas in a waste repository site is of course very much dependent on the type and the number of canister.

Steel in contact with acidic waters also generates hydrogen gas (reaction 1 in Figure 2.9). For one mole of iron, one mole of hydrogen gas is produced. This translates into 22.4 litres of gas for 55.85 grams iron corroded. Since the pore space available around the canister can safely assumed to be low, the gas may create locally pressures high enough to drive solutions leaking from the canister outwards. Gas will only be able to leave the site when the pressure exceeds the capillary gas entrance pressure of the surrounding geotechnical or geological barrier.

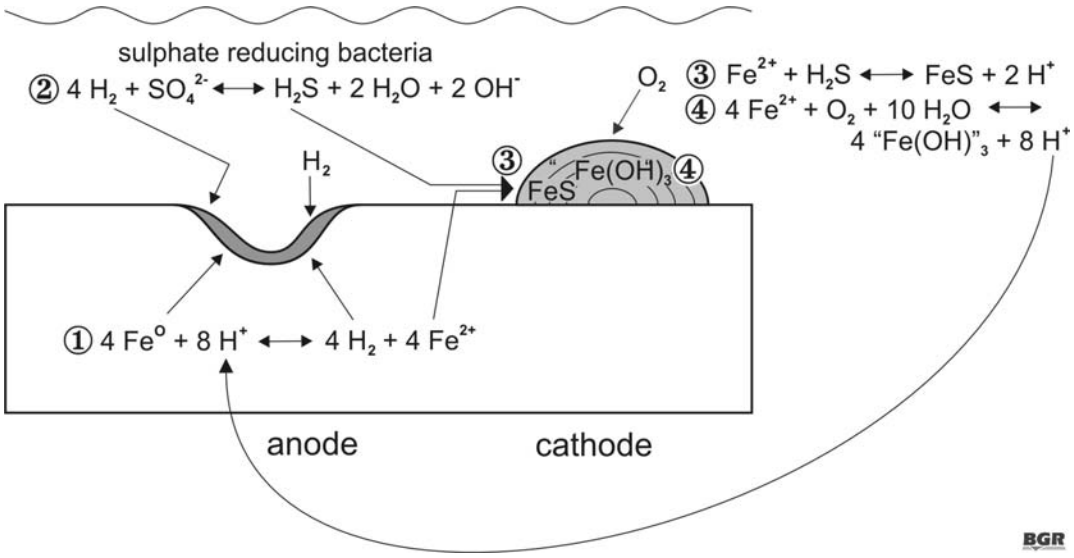

Figure 2.9: *Processes of the corrosion of metal surfaces. Reaction 1 creates hydrogen gas, a potential source of overpressures in the surroundings of waste containment canisters (HOUBEN & TRESKATIS 2006).*

3 Methods and materials

3.1 Sample material

Clays pose some certain problems for experimental work. Their very low hydraulic conductivity ($K \approx 1 \cdot 10^{-12}$ m/s) allows only very low flow rates and makes experiments very time-consuming. Since we wanted to perform several experiments with different rates of solute saturation and varying hyperfiltration rates this would not have been possible in a reasonable period of time. Bentonite additionally exhibits swelling behaviour when exposed to water. This alters the pressures acting on the sample (and its pore water) and both its porosity and hydraulic conductivity. The latter two parameters were crucial for the interpretation of our experiments since we wanted to compare the effects of the hyperfiltration phase on them (comparison before/after). Any additional changes due to swelling would have rendered the experiments basically useless. In order to avoid these problems we chose sandstone as substitute material. Sandstone is volume-stable and has a sufficient hydraulic conductivity to make experimental runs possible but low enough to invoke membrane behaviour.

We chose to use Obernkirchen sandstone, a grey-white to yellow-white, coarse silty to fine sandy, very homogeneous (no visible bedding) rock of lower cretaceous age. The still active quarry is located in the town of Obernkirchen, some 50 km southwest of Hannover. It is commonly used as building and decorative stone in Northern Germany. All samples were cylindrical and were core-drilled from the same block of stone. The sample dimensions were:

- diameter 0.050 m
- height 0.020 m
- area $1.9635 \cdot 10^{-3}$ m² (19.64 cm²)
- volume $3.927 \cdot 10^{-5}$ m³ (39.27 cm³)

With an average porosity of 17 % (Tab. 3.1) the total pore volume in a sample is about 6.68 cm³. One filling of the piston pump of 250 ml thus equals about 37 pore

volumes. Some basic properties of the sample material are listed in Table 3.1 and Figure 3.1.

Table 3.1: Properties of investigated samples from different analytical techniques.

	NMR	Hg porosimetry					N_2-Ads. (BET)
sample	porosity	porosity	bulk density	mineral density	pore - radius	surface area	surface area
	[%]**	[%]**	[g/cm³]	[g/cm³]	[µm] #	[m²/g]	[m²/g]
6-027-1 V1 vorher a	18.06	17.8	2.14	2.605	1.94	0.274	0.7360 0.2540
6-027-1 V1 vorher b		17.9	2.14	2.610	1.96	0.386	0.2465
I-5-70 6-027-2 V1	15.58 15.49	18.8	2.14	2.631	1.36	1.243	1.9174 1.7493 1.5916
II-1-70 6-049-1 V2		15.2	2.23	2.625	0.98	1.022	1.4021
III-10-70 6-049-2 V3		18.4	2.15	2.639	1.44	1.108	1.1724
IV-2-70 6-053-V4		16.6	2.21	2.650	1.31	0.952	0.9458
6-053-V5 vorher a		16.9	2.19	2.632	1.18	1.114	1.9489
6-053-V5 vorher b		17.4	2.19	2.654	1.24	1.019	0.9939
V-2-50 6-053-V5		17.1	2.17	2.623	1.36	0.832	0.7249
VI-5-50 6-053-V6		16.3	2.19	2.616	1.31	0.734	1.0953
VII-3-50 6-053-V7		17.1	2.16	2.611	1.24	1.099	1.4544
VIII-5-30 V8		18.7	2.14	2.627	2.12	0.484	0.4281
IX-2-30 V9		15.6	2.16	2.564	1.91	0.236	0.4553
X-2-10 V10		14.6	2.20	2.571	1.59	0.178	0.5747
XI-2-90 V11		15.9	2.18	2.593	1.70	0.182	0.5410
XII-5-90 V12		19.5	2.12	2.640	1.52	0.770	1.1162
XIII-5-10 V13		19.0	2.14	2.639	1.81	0.901	0.8362
XIV-5-10 V14		17.1	2.19	2.641	1.05	1.059	1.6211
XV-5-70 V15		19.2	2.13	2.633	1.70	1.025	1.7289
Median		17.1	2.160	2.627	1.44	0.901	1.045
Mean		17.3	2.167	2.621	1.51	0.769	1.070

Literature data on porosity and surface area of the Obernkirchen sandstone range between 10 to 14 % and 1.5 m²/g, respectively (KRUS 1995; FRANZEN & GRIESER 2002). Our samples - having a mean porosity of 17 % - were obviously from a somewhat more porous block. The mean (and median) specific surface area (N_2 adsorption) of our samples is around 1.05 m²/g and thus somewhat smaller (Fig. 3.1). The surface area data from mercury porosimetry must be assumed to be less accurate than data from nitrogen adsorption.

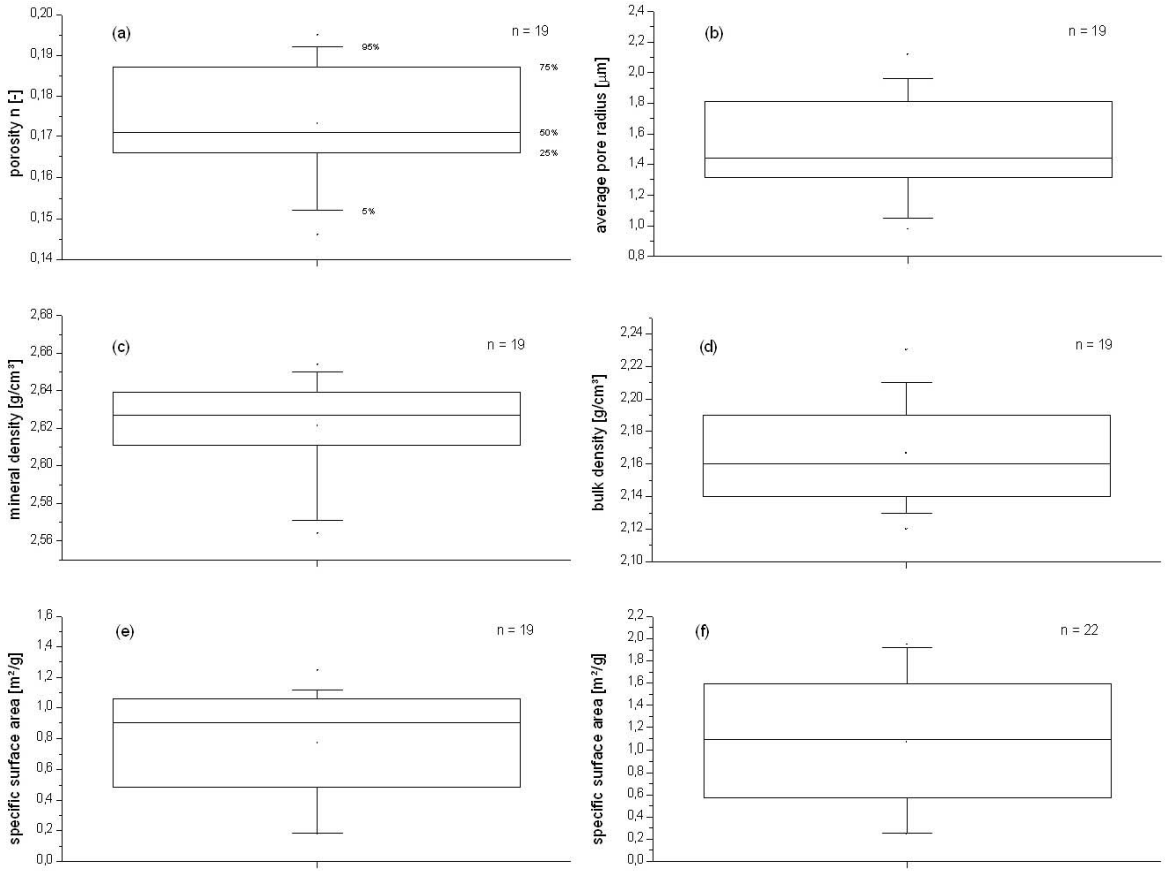

Figure 3.1: *Distribution of some basic properties from Table 3.1 of the studied Obernkirchen sandstone samples. (a) to (e) from mercury porosimetry, (f) from nitrogen adsorption (BET isotherm).*

All samples were measured and weighed before and after the experiments to be able to detect weight gains induced by the precipitation of crystals.

The total carbon content was determined for two samples to be 0.06 and 0.54 weight-%, respectively.

The cation exchange capacity (CEC) was determined for four untreated samples (two analyses each, a & b). The results are summarised in Table 3.2. As expected the CEC is rather low which indicates low membrane efficiencies.

Table 3.2: Cation exchange capacity of four samples

Sample	Subsample	Sample weight [g]	CEC [meq/100 g]
1	a b	1.107 2.055	0.5 0.5
2	a b	0.985 1.897	0.4 0.6
3	a b	0.748 1.914	0.7 0.5
4	a b	1.260 1.948	0.4 0.5
		Mean	0.513

Bi-distilled water was used for all pre-flushing and post-filtration experiments (EC < 0.2 µS/cm). Nickel sulphate ($NiSO_4 \cdot 6H_2O$, p.a., MERCK, M = 262.7 g/mol) was used as model salt and dissolved in 250 ml bi-distilled water at different degrees of saturation (10, 30, 50, 70, 90 %; Tab. 3.3). The maximum solubility of nickel sulphate is 650 g/l (≈ 2.50 mol/l).

Table 3.3: Properties of the nickel sulphate solutions.

Saturation S	Concentration C	Concentration C	Ω (= actual conc./ max. solubility)	SI (=log Ω)
[%]	[g/l]	[mol/l]	-	-
10	65	0.25	0.1	- 1.00
30	195	0.74	0.3	- 0.52
50	325	1.24	0.5	- 0.30
70	455	1.73	0.7	- 0.15
90	585	2.23	0.9	- 0.046

3.2 General set-up of the experiments

The set-up of the experiments (Fig. 3.2) was assembled from different components. The high-precision piston pumps used for pumping the solute through the sample and to build up the surrounding pressure were custom-made for this purpose by WILLE GEOTECHNIK (Göttingen, Germany). Maximum pressure and maximum flow rate for both are 60 bar (6000 kPa) and 50 ml/min, respectively. The piston is able to take up to 250 ml fluid. The pump has an in-build pressure transducer and a displacement (volume) measurement device. The accuracy of the latter is rated at 0.01 µl. Time, pressure and piston movement (volume) of both pumps were continuously recorded (20 sec interval) digitally on a laptop using an Excel macro called PVC 60, programmed by WILLE GEOTECHNIK.

The sample was held in a sample holder (Fig. 3.3) which itself was contained in a triaxial cell (Fig. 3.4), the latter rated at 700 bar pressure. The whole cell and its interior are made up of stainless steel. The sleeve in which the sample is embedded was made of high-durability rubber. Test fluids entered the sample from the bottom and exited through a capillary which leaves the cell through a pressure-tight seal (Fig. 3.3, lower figure). The remaining space between the sample holder and the triaxial cell was filled with hydraulic oil (about one litre) and connected to one of the piston pumps. The applied external pressure thus acted on all sides of the sample. The external pressure was always higher than the fluid pressure pushing water or solute through the sample to avoid the establishment of flow around the sample. In a few cases oil entered the sample (indicated by floating oil in the sampling beaker). These experiments were immediately cancelled and results and samples discarded.

Stainless steel porous diffusor plates (frits) were used both below and on top of the sample to allow an even flow distribution over the sample faces.

Specific electrical conductivity of the outflowing solution was continuously measured using a conductivity probe (WTW TetraCon 325, WTW GmbH, Weilheim, Germany) installed in a flow-through cell (UIT GmbH, Dresden, Germany) and a conductivity meter (WTW Lf 340). Values were transferred and stored simultaneously (5 sec interval) on a laptop using the software MultiLab Pilot (WTW).

The temperature in the laboratory and of the solutes ranged between 25 and 28° C.

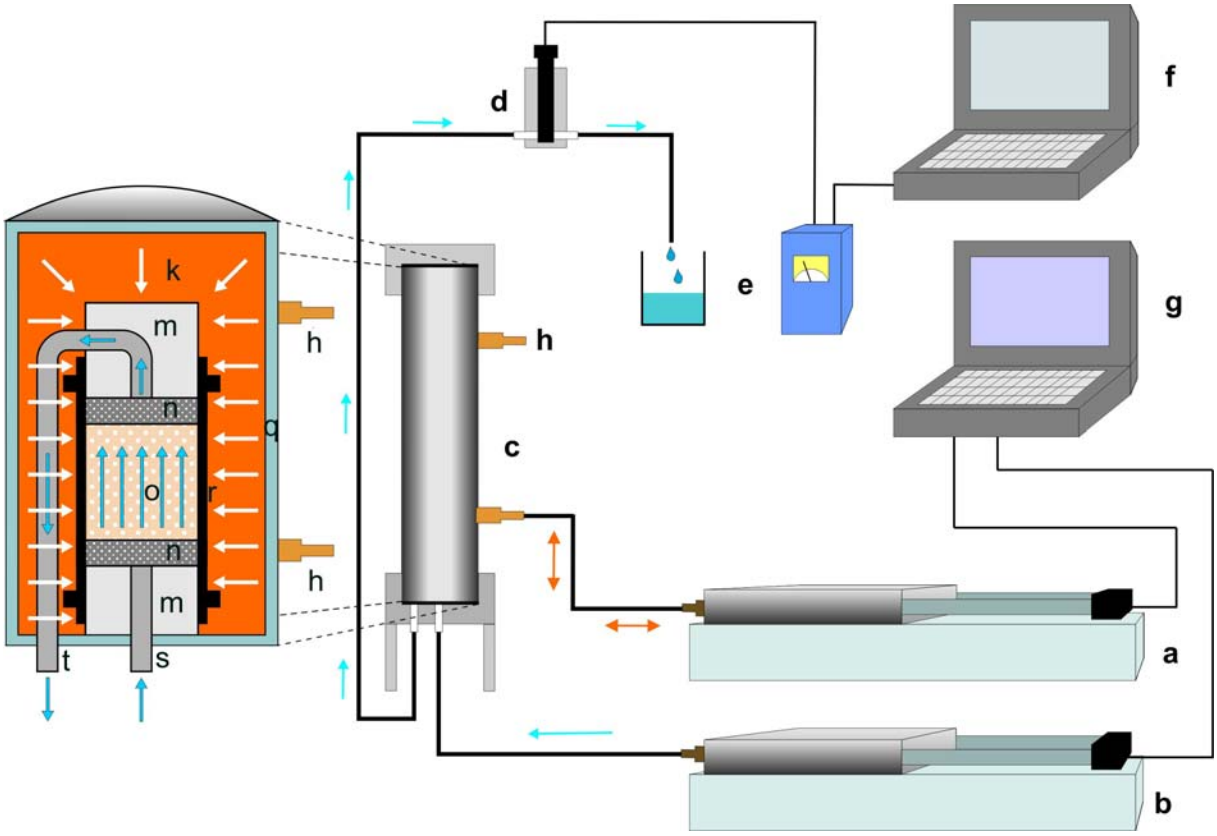

Figure 3.2: *General set-up of the experiments. The arrows mark the flow of the solution (blue) and hydraulic oil (yellow).*

a	high-precision piston pump (oil pressure)
b	high-precision piston pump (solution)
c	triaxial cell
d	conductivity probe in flow cell
e	sampling and conductivity meter
f, g	computers to store pressure and conductivity data
h	oil valves
k	oil
m	top and bottom sample cap
n	porous diffusor plates
o	sample
q	wall of pressure cell
r	rubber sleeve (mantle)
s	inflow capillary
t	outflow capillary

Figure 3.3: *Sample holder without (upper figure) and with sample installed (in rubber sleeve, lower figure).*

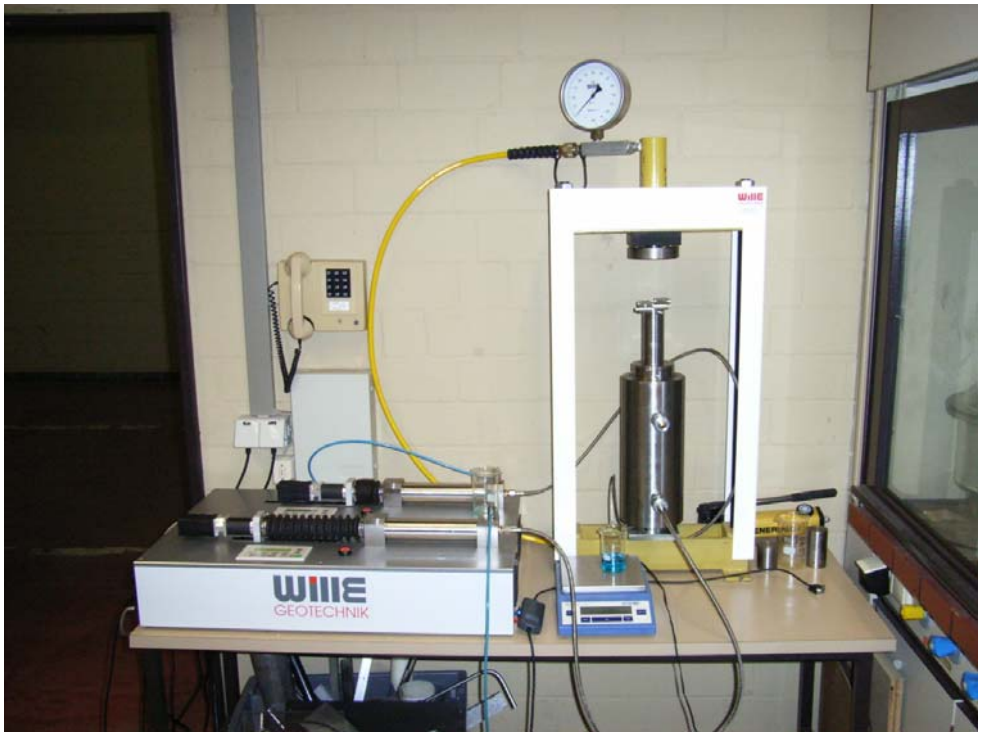

Figure 3.4: *Triaxial cell (right, in frame) and piston pumps (left).*

3.3 Solute analysis

The specific electrical conductivity of the passing solution was measured using the equipment described under 3.2.

Aliquots of 1.000 ml were taken from the outflow using an EPPENDORF pipette and diluted 1:10 with distilled water. The dissolved ionic constituents of the solution were determined in the BGR lab using an ICP-OES (SPECTRO Ciros CCD).

3.4 Analysis of solid samples

3.4.1 Nitrogen adsorption

The surface area of the samples was investigated in the BGR laboratory using a MICROMERITICS Gemini 2375. The surface area was calculated using the BET-isotherm approach (49 points adsorption, 49 points desorption).

3.4.2 Scanning electron microscope (SEM)

The occurrence and distribution of precipitates in fragments of the used samples was investigated in the BGR laboratory using an Environmental Scanning Microscope (ESEM) of the type FEI Quanta 600 FEG.

Nickel sulphate crystals were identified qualitatively by their nickel and sulphur contents via EDX.

3.4.3 Mercury porosimetry

Porosity, average pore radius, pore size distribution, bulk and mineral density and surface area were determined externally by POROTEC (Hofheim, Germany) using a mercury porosimeter of the type THERMOELECTRON PASCAL 140. Mercury is injected into the evacuated sample with increasing pressures. The radius of the pore corresponding to the applied pressure is calculated according to the WASHBURN equation

$$p = \frac{-2 \cdot \gamma \cdot \cos\Theta}{r} \qquad [3.1]$$

where:

p	=	injection pressure	[N/m²]
r	=	pore radius	[m]
γ	=	surface tension of mercury	[N/m]
Θ	=	contact angle	[-]

3.4.4 Cation exchange capacity

The CEC (cation exchange capacity) was determined by the Cu-triene method (slightly modified after KAHR & MEIER (1996)). The Cu-triene solution is produced by adding 1.596 g CuSO4 (dried) to 100 ml water, then adding 1.463 g triethylene-tetramine (triene), and finally adding water up to 1000.0 ml. The samples were dried at 60 °C maximum. The water content was determined by drying 1 g at 105 °C for 2-3 days. For the determination of the CEC, 0.1000 g and 0.1500 g were weighed in 85 ml centrifuge tubes. Finally, 10.0 ml of the 0.01 M Cu-triene solution and 50.0 ml

water were added. Before centrifugation the suspension was kept for 2 h in an end-over-end shaker. The supernatant was analyzed with respect to vis-absorption at 578 nm against water. In addition the vis-absorption of the pure Cu-triene solution (diluted 1:5) was recorded. For the calculation of the CEC the difference between the absorption of the Cu-triene solution (1:5) and the absorption of the supernatant of a sample is converted to the concentration and referred to the dry mass of the sample.

3.4.5 Calcite content

The total inorganic carbon (TIC) content of the samples, later recalculated as $CaCO_3$, was determined using a LECO CS-444 analyser.

3.4.6 µ-EDXRF (element mapping)

Non-destructive energy differentiated µ-X-ray fluorescence analysis (µ-EDXRF) provides the capability of acquiring high-resolution geochemical analyses from different types of geological materials. The sample preparation is minimized since no coating is necessary. Depending on the application, the effect of surface roughness can be neglected. The µ-EDXRF instruments allow relatively fast, continuous, and reliable spot analysis, line or area scans (mapping) of samples. The µ-EDXRF technique provides non-destructive, multi-element, µ-scale, (semi-)quantitative analysis of elements down to trace level (WITTENBERG &SCHWARZ-SCHAMPERA 2005).

Two µ-EDXRF instruments by COX ANALYTICAL INSTRUMENTS (Gothenborg, Sweden) based on X-ray fluorescence are in use at the BGR, the ITRAX™ X-ray microscope and the ITRAX™ geoscanner. Both systems operate under ambient air conditions using a 3 kW long fine focus Mo side-window tube.

The ITRAX™ X-ray microscope utilises X-rays for element analysis, employing an energy-dispersive ROENTEC™ UHV Dewar Si(Li)-detector. The element range includes all elements from Mg and heavier (Z > 12), with detection limits at the µg/g level. For most applications the tube runs with 45kV and 30mA having the capacity for the simultaneous detection of lighter and heavy elements. High sensitivity is obtained by the mounted COX™ mono capillary X-ray optical unit of 100 µm beam size. Typically, the step size equals the spot size of the capillary and a counting time of 500 or 1000 µs/spot are used. The data can be compiled as point, line or

accumulated spectra of an area. The measuring spot, and thereby the lateral analytical resolution, can be varied in the 10 - 100 µm range. The sample stage is designed to enable precise movement of the sample at steps of 10 µm. The pixel size of the resulting map equals the spot size of the measurement.

The ITRAX™ geoscanner allows for the characterization of the chemical composition of samples up to 750 mm length. The X-ray beam focuses through a COX™ flat-beam capillary optic of a rectangular cross-section of 250 µm x 22 mm. Because of the relative large beam size and high counting times (up to 120 seconds) and step sizes of 10 to 250 µm, the geoscanner is more sensitive than the ITRAX™ microscope. The X-ray fluorescence signal is detected by a ROENTEC XFlash® 2001 Detector. An X-ray line-scanning camera provides optical images of X-ray absorption by the sample at a defined thickness at a microscopic scale. The transmitted X-rays are recorded with an array of 1024 diodes, each 25 µm wide. The optical line camera system consists of a CCD colour camera operating in line mode, synchronized with the stepper motor movement. The camera has 640 pixels/line and is equipped with a SCHNEIDER CM 120 BK Compact Xenoplan lens system giving a field view of about 8 mm (depending on the chosen spacing) perpendicular to the scanning direction corresponding to 0.0125 mm/pixel.

3.4.7 Nuclear magnetic resonance (NMR)

Nuclear magnetic resonance (NMR) is a physical phenomenon based upon the magnetic property of atomic nuclei. Most of them have an intrinsic magnetic moment. The most often-used nuclei are hydrogen-1 and carbon-13. NMR studies a magnetic nucleus, like that of a hydrogen atom by aligning it with a very powerful external magnetic field and perturbing this alignment applying an electromagnetic field.

The NMR spectrometer used was a type MARAN ULTRA 5 owned by the LEIBNIZ INSTITUTE FOR APPLIED GEOSCIENCE (GGA, Hannover, Germany). The magnetic field is created by a permanent magnet with a magnetic field intensity of 0.19 Tesla. The magnet is kept at a constant temperature of 35° C and contains a tubular boring of 5 cm diameter that serves as sample holder. Samples may me up to 1 m long. All samples have to be water saturated prior to measurement. The hydrogen atoms aligned in the permanent magnetic field are then excited using a radio frequency

pulse that includes the resonance frequency of hydrogen (8 MHz). This causes a magnetisation normal to the magnetic field of the permanent magnet (deflection). After turning off this impulse the magnetisation returns to its original state (relaxation). This induces a decreasing voltage curve that can be detected through a measuring coil (Fig. 3.5). Fast relaxation times indicate closeness of the hydrogen atoms to a solid surface while slow relaxation times indicate larger pore spaces. The boundaries between the different types of water bonding in sandstone sample are commonly set according to the relaxation times T_2.

T_2 < 4 ms for clay bound water

4 < T_2 < 33 ms for capillary water

T_2 > 33 ms for free water

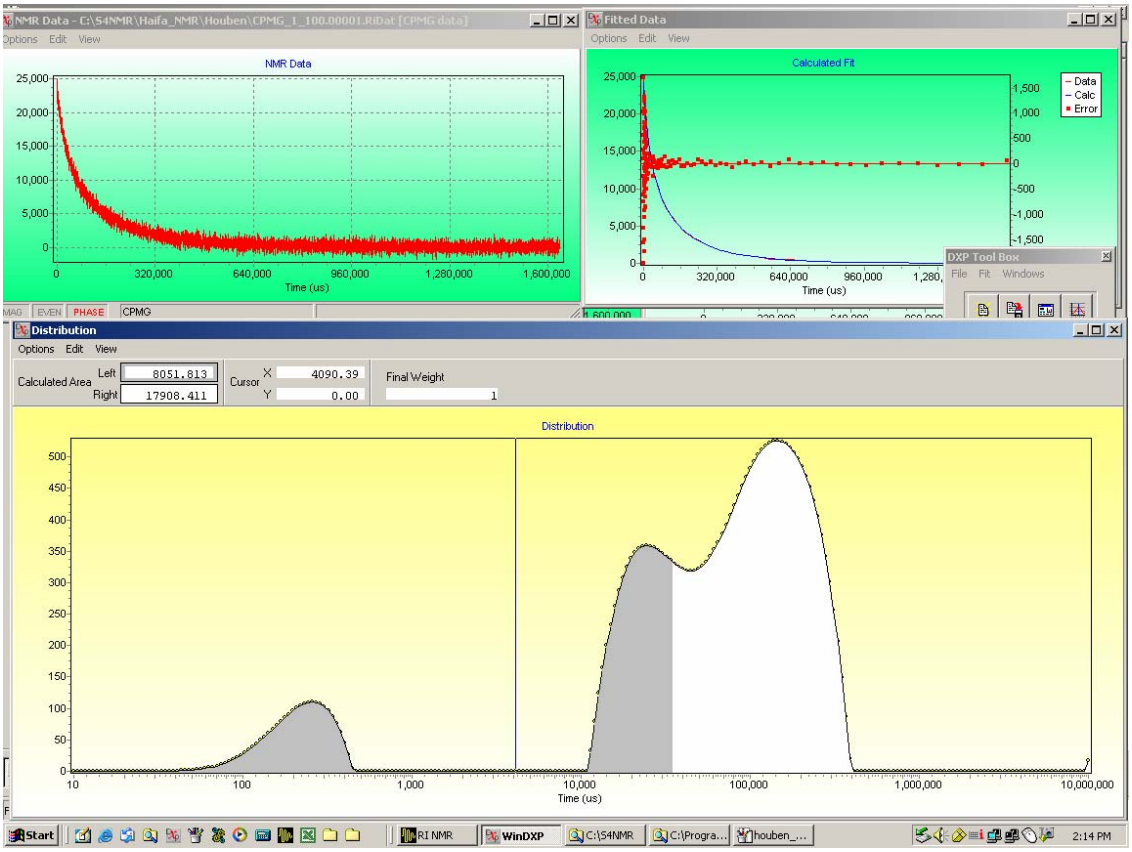

Fig. 3.5: *NMR relaxation of an Obernkirchen sandstone sample. The shaded area (grey) below the curve equals capillary bound water, the white area mobile pore water (free water). Clay-bound water (T2 < 4 ms) is practically absent.*

4 Experiments

4.1 Experimental programme

A variety of experimental configurations was performed to investigate the influences of varying hyperfiltration flow rates and solute saturations (Tab. 4.1). During the course of the experiments we decided to concentrate on two hyperfiltration flow rates (2 and 5 ml/min) and apply five different saturations ranging from very low to nearly saturated. The results of these experiments are listed in the tables of Annex B.

Table 4.1: Overview of the performed experiments.

Flow rate hyperfiltration [ml/min]	**Saturation $NiSO_4$ [%]**				
	10	**30**	**50**	**70**	**90**
1				x	
2	x	xx	x	x	x
3			x		
5	xx	x	x	xx	x
10				x	

x = experiment performed, xx = experiment performed twice

Nomenclature: XII-2-30 = Experiment 12, Q_{hyp} = 2 ml/min, saturation S = 30 %

4.2 Experimental work: general schedule

All experiments comprised four phases. The first phase (phase zero) was used to precondition the sandstone cores. Therefore 250 ml (≈ 37 pore volumes) of bi-distilled water were pumped through the system at a rate of 5 ml/min. This was done in order to:

- ❖ wet all surfaces
- ❖ eliminate air from tubing and sample (full saturation)
- ❖ eliminate dust from sample

The final pressures obtained from this stage were usually not used for interpretation. The “dead volume” of tubing, sample and conductivity cell was measured to be around 40 ml. The pressure curve from this stage usually shows an initial steep incline indicating unsaturated flow and compression of air (Fig. 4.1). This is followed by a decrease in pressure which develops into a pressure plateau indicating fully saturated steady-state flow.

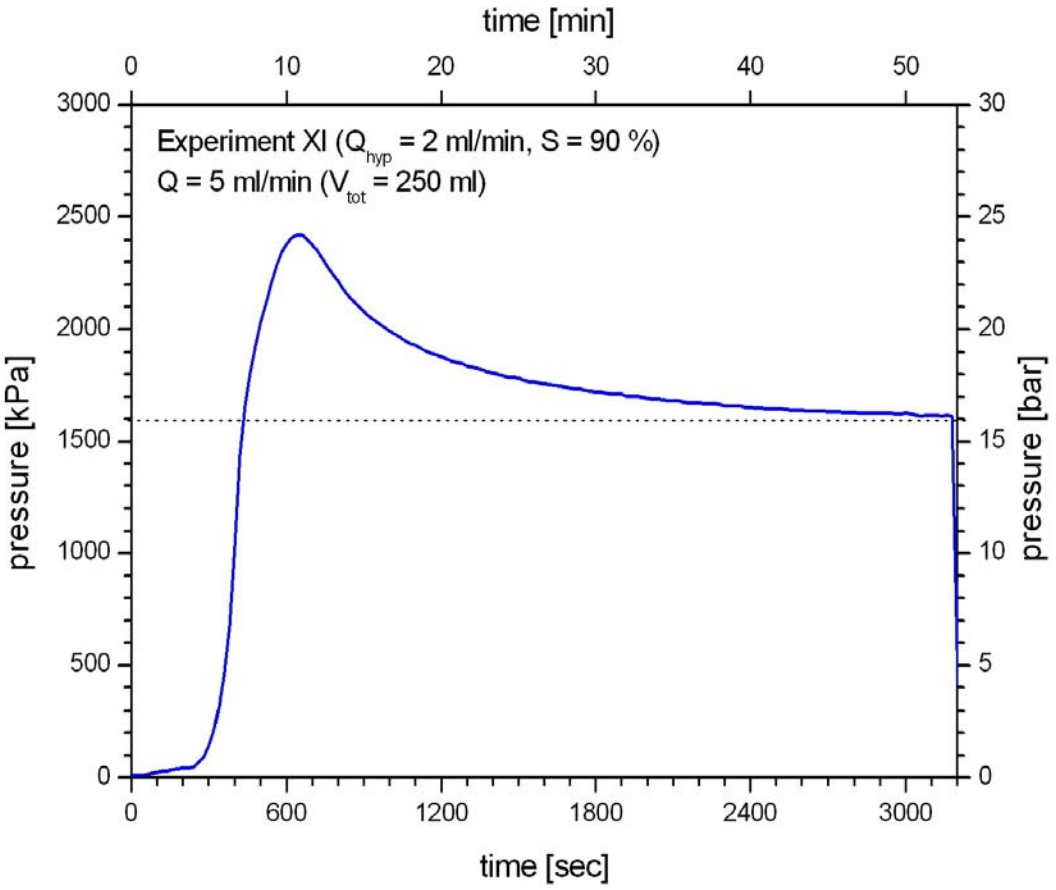

Figure 4.1: *Typical example of pressure development during the first pre-flushing stage (phase zero, distilled water). An initial pressure build-up peak is followed by the development of a constant flow - pressure relation (dashed line) indicating fully saturated steady state flow.*

In a second phase (phase 1), 250 ml bi-distilled water was pumped through the system with stepwise increasing flow rates (usually 1, 2, 3, 4, 5 sometimes 10 ml/min). The next higher flow rate was only employed after a steady state pressure had been reached before (Fig. 4.2). The first flow rate usually took longest to reach a steady state pressure. The final, steady state pressure of each flow rate was recorded and plotted against the flow rate. This allowed to check for linearity and thus the applicability of DARCY'S law. The slope of this curve was used to calculate the coefficient of hydraulic conductivity K, the intrinsic permeability k and the derived parameters (specific flux v_f, flow velocity v_a, and REYNOLDS number Re; Fig. 4.3). The highly linear curves showed that despite of the high gradients all samples exhibited fully laminar flow. The REYNOLDS numbers were accordingly always way below 1.

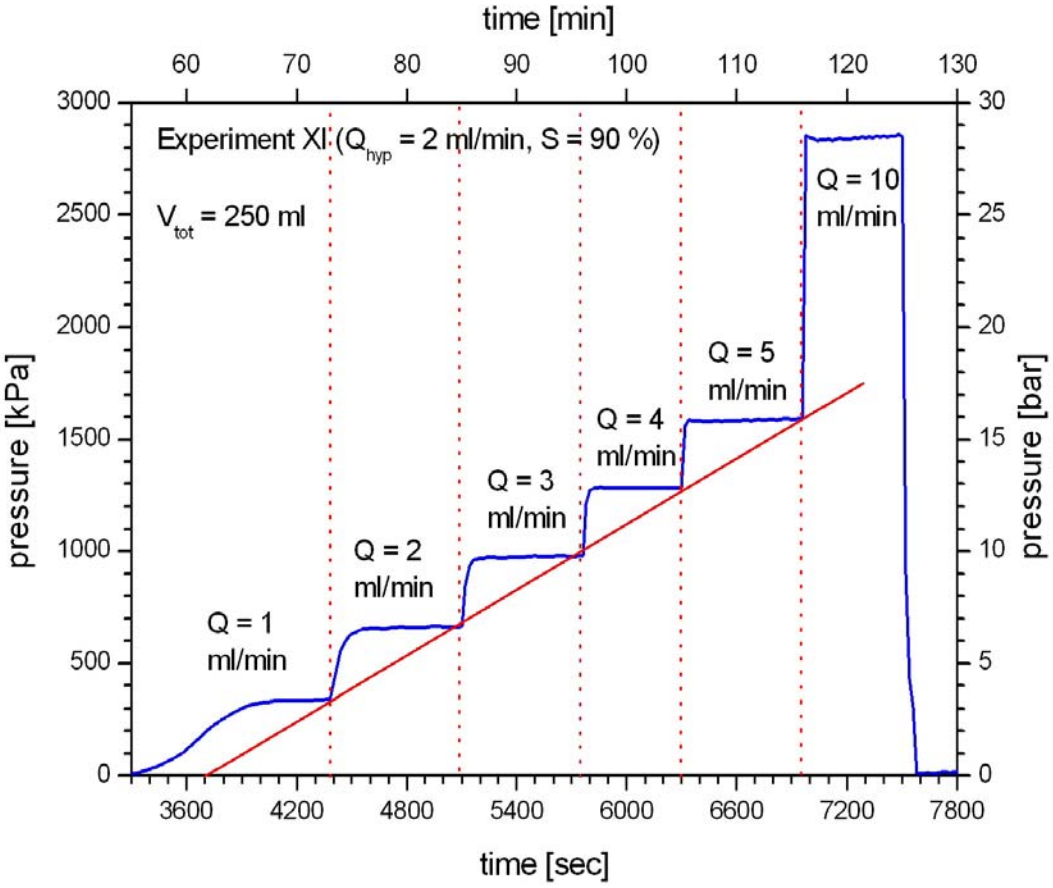

Figure 4.2: *Typical example of pressure development during the first stage (distilled water). Each flow rate results in a constant flow - pressure relation (horizontal parts of blue curve, end points connected by red line) indicating steady state DARCY flow.*

It turned out that the samples - albeit being from the same block of stone - were far from homogeneous from a hydraulic point of view. The hydraulic conductivities calculated after DARCY from the second stage of the experiments showed a rather wide range over more than one order of magnitude (K_{max} / K_{min} = 14.4). The main parameter causing this is the varying bulk density which is in the range between 2.10 and 2.26 g/cm³ (Fig. 4.4). The mean and median conductivities are $8.31 \cdot 10^{-9}$ and $4.52 \cdot 10^{-9}$ m/s, respectively. The variable conductivity makes inter-comparisons amongst different experiments at least more difficult.

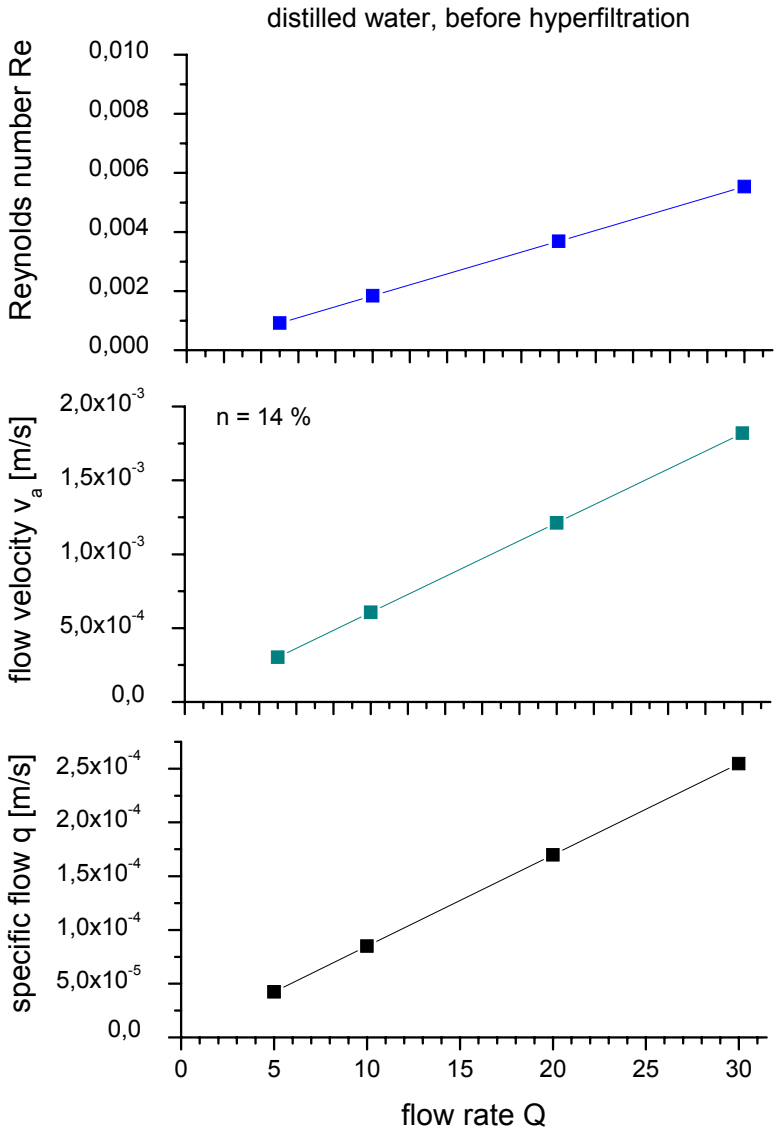

Figure 4.3: *Specific flow (DARCY velocity), flow velocity and REYNOLDS number as function of flow rate (first stage of experiment, distilled water).*

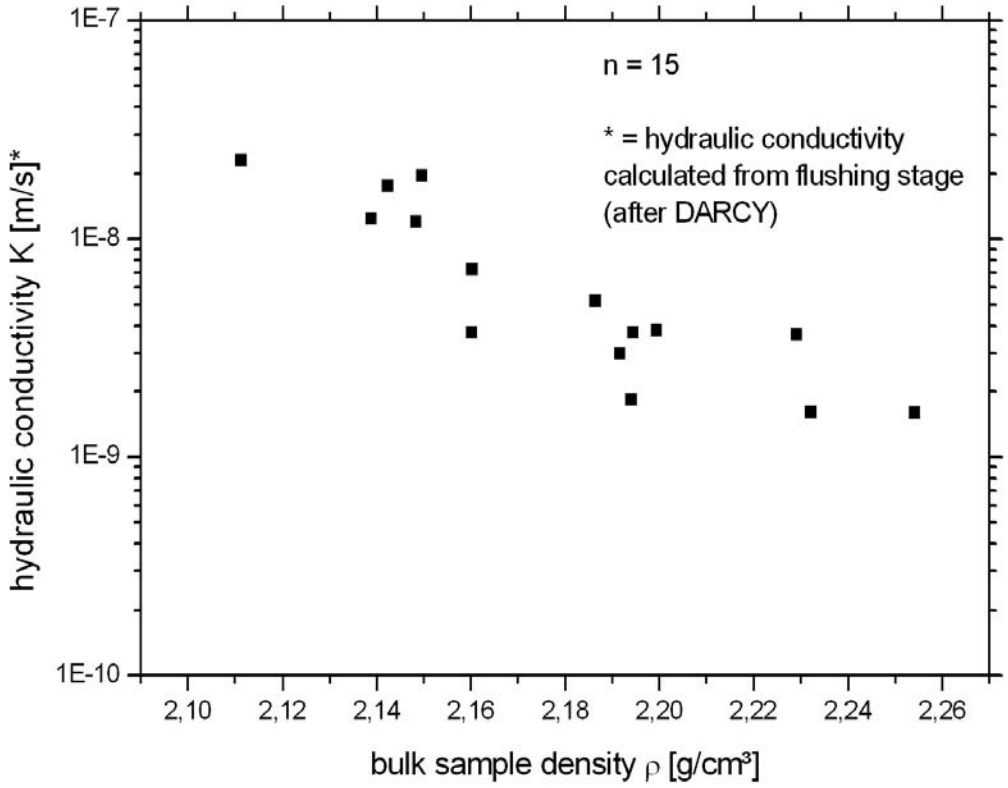

Figure 4.4: *Correlation between bulk density and hydraulic conductivity.*

The measurements of porosity and specific surface area for each untreated sample allowed calculations of the hydraulic conductivity after KOZENY-CARMAN [Eq. 2.8]. These values can then be compared to the measured hydraulic conductivities after DARCY from the actual experiments (phase 1). Figure 4.5 shows that the correlation is not well pronounced but that both methods at least result in conductivities in the same range.

The second (main) stage was the actual hyperfiltration phase. The piston pump was therefore filled with 250 ml nickel sulphate solution. A sample of the solution was taken beforehand to allow referencing the passing solution to the initial solution. Measurements of the specific electrical conductivity indicated the imminent breakthrough of the solution and gave good indication on when to sample. In all cases we noticed a steep increase of both the conductivity and the pressure. Both values reached a plateau value after some time. A commonly observed decrease of both values just before the end of the piston was reached (see e.g. Figures 4.6, 4.7) is due to an unavoidable artefact. Some distilled water remains in the end socket of

the piston which dilutes the last few millilitres of the nickel sulphate solution. Therefore the previously obtained plateau values for pressure, conductivity and (nickel and sulphate) concentrations were used for all further calculations.

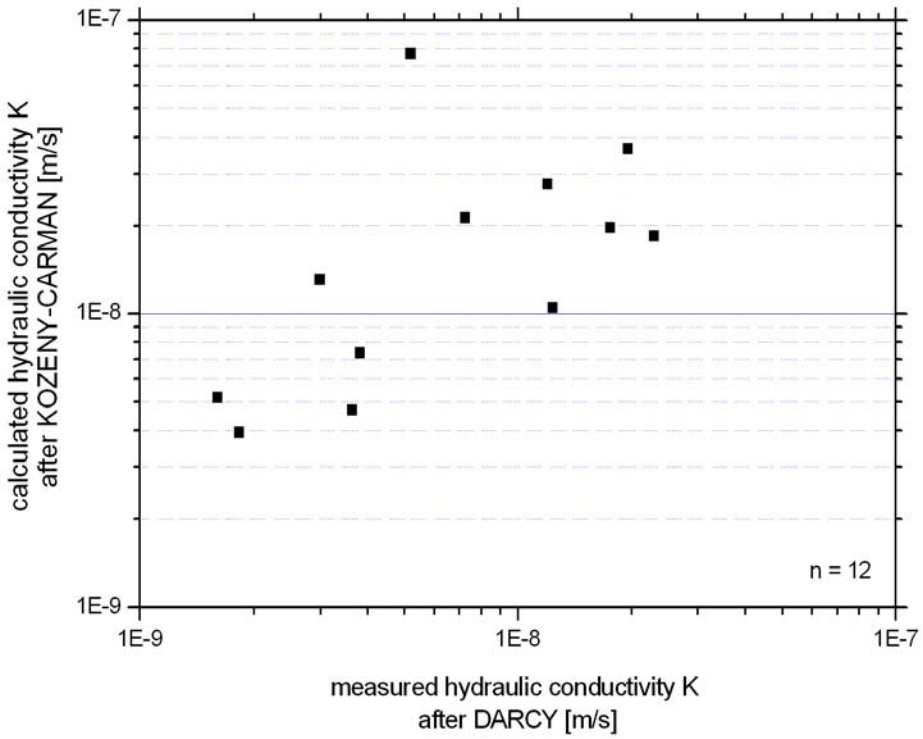

Figure 4.5: *Correlation between measured hydraulic conductivity after DARCY and calculated hydraulic conductivity after KOZENY-CARMAN [Eq. 2.8]. For the latter, porosities from mercury porosimetry and specific surface areas from nitrogen adsorption (BET) were used (Tab. 3.1). Geometry factor = 2.0 and tortuosity = 0.7.*

The pressures during the hyperfiltration phase were always the highest during the whole experiment. They can be related - at least initially - to the osmotic back pressure developing between the nickel sulphate solution on the high pressure side of the sample and the water on the other side. After the breakthrough of the solution this osmotic back pressure must diminish significantly since now a solution of high salinity is present on both sides. The remaining pressure increase must therefore be due to:

- ❖ osmotic back pressure between solution on low pressure side and the solution in the concentration polarization layer on the high pressure side
- ❖ permeability damage caused by mineral precipitation in pore spaces

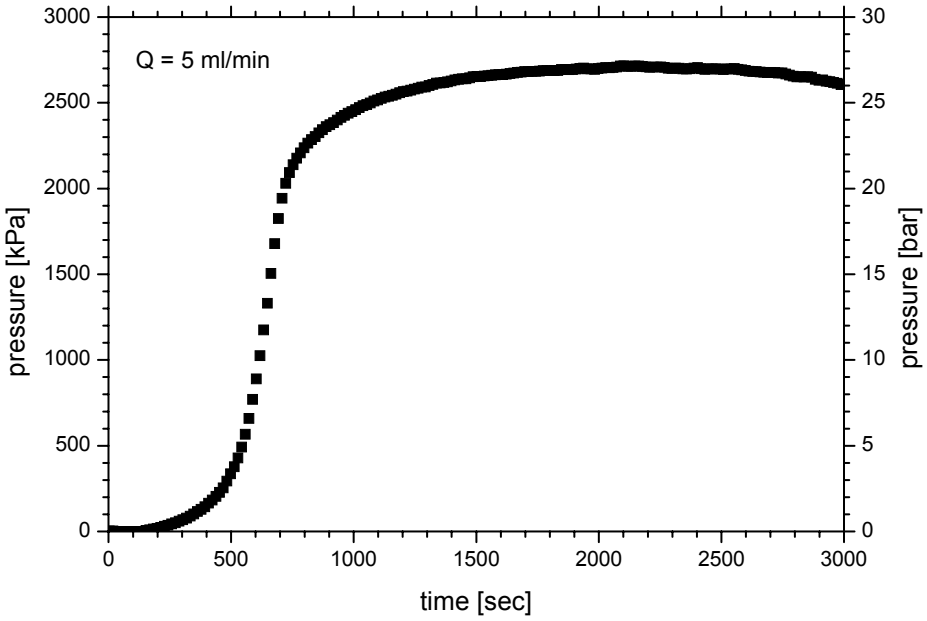

Figure 4.6: *Pressure development during the main (hyperfiltration) stage of the experiment (Q_{hyp} = 5 ml/min, S = 70 %).*

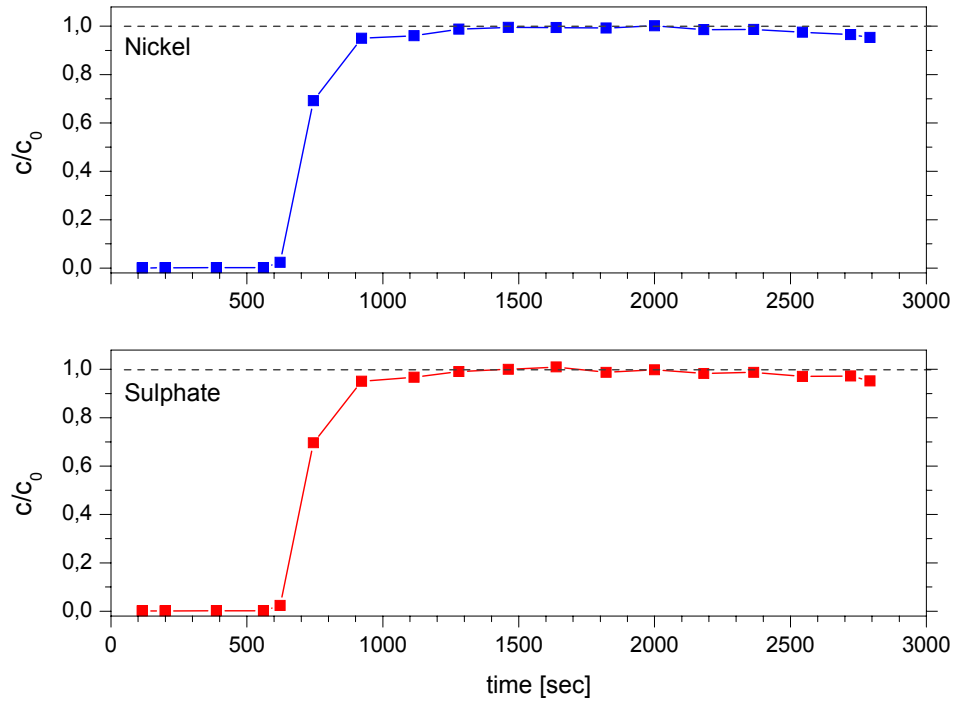

Figure 4.7: *Breakthrough curves of nickel and sulphate during the main (hyperfiltration) stage of the experiment (Q_{hyp} = 5 ml/min, S = 70 %).*

For the third (re-flushing) phase, the piston was again filled with 250 ml bi-distilled water. It was pumped through the system in stepwise increasing flow rates (usually 1, 2, 3, 4 and 5 ml/min). The first flow rate was maintained until the conductivity had fallen significantly (breakthrough of water) and the osmotic back pressure could thus be considered to be relatively small. Again, the next higher flow rate was only employed after a steady state pressure had been reached previously (Fig. 4.8). The final, steady state pressure of each flow rate was recorded and plotted against the flow rate (Fig. 4.9). In most cases this plot showed no linear behaviour. The relatively decreasing pressures are an indication of increasing hydraulic conductivities, obviously due to the dissolution of some nickel sulphate precipitates from the pore space. In the ideal case all precipitates should re-dissolve during the re-flushing stage (full reversibility). The pressures for each flow rate should then finally be equal to the ones observed during the second stage of the experiments. This was only achieved once for an experiment with a very low degree of solute saturation (Q_{hyp} = 5 ml/min, S = 10 %). In all other experiments the 250 ml of distilled water (≈ 36 pore volumes) never were enough to obtain this.

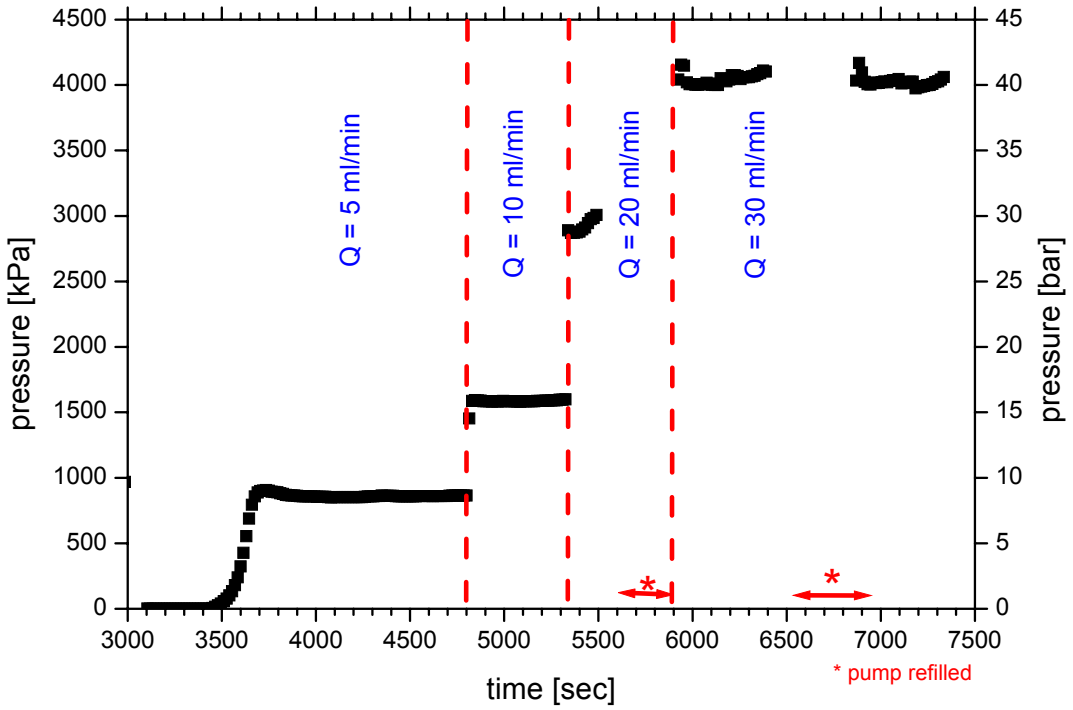

Figure 4.8: *Typical example of pressure development during the third phase (re-flushing with distilled water). Each flow rate results in a constant flow - pressure relation (horizontal parts of black curves) indicating steady state flow (Q_{hyp} = 5 ml/min, S = 70 %).*

In order to quantify the reversibility of the precipitation-induced damage to the hydraulic conductivity, we divided the final pressure of each flow rate for the re-flushing phase by the final pressure obtained for the same flow rate in phase 2 (bi-distilled water). The obtained value is the so called r_K value (= residual conductivity, ratio of post-filtration vs. initial conductivity). A r_K value of 1.00 would indicate full reversibility of the hyperfiltration-induced permeability damage.

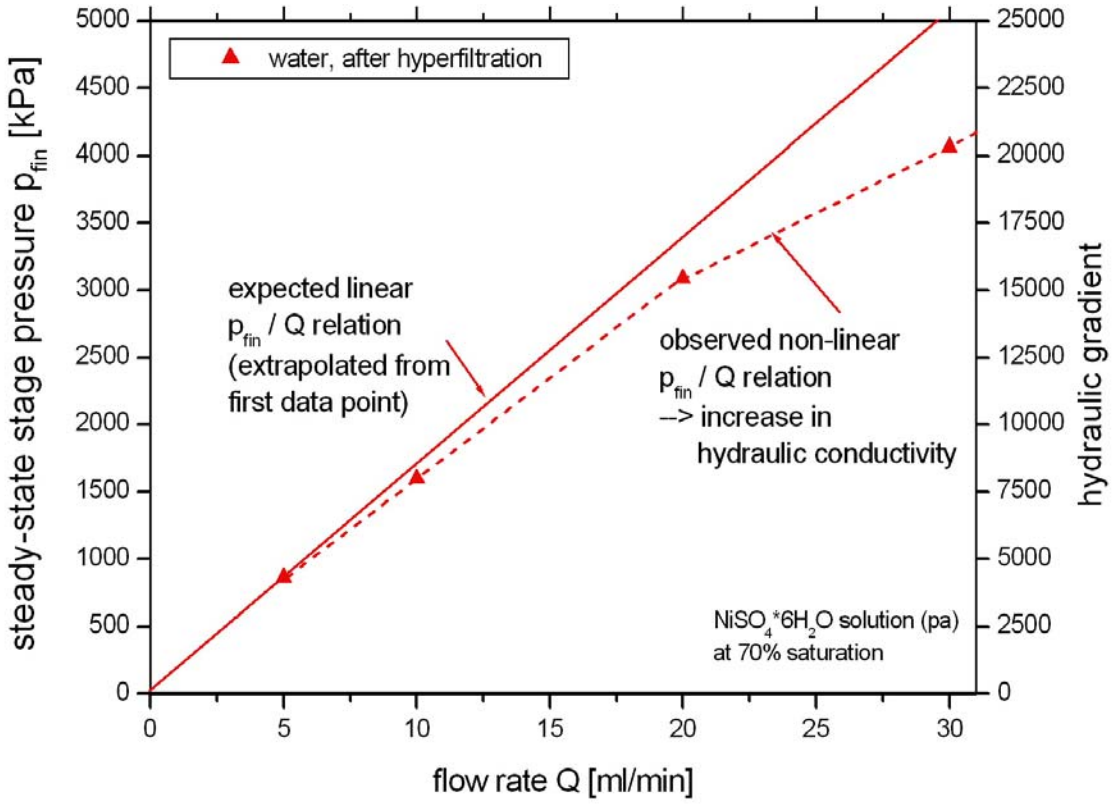

Figure 4.9: *Plot of steady state stage pressures observed during re-flushing (third phase) of a sample after hyperfiltration (Q_{hyp} = 5 ml/min, S = 70 %).*

We performed one experiment (Q_{hyp} = 5 ml/min, saturation $NiSO_4$ = 70 %) where we flushed the sample after hyperfiltration with 11 consecutive piston volumes of bi-distilled water (= 2750 ml or more than 400 pore volumes) at a constant flow rate of 5 ml/min. The specific electrical conductivity never came down to the value of bi-distilled water (0.2 µS/cm) which indicates constant re-dissolution of precipitated nickel sulphate crystals. Hydrochemical analyses of five samples collected at different times accordingly show that their almost constant electrical conductivity (≈ 30-40 µS/cm) is a result of dissolving nickel sulphate and not of dissolving

carbonate as one may suspect (Tab. 4.2). The pressure needed to push the water through the sample nevertheless never came down and remained practically constant. This is a strong indication that the permeability damage is practically irreversible.

Table 4.2: Hydrochemical analyses of five samples collected during extended re-flushing of a sample after hyperfiltration (Q_{hyp} = 5 ml/min, saturation $NiSO_4$ = 70 %).

ID	**spec. el. conductivity**	**Mg**	**Ca**	**SO_4**	**Ni**
	µS/cm	mg/l			
XV1	43	0.074	0.152	17.8	10.1
XV2	39	0.003	0.034	15.8	9.17
XV3	30	0.003	0.032	11.3	6.86
XV4	40	0.002	0.030	14.8	9.14
XV5	40	0.002	0.033	15.3	9.36

Finally we combined the results of the three main experimental phases (1, 2, 3) into one diagram of the type presented in Figure 4.10. The diagrams and data for all other experiments can be found in Annexes A and B. The blue symbols give the final stage pressures obtained during phase 2 (distilled water). The blue line is the linear line of best fit for these values. It practically always shows a very high linear correlation ($r^2 > 0.98$) and thus indicates fully laminar Darcy flow. The black symbol shows the final pressure obtained during hyperfiltration (third phase). It is always higher than the pressures noted during the previous phase. Finally, the red points are the steady-state stage pressures obtained during the re-flushing phase (phase 3). The dotted red line indicates an expected linear relation for the re-flushing stage extrapolated form the zero point and the first red data point. The difference between the blue and red symbols indicates the amount of hydraulic permeability reduction induced by the precipitation (grey shaded area). The r_K values are also given as numbers above the red symbols. The difference between the solid and the dotted red line shows the hydraulic effect of the re-dissolution (flushing) of some of the nickel sulphate precipitates.

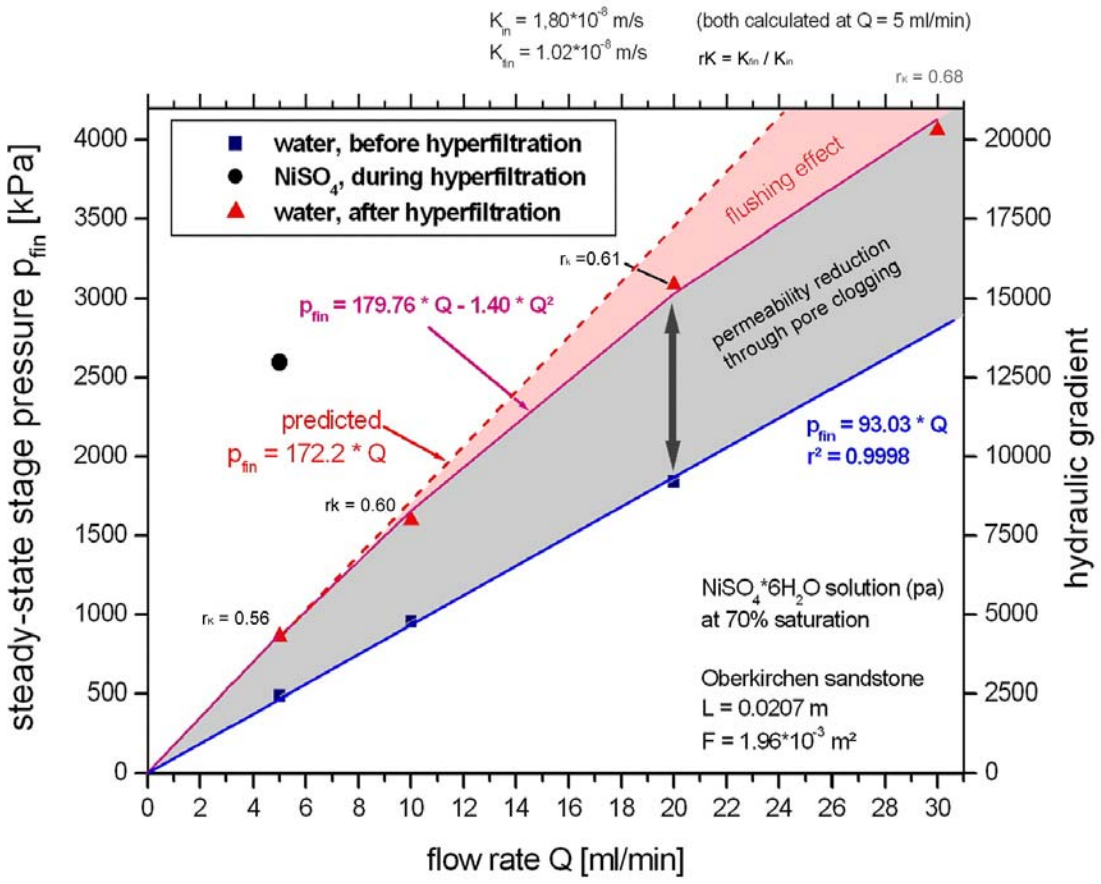

Figure 4.10: *Comparison of pressure development for all experimental phases (Q_{hyp} = 5 ml/min, S = 70 %).*

Due to the experimental set-up we could not sample the concentration of the solution at the high-pressure side of the membrane after hyperfiltration directly (the set-up is being re-designed to allow this in future experiments). Therefore we could not employ Equations [2.13] to calculate reflection coefficients. The reflection coefficients calculated after Equation 2.14 using the measured concentrations showed no consistent results (Fig. 4.11). From theory one should expect that the reflection coefficient (or in other words the membrane efficiency) should decrease with increasing solute concentration (or saturation). For Q_{hyp} = 5 ml/min (Fig. 4.11 b) this is more or less visible disregarding the value at 90 % saturation. For Q_{hyp} = 2 ml/min (Fig. 4.11 a) no obvious trend is visible. Considering the relatively high hydraulic conductivity of our samples - compared to clays - one might still safely assume that the reflection coefficients of the sandstone samples should be very low (< 0.1). The low membrane efficiency should cause only small concentration increases of the hyperfiltrated solution (Fig. 2.7) and make higher degrees of saturation necessary to cause precipitation. Therefore it is quite surprising that solute saturations as low as

30 % are sufficient to cause noticeable mineral precipitation and permeability damages.

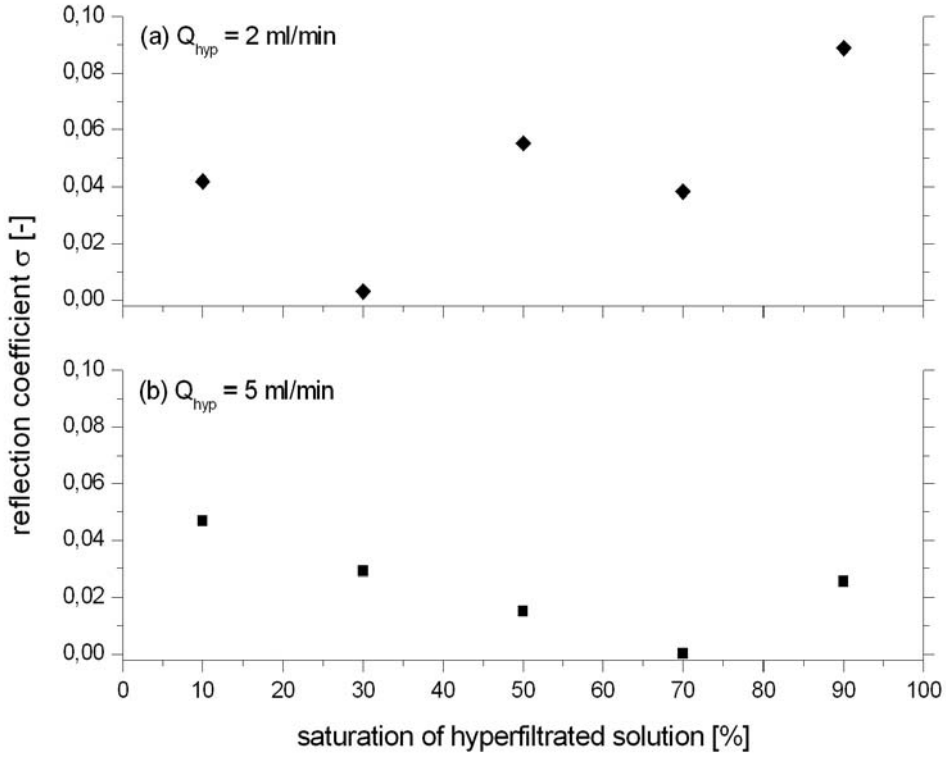

Figure 4.11: *Reflection coefficients σ for $NiSO_4$ calculated after Equation [2.14] for (a) Q_{hyp} = 2 ml/min and (b) Q_{hyp} = 5 ml/min.*

Figure 4.12 shows the residual hydraulic conductivities as a function of solute saturation. Both hyperfiltration flow rates yield very similar results. The hyperfiltration-induced damage to hydraulic conductivity is clearly a function of solute saturation. Higher saturations result in higher conductivity losses. Full reversibility is only obtained at saturations below 30 %. The curve shape indicates that at saturations above 50 % damage increases drastically and that reversibility is only slight. This is in good accordance with the predictions resulting from Figure 2.7. This figure shows that membranes of low ideality - such as our sandstone samples - should only be able to increase the concentration in the CPL by a factor of two. A solution should then have at least a saturation of around 50 % to attain super-saturation.

As expected, the pressures obtained during the hyperfiltration phase are clearly a function of solute saturation (Fig. 4.13).

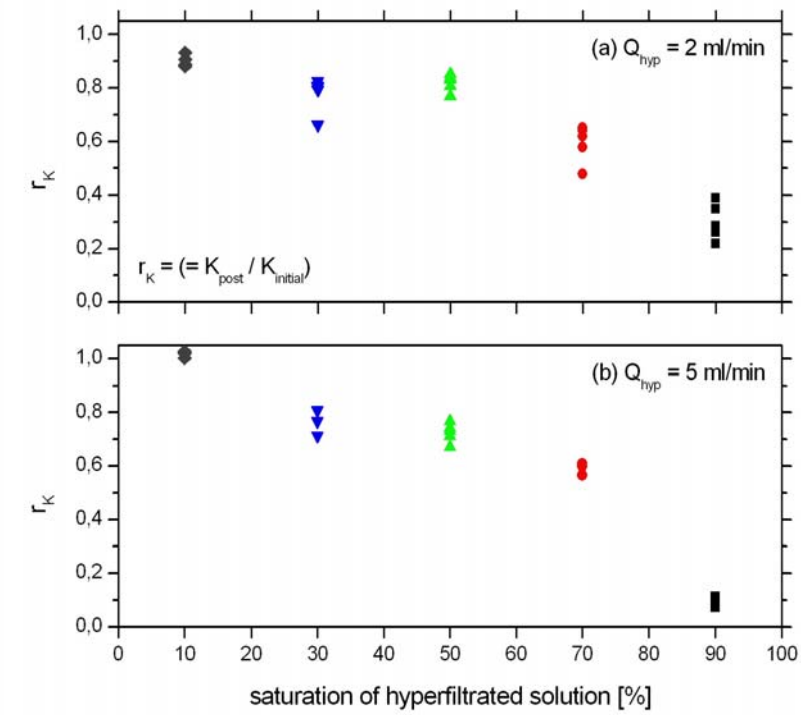

Figure 4.12: *Residual hydraulic conductivities (for all flow rates) as a function of solute saturation. Calculated as ratio between final stage pressure during re-flushing (phase 3) and during phase 1 (water filtration) for (a) Q_{hyp} = 2 ml/min and (b) Q_{hyp} = 5 ml/min.*

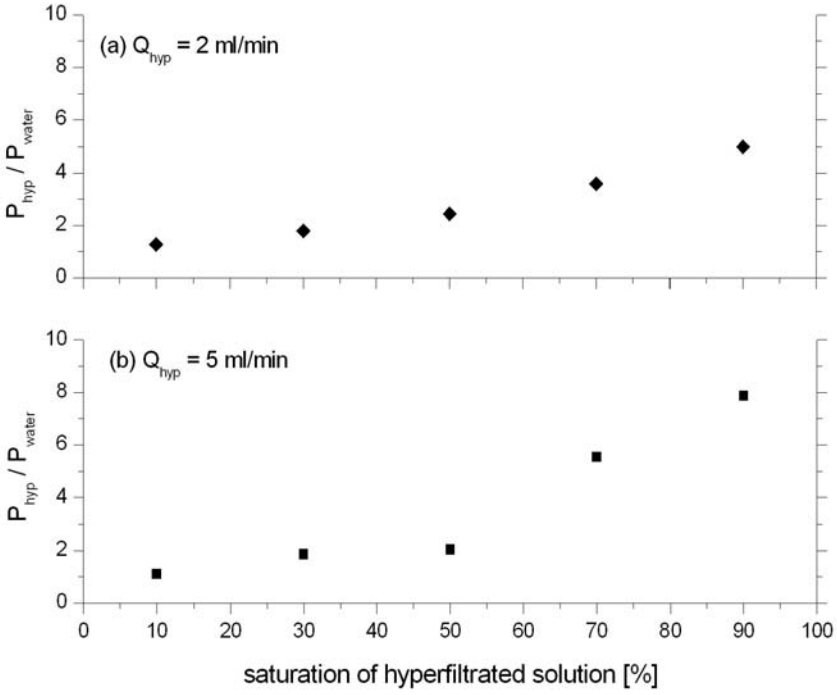

Figure 4.13: *Ratio between final stage pressure during hyperfiltration (phase 2) and during phase 1 (water) for (a) Q_{hyp} = 2 ml/min and (b) Q_{hyp} = 5 ml/min.*

Equation 2.5 might be employed in systems where a thin layer of precipitates affects the total hydraulic conductivity while the remainder of the sample retains the original conductivity. Assuming that the hydraulic conductivity was only changed in one layer and knowing the initial and the final vertical hydraulic conductivity of the whole sample and the thicknesses of both layers (e.g. from geochemical investigations → 5) one might solve Equation [2.5] for the conductivity of the clogged layer. Figure 4.14 shows some indications that its conductivity is a function of the saturation of the hyperfiltrated solution.

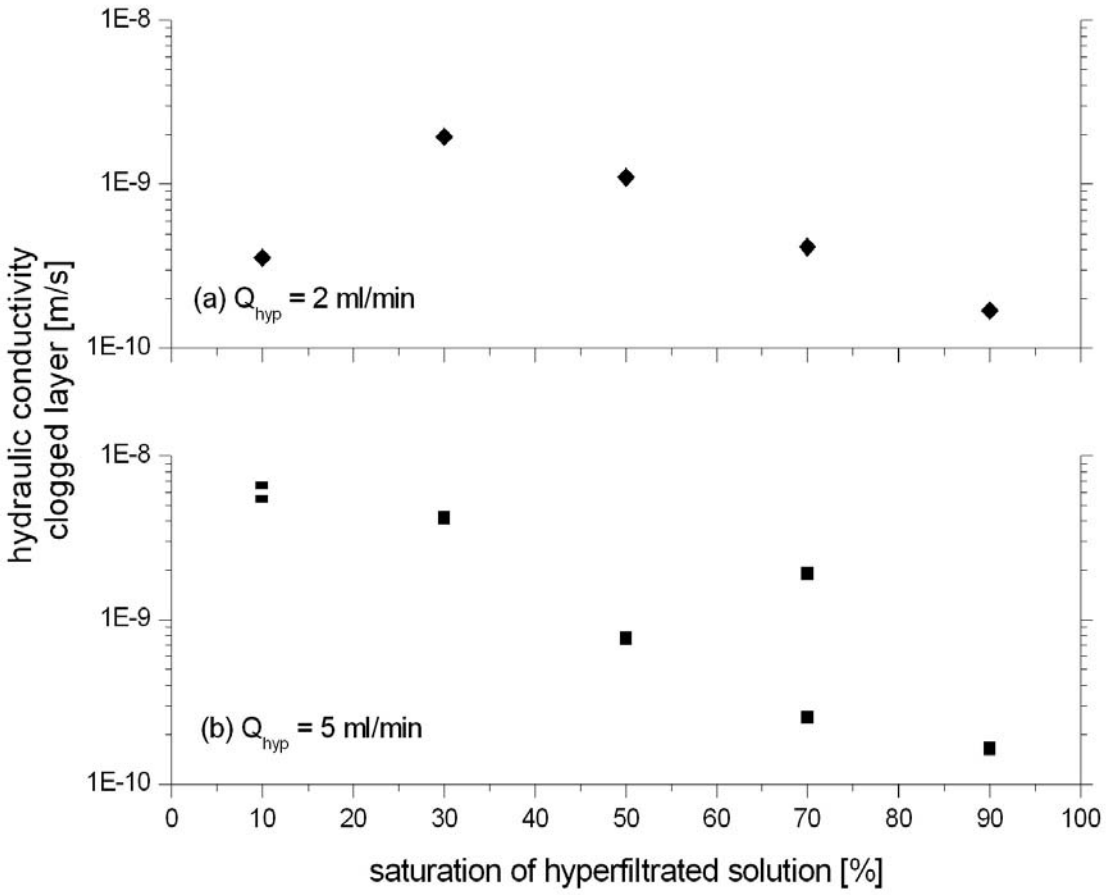

Figure 4.14: *Hydraulic conductivity of a 2 mm clogging layer for (a) Q_{hyp} = 2 ml/min and (b) Q_{hyp} = 5 ml/min.*

5 Post-mortem study of samples

5.1 Mass gain

The simplest way to assess changes to the samples induced by the hyperfiltration process is to measure the difference in mass before and after the experiments. The sample weight was recorded for the dry samples before and afterwards (following freeze-drying). The difference in mass must be due to precipitates that formed in the pore spaces. Figure 5.1 shows that there is a trend visible for both hyperfiltration flow rates (Q_{hyp}) that suggests an increasing amount of precipitate with increasing solute saturation. Unfortunately one unexplained outlier (5 ml/min, 90 %) affects the overall statistical significance of this general observation. The hyperfiltration flow rate (Q_{hyp}) itself seems to have no significant influence on the amount of precipitates as a comparison of Figures 5.1 a and 5.1 b shows.

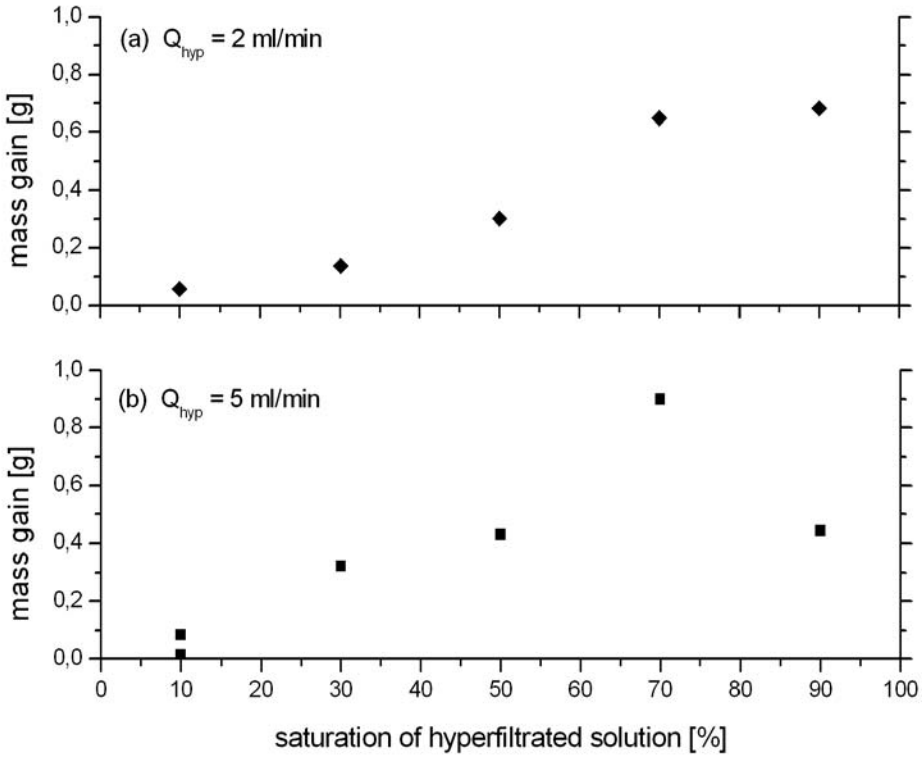

Figure 5.1: *Mass gain induced by hyperfiltration as a function of solute saturation (mass gain is calculated as difference between sample mass before and after the experiments).*

If we omit the outlier in Figure 5.1 we find that a higher flow rate results in a steeper correlation between saturation and mass gain. One might suspect that the amount of precipitated minerals is also a function of hydraulic sample conductivity with samples of lower permeability attracting higher amounts of precipitates. Figure 5.2 shows that this is not the case. Obviously, solute saturation is more important than sample permeability.

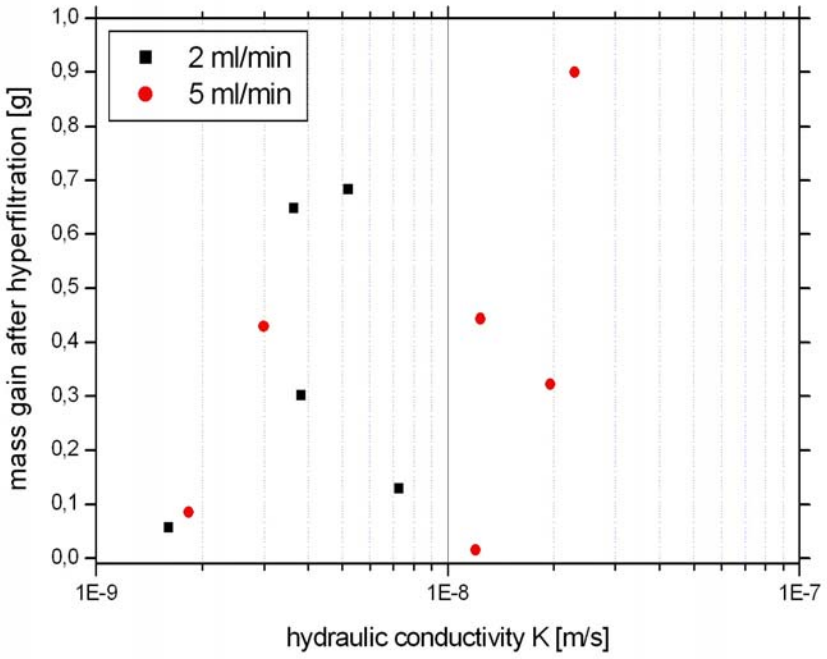

Figure 5.2: *Mass gain induced by hyperfiltration as a function of initial hydraulic conductivity (mass gain is calculated as difference between sample mass before and after the experiments).*

The mass gain of the sandstone samples after hyperfiltration is very small compared to the total dissolved mass hyperfiltrated through it in the course of the experiment (Tab. 5.1). The percentage of mass removed from solution by mineral precipitation is always well below 1 %.

Table 5.1: Mass gain of samples after hyperfiltration compared to total dissolved mass in hyperfiltrated solution.

Saturation S	hyperfiltrated mass $NiSO_4$ M*	Q_{hyp} = 2 ml/min		Q_{hyp} = 5 ml/min	
		mass gain [g]	fraction of total hyperfiltrated mass [%]	mass gain [g]	fraction of total hyperfiltrated mass [%]
[%]	[g/l]				
10	16.25	0.06	0.37	0.09	0.55
30	48.75	0.13	0.27	0.32	0.66
50	81.25	0.30	0.37	0.43	0.53
70	113.75	0.65	0.57	0.90	0.79
90	146.25	0.68	0.46	0.45	0.31

* dissolved in 250 ml distilled water

5.2 Imaging with environmental scanning electron microscope

Images obtained using a scanning electron microscope showed that pore spaces are often rimmed of even blocked by small (1-2 µm) and light (= higher density compared to quartz) grains with ill-defined crystal faces (Fig. 5.2). The latter fact could be an indication of dissolution processes which obscure the crystal faces. EDX analyses clearly identified the precipitates as phase consisting of nickel and sulphur (Fig. 5.3).

Qualitatively, we found that more precipitates were visible in the lower parts of the sample than in the upper parts.

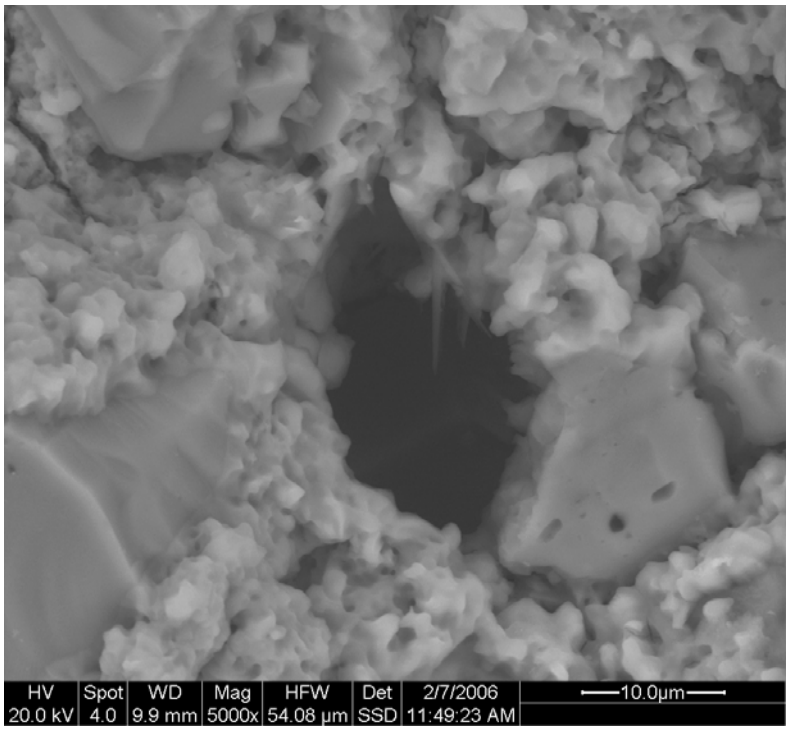

Figure 5.2: *Scanning electron microscope (SEM) picture of the lower face of a sample after hyperfiltration (Q_{hyp} = 5 ml/min; S = 70 %). The larger, evenly faced grains are quartz, the small, ill-defined lighter material $NiSO_4$ precipitates. Note the open pore in the centre of the picture.*

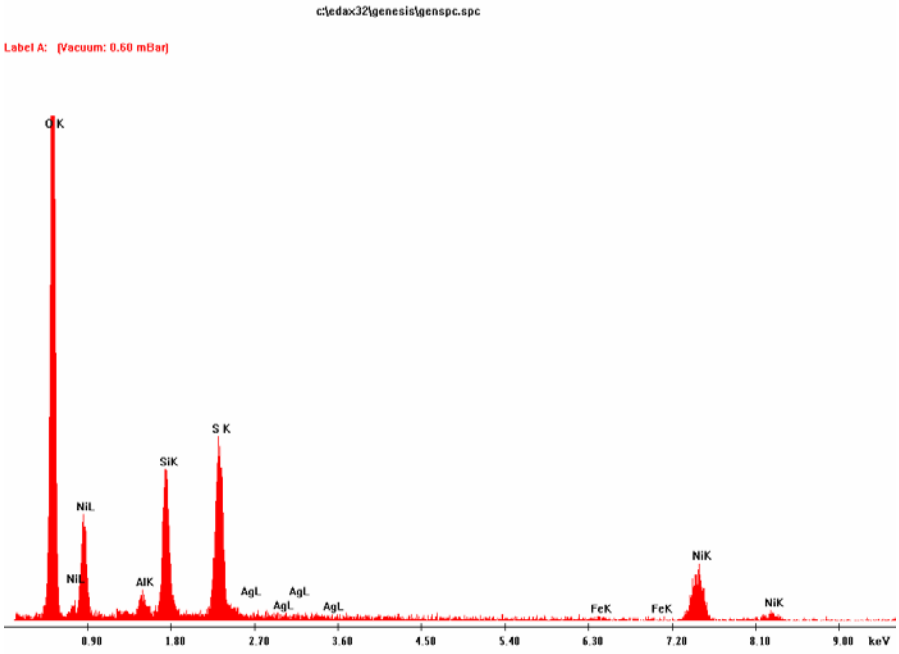

Figure 5.3: *EDX element plot of the precipitates of the preceding figure using the scanning electron microscope (SEM). Nickel and Sulphur are identified as main components, silicon and aluminium are from silicate minerals of the background.*

5.3 Element mapping

The distribution of nickel - as indicator of hyperfiltration-induced precipitates - was investigated using the X-ray microscope and the X-ray geoscanner. Whilst the former results in a 2 D map of element distribution (Fig. 5.4) the latter gives a geochemical line profile (Fig. 5.5). The reader should be aware that both methods only give semi-quantitative concentrations which make quantitative comparsions between different samples at least difficult. This is e.g. due to effects of surface roughness which may differ from sample to sample (note that the surfaces are not polished in any way and thus have differing surface morphologies).

(a) X-2-10	(b) IX-2-30	(c) I-5-70	(d) XI-2-90
			
Q_{hyp} = 2 ml/min S = 10 %	Q_{hyp} = 2 ml/min S = 30 %	Q_{hyp} = 5 ml/min S = 70 %	Q_{hyp} = 2 ml/min S = 90 %

Figure 5.4: *2-D element mapping of spatial nickel distribution (light) in samples after hyperfiltration using the ITRAX X-ray microscope (flow direction from bottom to top of pictures, height of sample in picture = 20 mm).*

Both figures show that nickel is indeed detectable in the sample after hyperfiltration and re-flushing. Elevated concentrations immediately at the bottom and top faces are probably artefacts due to the experimental set-up and the sample treatment. More interesting is the elevated nickel content in the lower two to three millimetres of the sample (at least visible in Figures 5.4 a, b and c). They probably show the depth of

precipitate penetration into the sample. The concentrations show a linear decrease with increasing depth.

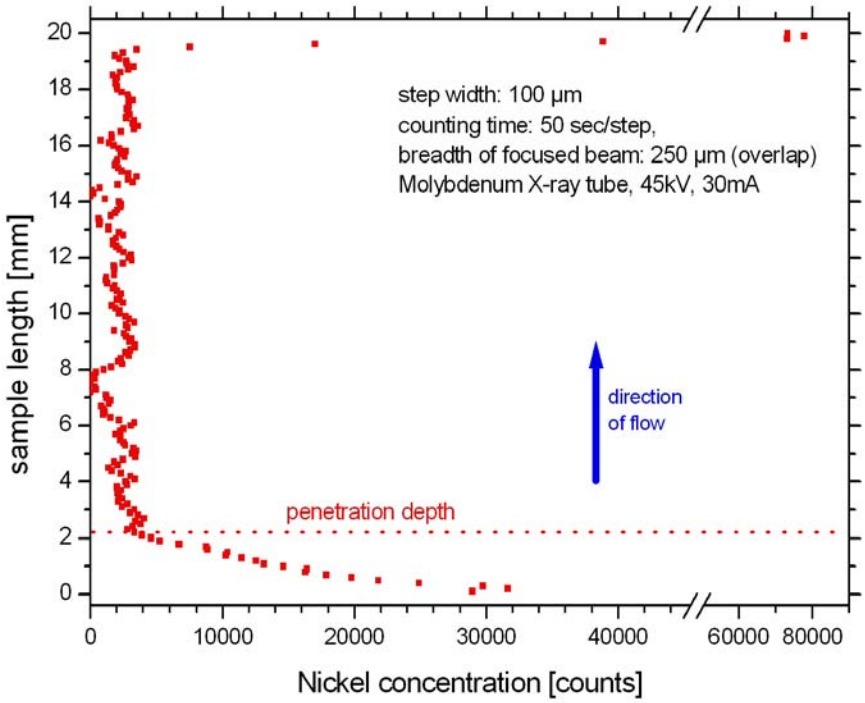

Figure 5.5: *Element profile (line scan) of nickel in a sample after hyperfiltration (Q_{hyp} = 5 ml/min, 70 %) using the ITRAX X-ray geoscanner (same sample as in Fig. 5.4).*

5.4 Porosity distribution

The decrease in hydraulic conductivity in the cause of the experiments was a result of a reduction in porosity through the precipitation of nickel sulphate crystals. Therefore we expected that samples would have a lower porosity, smaller average pore radii and higher mineral densities after the experiments. From the element distribution mapping (→ 5.3) we know that the precipitates are restricted to a small layer at the bottom of the samples. Therefore we performed mercury porosimetry on small (2 mm) slices sawed off (dry) from the bottom of the samples and on material from the "undisturbed" middle. Only experiments with higher saturation rates were considered.

The results are summarised in Table 5.2 and do not support the expectations. In half the cases porosity and average pore radii apparently increased while the mineral

density decreased or remained practically constant. This unexpected result could be attributed to several possible causes:

- ❖ method inappropriate (injected mercury displaces nickel sulphate?)
- ❖ bottom part of sample had initially higher porosity (loosened through drilling during sample preparation and/or sawing)

Table 5.2: Mercury porosimetry on sample material after the experiments (bottom = material sawed off from the lowermost 2 mm of the sample, “middle” = material from the unaffected middle of the core).

Experiment		**IV-2-70**		
		middle	bottom	difference
porosity	%	15.4	15.6	+ 0.2
average pore radius	µm	1.163	1.306	+ 0.143
mineral density	g/cm³	2.633	2.630	- 0.003
Experiment		**XI-2-90**		
		middle	bottom	difference
porosity	%	15.9	15.6	- 0.3
average pore radius	µm	1.699	1.434	- 0.265
mineral density	g/cm³	2.593	2.598	+ 0.005
Experiment		**XV-5-70**		
		middle	bottom	difference
porosity	%	19.2	20.2	+ 1.0
average pore radius	µm	1.697	1.837	+ 0.140
mineral density	g/cm³	2.633	2.643	+ 0.010
Experiment		**XII-5-90**		
		middle	bottom	difference
porosity	%	19.5	18.0	- 1.5
average pore radius	µm	1.523	1.589	+ 0.066
mineral density	g/cm³	2.640	2.619	- 0.021

The relative pore volume as a function of pore size also gives little insight into the changes in porosity (Fig. 5.6). The calculated differences (Fig. 5.6, lower diagram) do

not show any significant rearrangement of pore structure between the two samples and are more likely related to some natural variation.

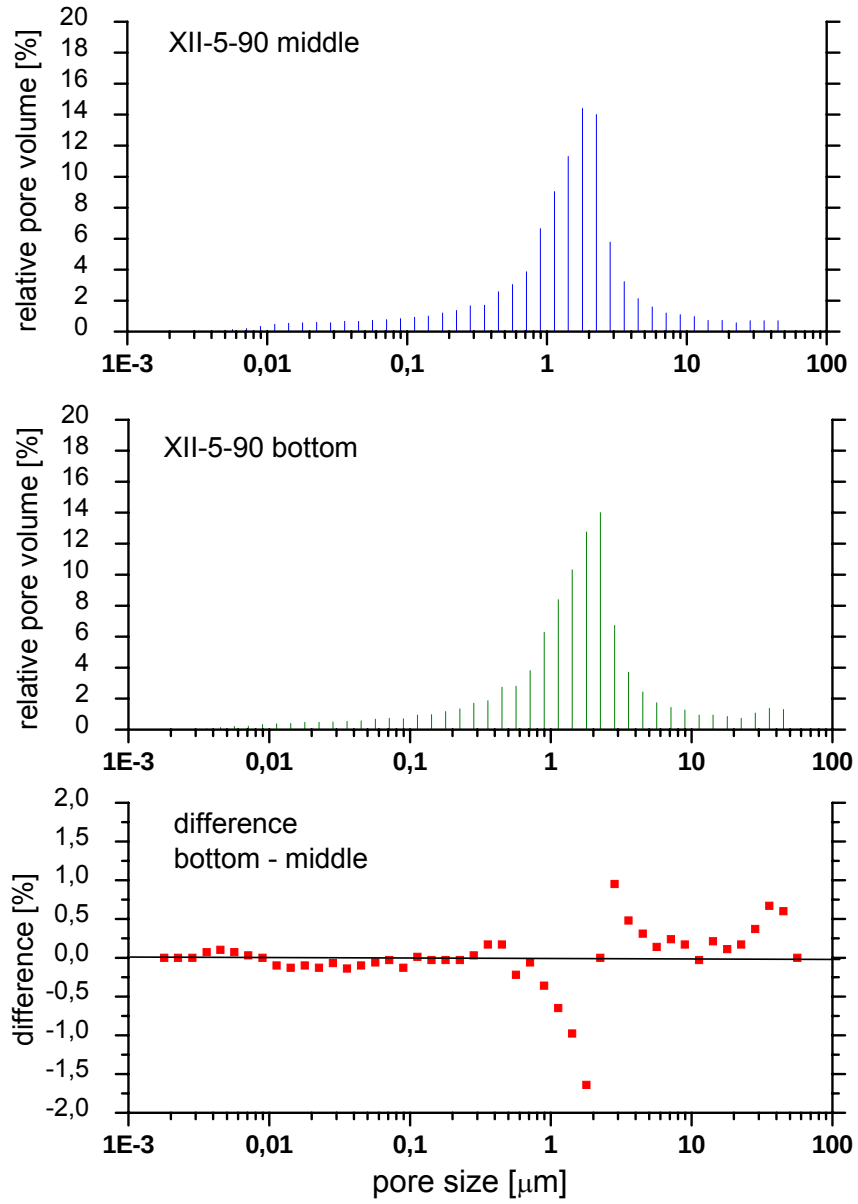

Figure 5.6: *Comparative results of mercury porosimetry analysis: relative pore volume distribution as a function of pore size in samples from middle and bottom (lower 2 mm) of core after hyperfiltration (Experiment XII, Q_{hyp} = 5 mL/min, S = 90%).*

The pore size distributions of all other samples are presented in Annex C.

6 General interpretation of results

6.1 Occurrence of hyperfiltration precipitates

The experiments conclusively showed that hyperfiltration-induced mineral precipitation occurs even in the relatively - compared to clay - permeable sandstone samples used in this study. The main precipitation occurs in a small layer at the bottom (inflow) of the samples. This layer is probably identical with the concentration polarisation layer (CPL).

6.2 Porosity and permeability damage caused by precipitates

Degrees of solute saturation as low as 10 % $NISO_4$ were found to be sufficient to cause measurable effects on the hydraulic conductivity of the sample. We found strongly increasing precipitation and resulting permeability damages with increasing solute saturation, especially above 50 %. Calculations showed that the precipitates cause a decrease in hydraulic conductivity of the thin precipitation zone by two orders of magnitude lower compared to the unaltered rest of the sample. The method employed to assess the porosity reduction in the CPL zone (mercury porosimetry) turned out to be unsuitable for this purpose.

6.3 Reversibility of permeability damage

As noted before, the permeability damage induced by the precipitates was only fully reversible for very low degrees of solute saturation (10 %). Reversibility decreased with increasing solute saturation.

One would expect that all precipitates should eventually re-dissolve due to the high solubility of nickel sulphate. On the contrary, the long-term re-flushing experiment mentioned in Chapter 4 showed that this is probably not the case - even for extended times and volumes of re-flushing. Figure 6.1 shows a possible explanation: some

pores are only partially blocked: passing water may dissolve the exposed precipitates. Other pores may be fully blocked so that water may not enter at all, especially when the pore throat is very narrow. Such pores are then not available for water migration and may retain permeability damage on the long range.

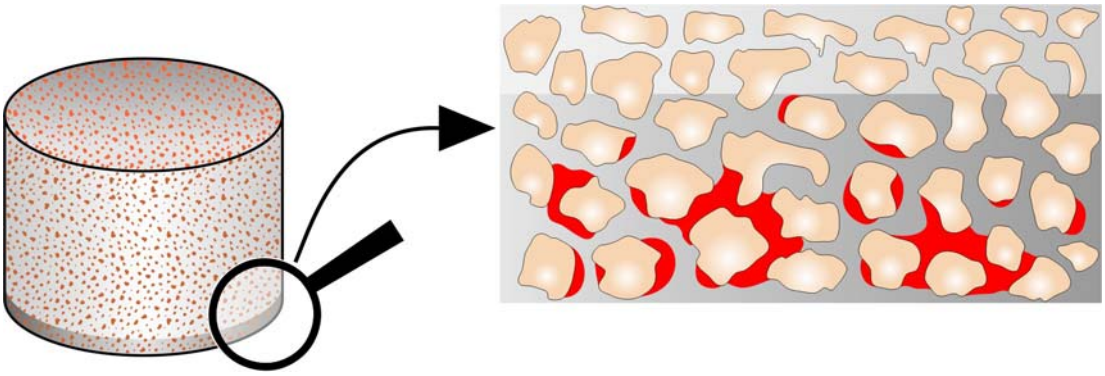

Figure 6.1: *Schematic drawing of precipitate (red) distribution in samples after hyperfiltration (light brown = quartz grains).*

7 Outlook

The experiments presented in this study dealt with sandstone samples and one type of solute (nickel sulphate). In order to transfer the results to the original aim of this investigation, the near-field of radioactive waste deposits, similar experiments have to be performed in the future with silts and clays. Since the hydraulic conductivity of such material is much lower than that of sandstones one must expect

- very low flow rates
- high pressures
- very long experimental times

In a first phase it would be better to use non-swelling clays such as kaolinite in order to be able to address permeability changes induced by hyperfiltration precipitates without the need to include effects of porosity changes induced by swelling.

The experimental set-up should be altered in such a way that samples of the liquid at the high pressure side of the sample can be taken after the experiment. This would require the installation of an additional pressure-tight capillary.

Acknowledgements

The author would like to express our gratitude to Friedhelm Schulte for his technical assistance during design and construction of the experimental equipment. Also, I would like to thank Frank Wagner and our student workers Dörte Carstens and Kateryna Skrypka for their help in performing the actual experiments.

Another “thank you” goes to Reiner Dohrmann, Stephan Kaufhold, Antje Wittenberg, Melanie Hein and Natascha Schleuning for the mineralogical analyses. Assistance in interpreting the porosimetry data by Andreas Schreiber (Porotec GmbH) is gratefully acknowledged.

8 References

Benzel, W.M. & Graf, D.L. (1984): Studies of smectite membrane behavior: Importance of layer thickness and fabric in experiments at 20° C.- Geochim. Cosmochim. Acta 48: 1769-1778.

Chapuis, R.P. & Aubertin, M. (2003): On the use of the Kozeny-Carman equation to predict the hydraulic conductivity of soils.- Can. Geotech. J. 40: 616-628.

Coplen, T.B. & Hanshaw, B.B. (1973 a): Ultrafiltration by a compacted clay membrane – I. Oxygen and hydrogen isotope fractionation.- Geochim. Cosmochim. Acta 37: 2295-2310.

Coplen, T.B. & Hanshaw, B.B. (1973 b): Studies of smectite membrane behavior: Electrokinetic, osmotic, and isotopic fractionation processes at elevated pressures.- Geochim. Cosmochim. Acta 52: 727-737.

Dickey, P.A. (1969): Increasing concentration of subsurface brines with depth.- Chem. Geol. 4: 361-370.

Demir, I. (1988): Ultrafiltration by a compacted clay membrane – I. Oxygen and hydrogen isotope fractionation.- Geochim. Cosmochim. Acta 37: 2295-2310.

Domenico, P.A. & Schwartz, F.W. (1990): *Physical and chemical hydrogeology*.- New York (Wiley).

Franzen, C. & Grieser, U.J. (2002): Neue Perspektiven für die Bestimmung des Feuchtesorptionsverhaltens von Naturbausteinen.- 11th Feuchtetag Weimar.

Fritz, S.J. & Eady, C.D. (1985): Hyperfiltration-induced precipitation of calcite.- Geochim. Cosmochim. Acta 49: 761-768.

Fritz, S.J.; Hinz, D.W. & Grossman, E.L. (1987): Hyperfiltration-induced fractionation of carbon isotopes.- Geochim. Cosmochim. Acta 51: 1121-1134.

Fritz, S.J. & Whitworth, T.M. (1993): Measuring phenomenological coefficients of membranes for use in predicting osmotically-induced hydraulic pressures.- Hydrol. Sci. Technol. 8 (1-4): 1-10.

Fritz, S.J. & Whitworth, T.M. (1994): Hyperfiltration-induced fractionation of lithium isotopes: ramifications relating to representativeness of aquifer sampling.- Water Resources Res. 30 (2): 225-235.

Graf, D.L. (1982): Chemical osmosis, reverse chemical osmosis, and the origin of subsurface brines.- Geochim. Cosmochim. Acta 46: 1431-1448.

Hansen, D. (2004): Discussion of “On the use of the Kozeny-Carman equation to predict the hydraulic conductivity of soils”.- Can. Geotech. J. 41: 990-993.

Haydon, P.R. & Graf, D.L. (1986): Studies of smectite membrane behavior: Temperature dependence, 20-180° C.- Geochim. Cosmochim. Acta 50: 115-121.

Horseman, S.T.; Higgo, J.J.W.; Alexander, J. & Harrington, J.F. (1996): Water, gas and solute movement through argillaceous media.- Report CC-96-1; Nuclear Energy Agen.

Houben, G. & Treskatis, C. (2006): *Rehabilitation of water wells*.- 348 p.; New York (McGraw Hill) [in print].

Kahr, G. & Meier, L.P. (1996): Einfache Bestimmungsmethode des Kationenaustauschvermögens von Tonen mit Komplexverbindungen des Kupfer(II)-Ions mit Triethylentetramin und Tetraethylenpentamin.- In: Wolf, D., Starke, R. &, Kleeberg, R. (eds.), Berichte der DTTG, Freiberg, p. 122.

Keijzer, T.J.S. (2000): *Chemical osmosis in natural clayey material*.- Geologica Ultraiectina 196; Utrecht.

Kharaka, Y.K. & Berry, F.A.F. (1973): Simultaneous flow of water and solutes through geological membranes - I. Experimental investigation.- Geochim. Cosmochim. Acta 37: 2577-2603.

Krus, M. (1995): *Feuchtetransport- und Speicherkoeffizienten poröser mineralischer Baustoffe. Theoretische Grundlagen und neue Messtechniken*.- PhD thesis, University of Stuttgart, Germany.

Lueth, V.W. & Whitworth, T.M. (2001): A geologic membrane-microbial metabolism mechanism for the origin of the sedimentary copper deposit in the Pastura district, Guadelupe County, New Mexico.- New Mexico Geol. Soc. Guidebook 52nd Field Conf.: 333-340.

Malusis, M. A., Shackelford, C. D. & Olsen, H. W. (2001): A laboratory apparatus to measure chemico-osmotic efficiency coefficients for clay soils.- Geotechn. Testing J. ASTM, 24 (3): 229-242.

Meier, L.P. & Kahr, G. (1999) Determination of the cation exchange capacity (CEC) of clay minerals using the complexes of Copper (II) ion with Triethylenetetramine and Tretraethylenepentamine.- Clays and Clay Minerals 47: 386 - 388.

Neuzil, C.E. (1986): Groundwater flow in low-permeability environments.- Water Resources Res. 22 (8): 1163-1195.

Neuzil, C.E. (1993): How permeable are clays and shale?- Water Resources Res. 30 (2): 145-150.

Neuzil, C.E. (1994): Low fluid pressure within the Pierre shale: A transient response to erosion.- Water Resources Res. 29 (7): 2007-2020.

Neuzil, C.E. (1995): Abnormal pressures as hydrodynamic phenomena.- Am. J. Sci. 295: 742-786.

Neuzil, C.E. (2000): Osmotic generation of “anomalous” fluid pressures in geological environments.- Nature 403: 182-184.

Olsen, H.W. (1972): Liquid movement through kaolinite under hydraulic, electric, and osmotic gradients.- Am. Ass. Petrol. Geol. Bull. 56: 2022-2028.

Olsen, H.W. (1985): Osmosis: a cause of apparent deviation from Darcy’s law.- Can. Geotech. J. 22 (2): 238-241.

Prichett, W.C. (1980): Physical properties of shales and possible origin of high pressure.- Soc. Petr. Eng. J. 20 : 341-348.

Rübel, A.; Noseck, U.; Müller-Lyda, I.; Kröhn, K.-P. & Storck, R. (2004): *Konzeptioneller Umgang mit Gas im Endlager*.- GRS Report 205.

Soler, J. (2001): The effect of coupled transport phenomena in the Opalinus Clay and implications for radionuclide transport.- J. Contaminant Transport 53: 63-84.

Saindon, & Whitworth, T.M. (2006): Electrolyte-induced solute permeability effects in compacted smectite membranes.- Appl. Geochem. 9: 533-546.

Staverman, A.J. (1952): Non-equilibrium thermodynamics of membrane processes.- Transact. Faraday Soc. 48: 176-185.

Whitworth, T.M. & Fritz, S.J. (1994): Electrolyte-induced solute permeability effects in compacted smectite membranes.- Appl. Geochem. 9: 533-546.

Whitworth, T.M., Marinas, B.J. & Fritz, S.J. (1994): Isotopic fractionation and overall permeation of lithium by thin-film composite polyamide reverse osmosis membrane.- J. Membrane Sci. 88: 231-241.

Whitworth, T.M. & De Rosa, G. (1997): *Geologic membrane controls on saturated zone heavy metal transport*.- New Mexico Water Resources Research Institute Technical Completion Report 1423923, 79 p..

Whitworth, T.M., Haneberg, W.C., Mozley, P.S. & Goodwin, L.B. (1999): Solute-sieving-induced calcite precipitation on pulverized quartz sand: experimental results and implications for the membrane behavior of fault gouge.- Faults and subsurface fluid flow in the shallow crust.- Geophys. Monogr. 113: 149-157 (Am. Geophys. Union).

Wittenberg, A. & Schwarz-Schampera, U. (2005): Advanced Investigations of Unconventional Uranium and Thorium Deposits by In-Situ µ-EDXRF analysis.- in: Merkel, B. & Hasche-Berger, A. (eds.): Uranium in the Environment - Mining impact and consequences.- Int. Conf. Uranium Mining Hydrogeol. IV: 159-164; Berlin (Springer).

Annex

Annex A

A 1: Experiments at flow rate Q = 2 ml/min

A 2: Experiments at flow rate Q = 5 ml/min

A 3: Experiments at flow rate Q = 1 ml/min

A 4: Experiments at flow rate Q = 3 ml/min

A 5: Experiments at flow rate Q = 10 ml/min

Annex B

B 1: Experimental data for experiments with Q_{hyp} = 2 ml/min

B 2: Experimental data for experiments with Q_{hyp} = 5 ml/min

Annex C

C 1: Pore size distribution for samples from experiments with Q_{hyp} = 2 ml/min

C 2: Pore size distribution for samples from experiments with Q_{hyp} = 5 ml/min

C 3: Pore size distribution for samples from experiments with Q_{hyp} = 1 ml/min

C 4: Pore size distribution for samples from experiments with Q_{hyp} = 3 ml/min

C 5: Pore size distribution for samples from experiments with Q_{hyp} = 10 ml/min

A 1: Experiments at flow rate Q = 2 ml/min

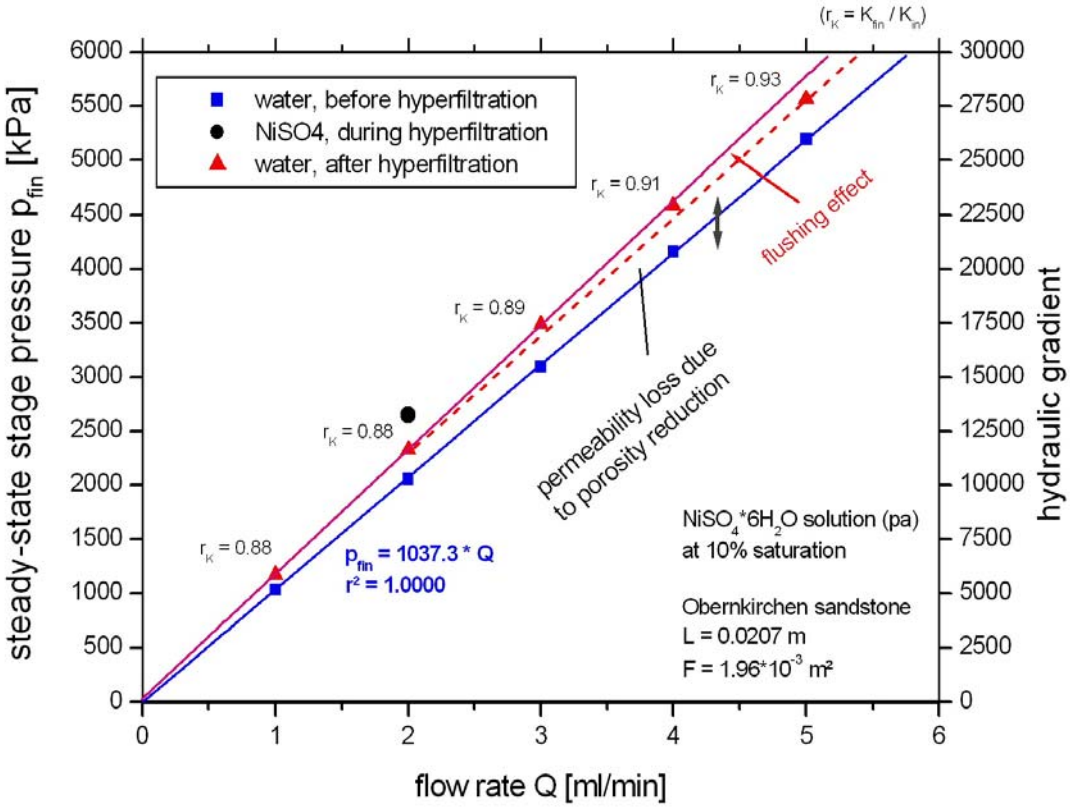

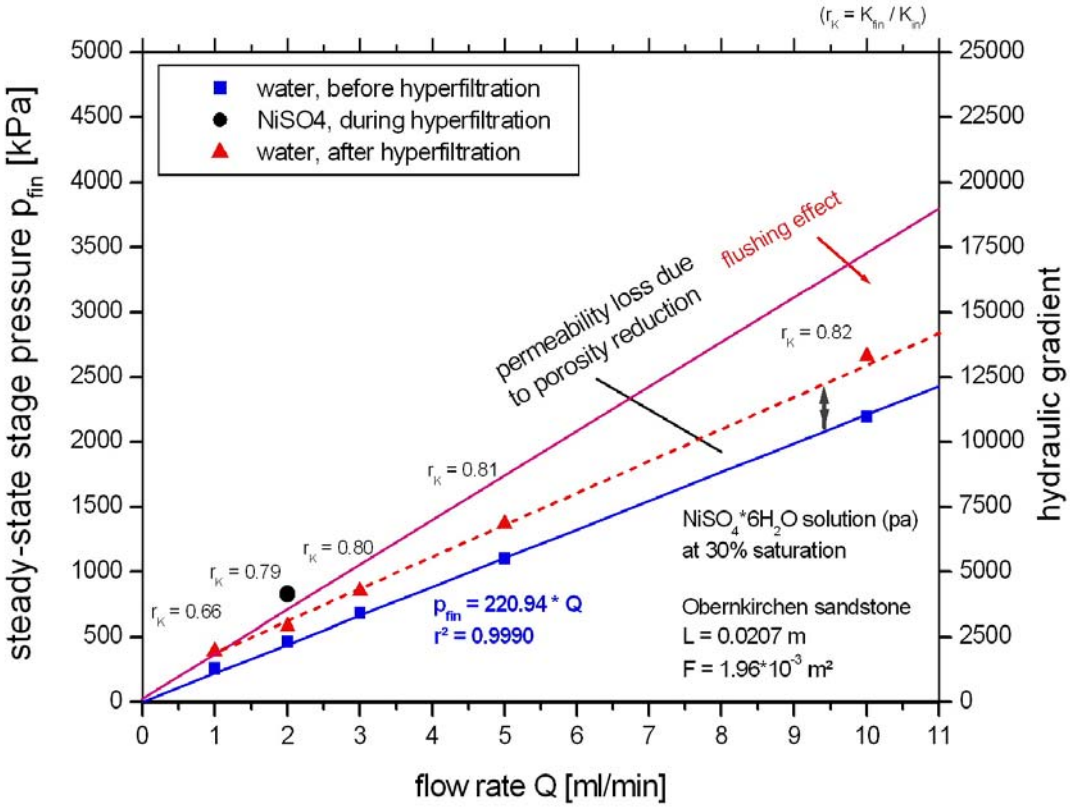

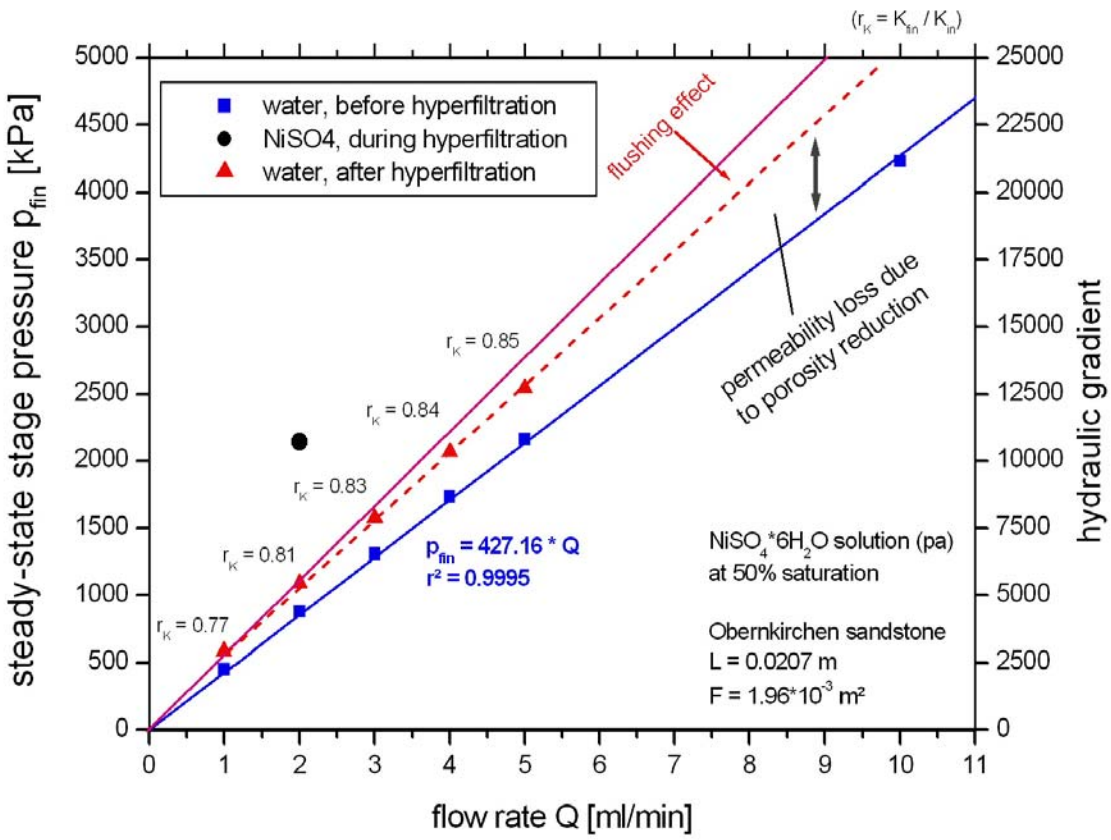
(r_K = K_fin / K_in)
water, before hyperfiltration
NiSO4, during hyperfiltration
water, after hyperfiltration
flushing effect
permeability loss due to porosity reduction
r_K = 0.85
r_K = 0.84
r_K = 0.83
r_K = 0.81
r_K = 0.77
p_fin = 427.16 * Q
r² = 0.9995
NiSO4*6H2O solution (pa) at 50% saturation
Obernkirchen sandstone
L = 0.0207 m
F = 1.96*10^-3 m²
steady-state stage pressure p_fin [kPa]
hydraulic gradient
flow rate Q [ml/min]

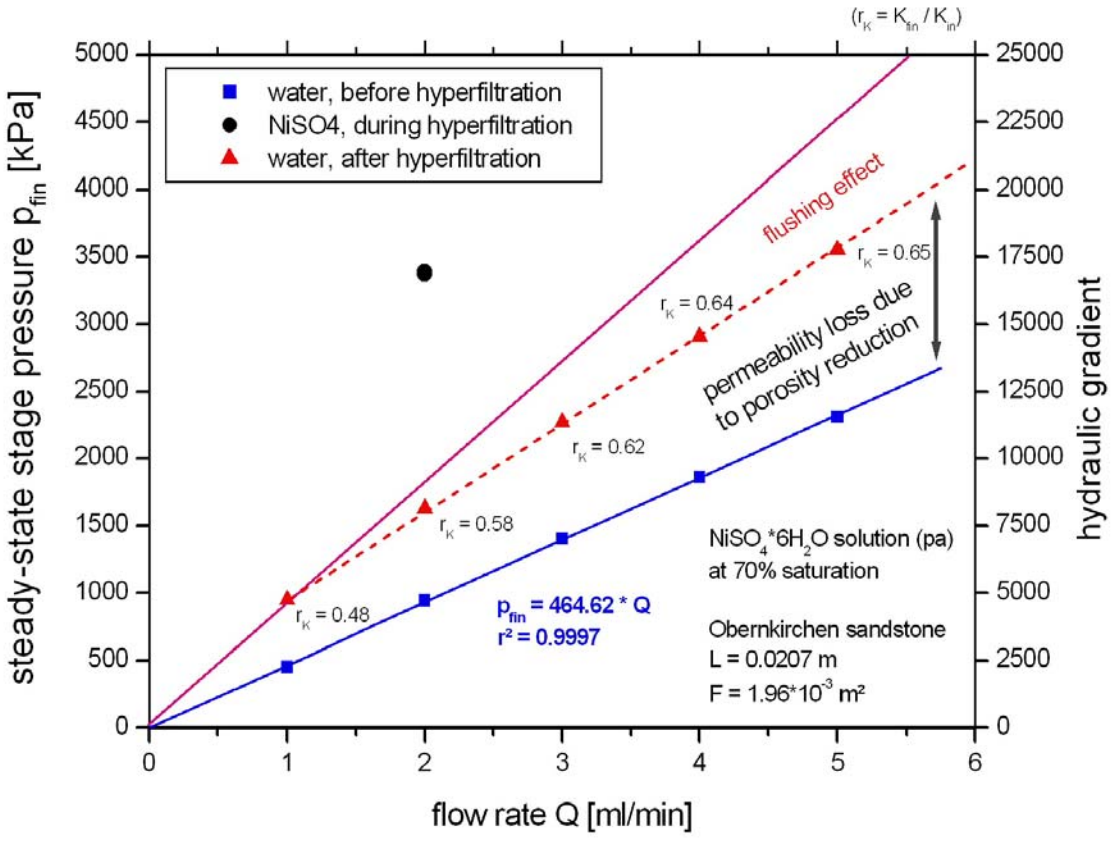
(r_K = K_fin / K_in)
water, before hyperfiltration
NiSO4, during hyperfiltration
water, after hyperfiltration
flushing effect
permeability loss due to porosity reduction
r_K = 0.65
r_K = 0.64
r_K = 0.62
r_K = 0.58
r_K = 0.48
p_fin = 464.62 * Q
r² = 0.9997
NiSO4*6H2O solution (pa) at 70% saturation
Obernkirchen sandstone
L = 0.0207 m
F = 1.96*10^-3 m²
steady-state stage pressure p_fin [kPa]
hydraulic gradient
flow rate Q [ml/min]

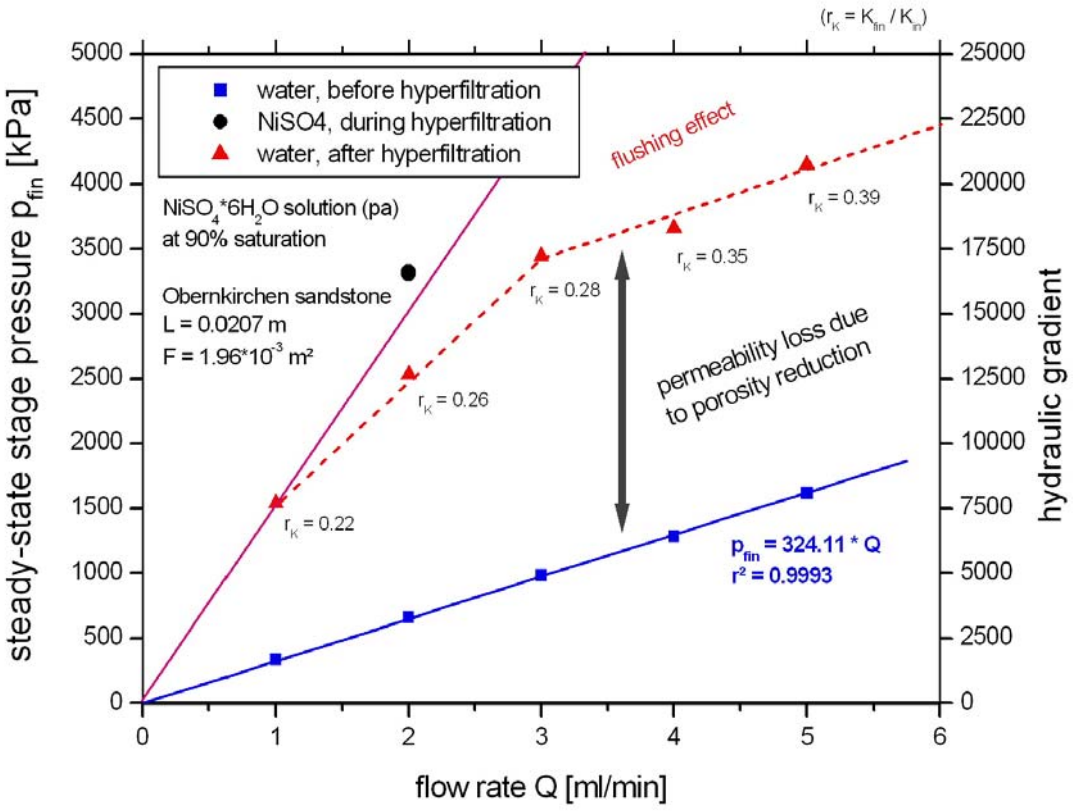
($r_K = K_{fin} / K_{in}$)
water, before hyperfiltration
NiSO4, during hyperfiltration
water, after hyperfiltration
flushing effect
$NiSO_4*6H_2O$ solution (pa)
at 90% saturation
Obernkirchen sandstone
L = 0.0207 m
F = 1.96*10^{-3} m²
r_K = 0.22
r_K = 0.26
r_K = 0.28
r_K = 0.35
r_K = 0.39
permeability loss due
to porosity reduction
p_{fin} = 324.11 * Q
r^2 = 0.9993
steady-state stage pressure p_{fin} [kPa]
hydraulic gradient
flow rate Q [ml/min]
0
500
1000
1500
2000
2500
3000
3500
4000
4500
5000
2500
5000
7500
10000
12500
15000
17500
20000
22500
25000
1
2
3
4
5
6

A 2: Experiments at flow rate Q = 5 ml/min

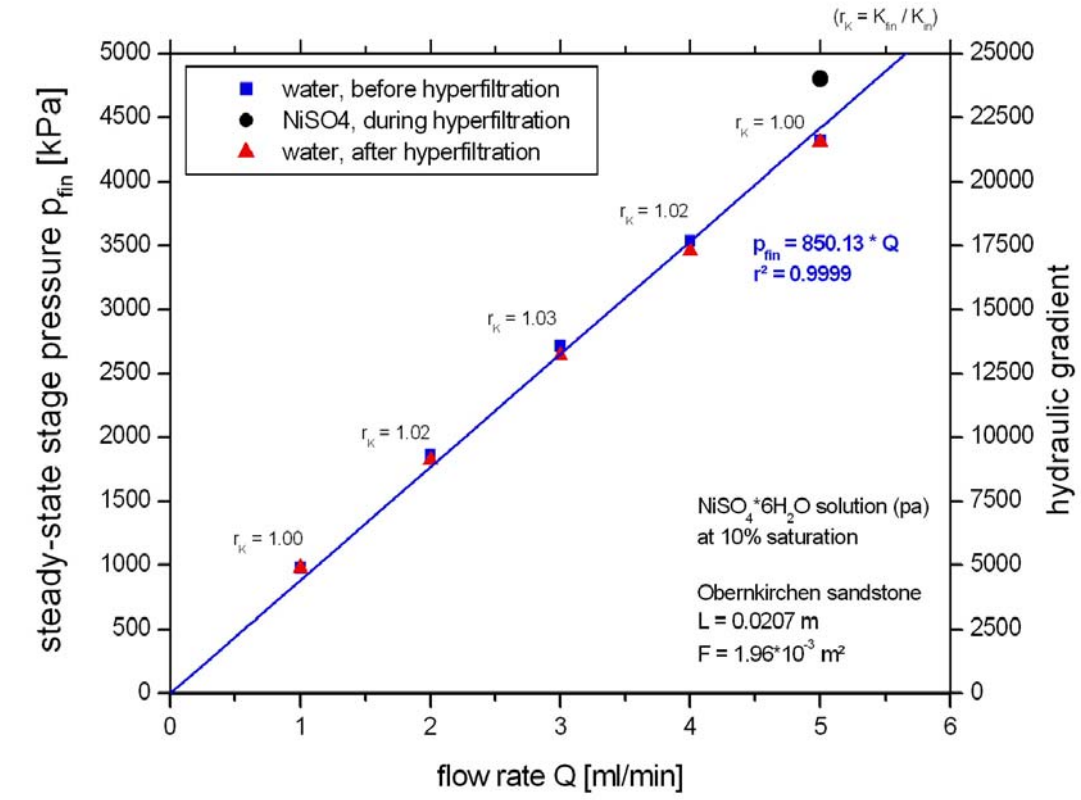

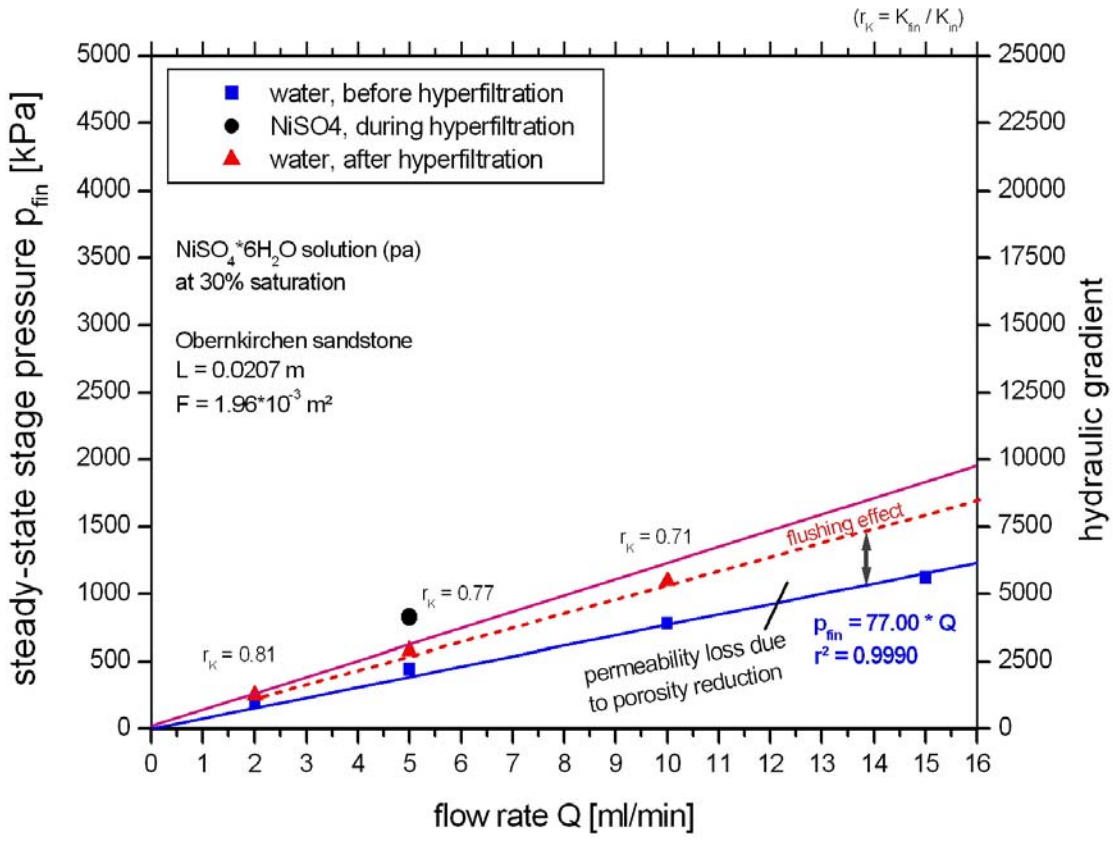

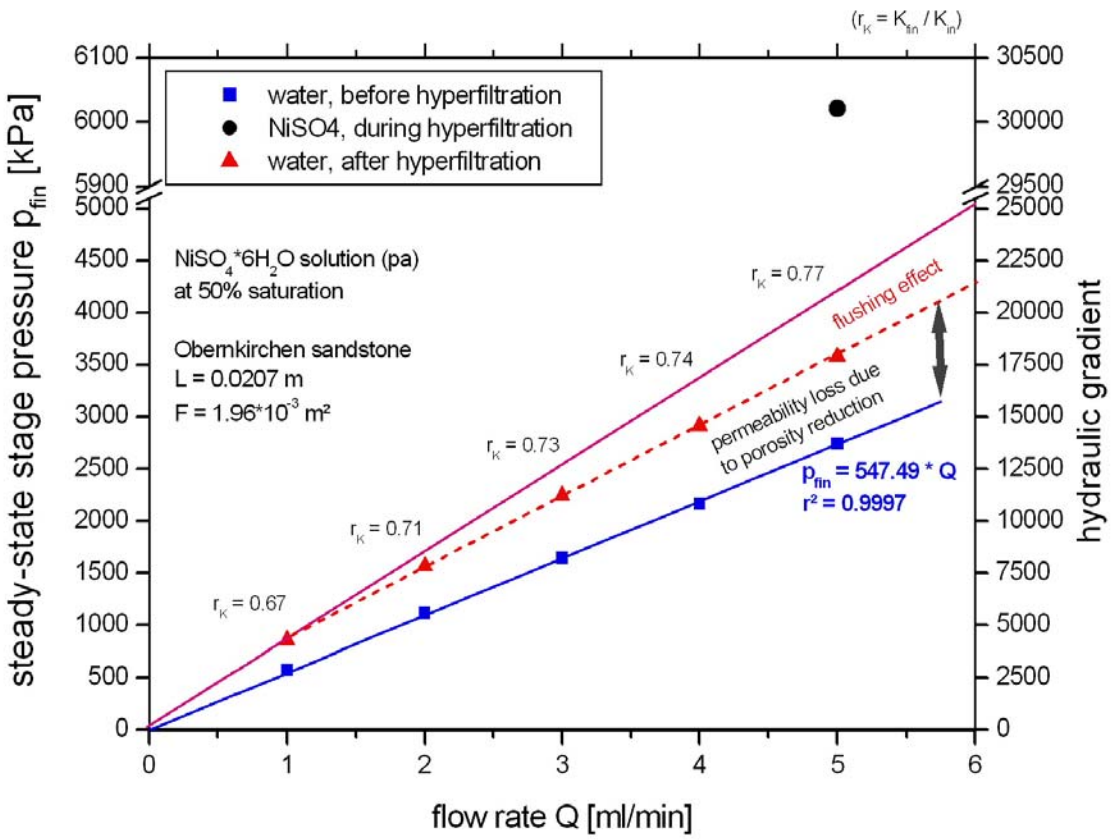
(r_K = K_fin / K_in)
water, before hyperfiltration
NiSO4, during hyperfiltration
water, after hyperfiltration
NiSO4*6H2O solution (pa)
at 50% saturation
Obernkirchen sandstone
L = 0.0207 m
F = 1.96*10-3 m²
r_K = 0.67
r_K = 0.71
r_K = 0.73
r_K = 0.74
r_K = 0.77
flushing effect
permeability loss due to porosity reduction
p_fin = 547.49 * Q
r² = 0.9997
steady-state stage pressure p_fin [kPa]
hydraulic gradient
flow rate Q [ml/min]

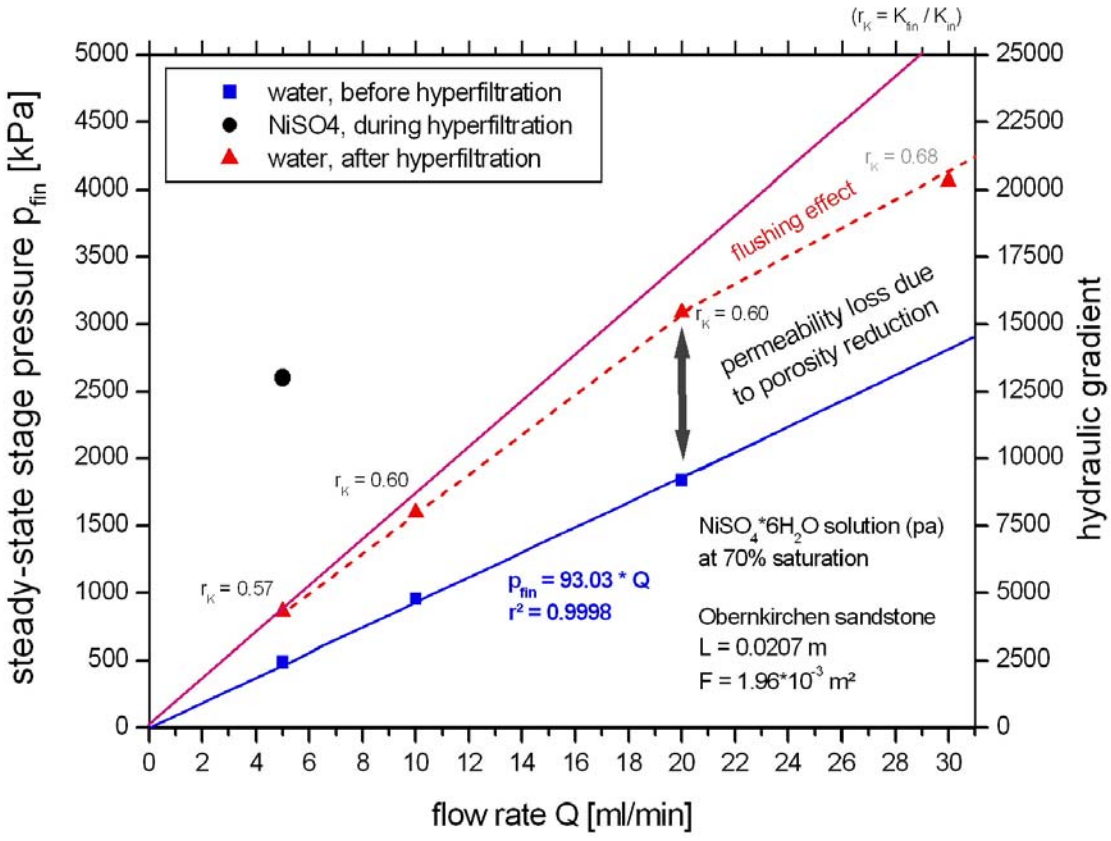
(r_K = K_fin / K_in)
water, before hyperfiltration
NiSO4, during hyperfiltration
water, after hyperfiltration
r_K = 0.57
r_K = 0.60
r_K = 0.60
r_K = 0.68
flushing effect
permeability loss due to porosity reduction
p_fin = 93.03 * Q
r² = 0.9998
NiSO4*6H2O solution (pa)
at 70% saturation
Obernkirchen sandstone
L = 0.0207 m
F = 1.96*10-3 m²
steady-state stage pressure p_fin [kPa]
hydraulic gradient
flow rate Q [ml/min]

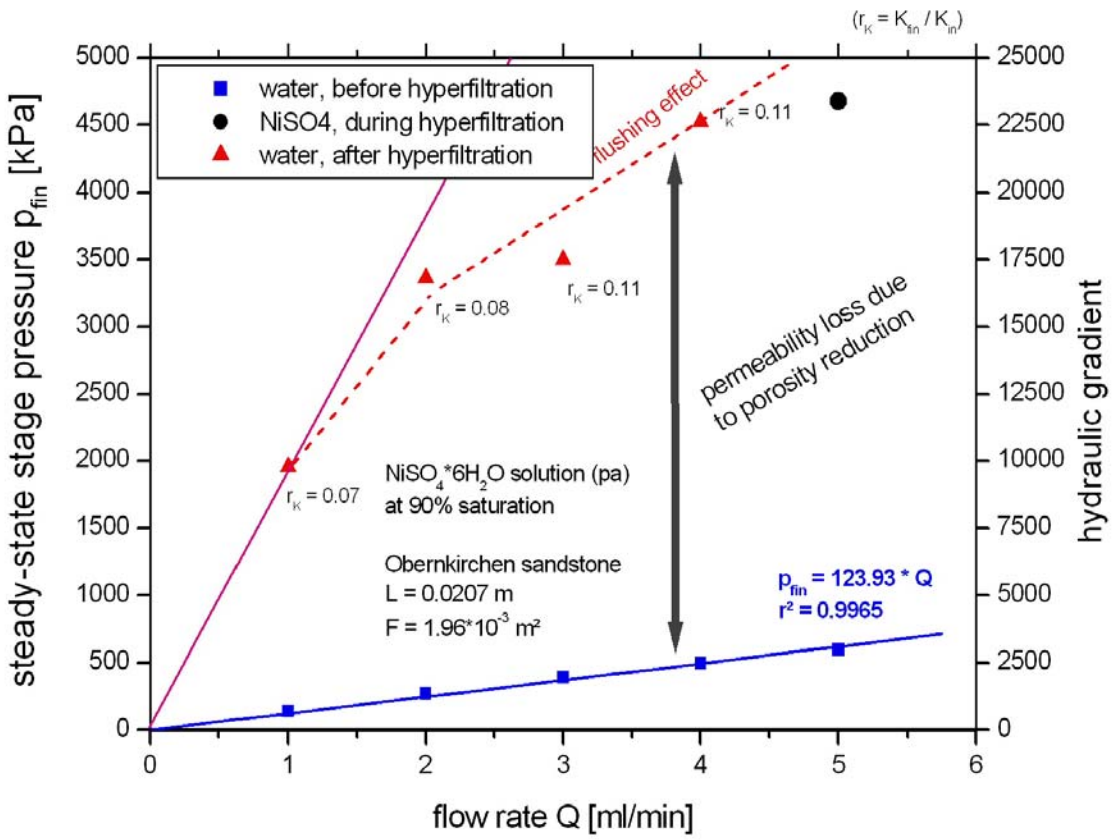
($r_K = K_{fin} / K_{in}$)
water, before hyperfiltration
NiSO4, during hyperfiltration
water, after hyperfiltration
flushing effect
r_K = 0.11
r_K = 0.08
r_K = 0.11
r_K = 0.07
permeability loss due to porosity reduction
$NiSO_4$*6H_2O solution (pa) at 90% saturation
Obernkirchen sandstone
L = 0.0207 m
F = 1.96*10^{-3} m²
p_{fin} = 123.93 * Q
r^2 = 0.9965
steady-state stage pressure p_{fin} [kPa]
hydraulic gradient
flow rate Q [ml/min]
0
500
1000
1500
2000
2500
3000
3500
4000
4500
5000
7500
10000
12500
15000
17500
20000
22500
25000
1
2
3
4
5
6

A 3: Experiments at flow rate Q = 1 ml/min

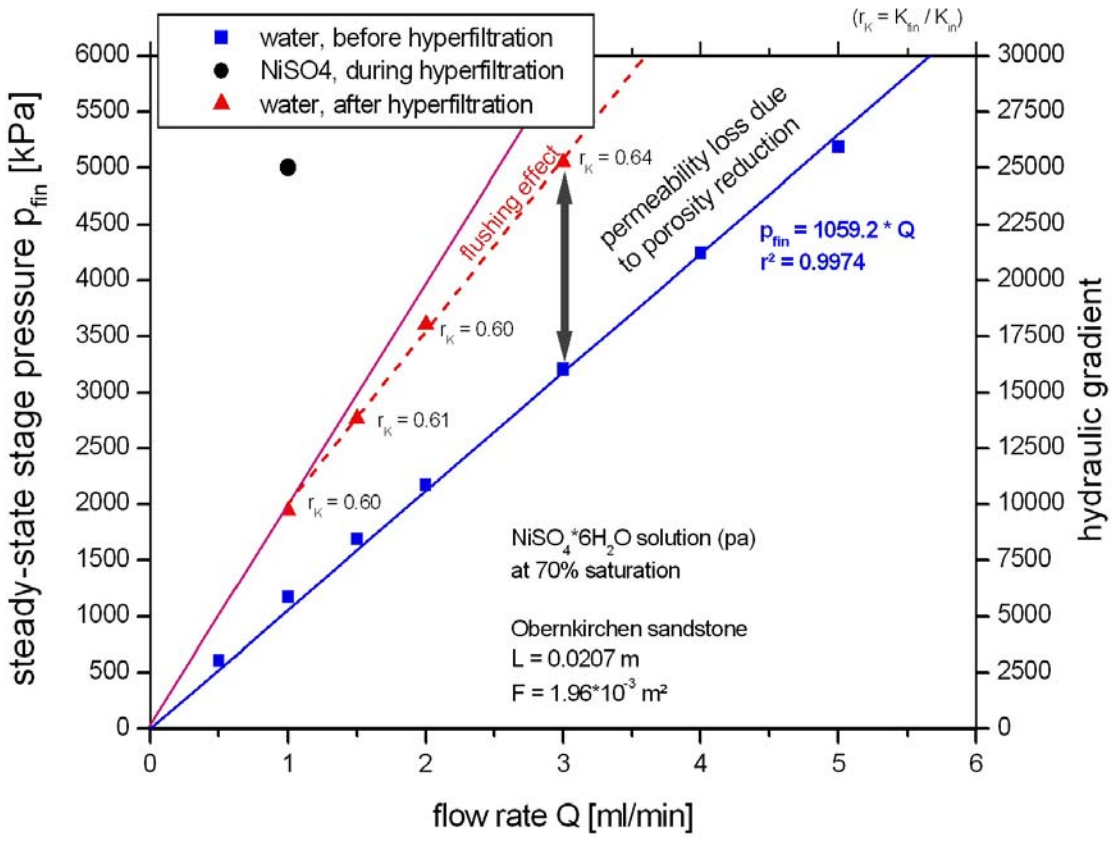

A 4: Experiments at flow rate Q = 3 ml/min

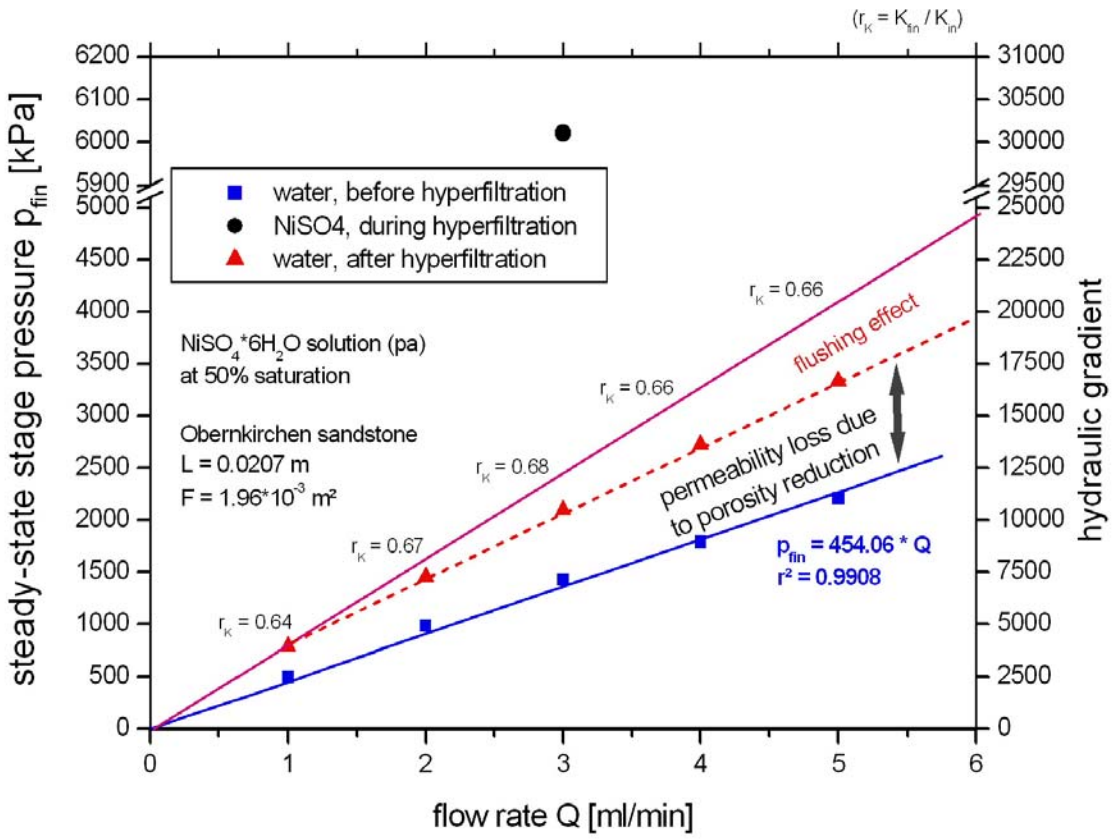

A 5: Experiments at flow rate Q = 10 ml/min

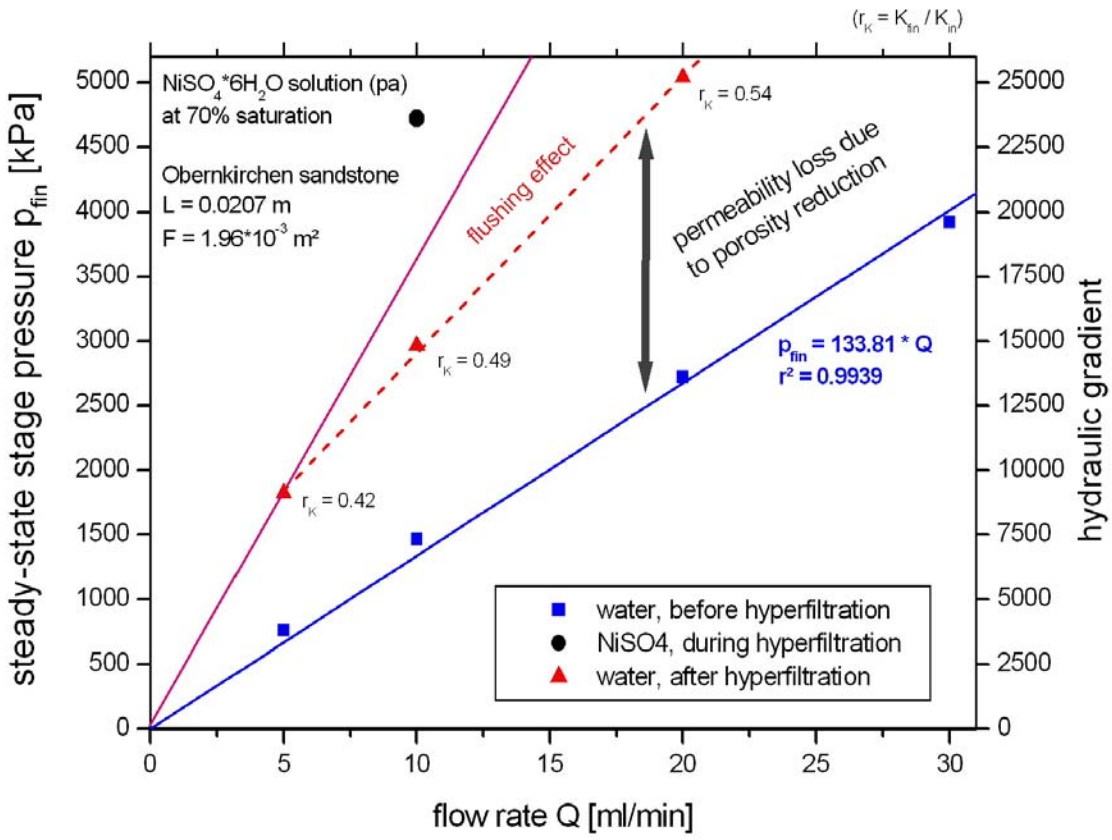

Annex B

B 1: Experimental data for experiments with Q_{hyp} = 2 ml/min

	experimental phase	sample mass M [g]	bulk density ρ [g/cm³]	stage pressure p [kPa]	hydraulic gradient I [-]	conductivity kf [m/s]	intrinsic permeability k [m²]	Reynolds number Re [-]	correlation coefficient r²	reflection coefficient σ_{NiSO4} [-]
10% $NiS0_4$, 2 ml/min	flushing	86.6608	2.1973	2060.7	10470	1.62E-09	1.52E-16	5.16E-05	1.0000	
	hyperfiltration			2649.3	12639	1.34E-09	1.18E-16	5.16E-05		
	re-flushing	87.7188		2331.3	11844.5	1.43E-09	1.34E-16	5.16E-05		0.042
30% $NiS0_4$, 2 ml/min	flushing	84.8338	2.1230	461.8	2354.6	7.19E-09	6.74E-16	5.15E-05	0.9993	
	hyperfiltration			828.2	3533.6	4.79E-09	3.76E-16	5.15E-05		
	re-flushing	85.6436		582.2	2968.3	5.70E-09	5.35E-16	5.15E-05		0.003
50% $NiS0_4$, 2 ml/min	flushing	86.3708	2.1994	879.2	4482.7	3.79E-09	3.55E-16	5.17E-05	0.9997	
	hyperfiltration			2142.3	8243.3	2.06E-09	1.46E-16	5.17E-05		
	re-flushing	86.6724		1089.2	5553.4	3.06E-09	2.87E-16	5.17E-05		0.055
70% $NiS0_4$, 2 ml/min	flushing	87.5413	2.2262	941.8	4801.7	3.54E-09	3.32E-16	5.17E-05	0.9997	
	hyperfiltration			3381.8	11850.3	1.43E-09	9.23E-17	5.17E-05		
	re-flushing	88.1899		1626.3	8291.5	2.05E-09	1.92E-16	5.17E-05		0.038
90% $NiS0_4$, 2ml/min	flushing	85.8607	2.1836	663.2	3379.6	5.02E-09	4.71E-16	5.16E-05	0.9993	
	hyperfiltration			3318.3	10668.7	1.59E-09	9.41E-17	5.16E-05		
	re-flushing	86.5436		2531.7	12901.2	1.31E-09	1.23E-16	5.16E-05		0.089

B 2: Experimental data for experiments with Q_{hyp} = 5 ml/min

	experimental phase	sample mass M [g]	bulk density ρ [g/cm³]	stage pressure p [kPa]	hydraulic gradient I [-]	conductivity kf [m/s]	intrinsic permeability k [m²]	Reynolds number Re [-]	correlation coefficient r^2	reflection coefficient σ_{NiSO4} [-]
10% $NiS0_4$, 5 ml/min	flushing	86.1596	2.1885	4319.4	22011.5	1.93E-09	1.81E-16	1.29E-04	0.9976	
	hyperfiltration			4802.5	22979.8	1.84E-09	1.62E-16	1.29E-04		
	re-flushing	86.2452		4229.3	21552.4	1.97E-09	1.84E-16	1.29E-04		0.047
30% $NiS0_4$, 5 ml/min	flushing	84.4131	2.0946	444.2	2242.3	1.86E-08	1.75E-15	1.27E-04	0.9850	
	hyperfiltration			824.8	3484.1	1.20E-08	9.41E-16	1.27E-04		
	re-flushing	84.7354		579.2	2923.8	1.43E-08	1.34E-15	1.27E-04		0.029
50% $NiS0_4$, 5 ml/min	flushing	86.0664	2.2006	2744.4	14048.5	3.02E-09	2.83E-16	1.29E-04	0.9993	
	hyperfiltration			5588.4	21590.1	1.97E-09	1.39E-16	1.29E-04		
	re-flushing	86.4964		3576.3	18307	2.32E-09	2.17E-16	1.29E-04		0.015
70% $NiS0_4$, 5ml/min	flushing	84.1300	2.1347	488.8	2483.5	1.71E-08	1.60E-15	1.29E-04	0.9998	
	hyperfiltration			2705.2	9446.2	4.49E-09	2.90E-16	1.29E-04		
	re-flushing	/		863.8	4388.7	9.67E-09	9.10E-16	1.29E-04		0.0003
90% $NiS0_4$, 5ml/min	flushing	83.9920	2.1448	593.8	3039.7	1.39E-08	1.31E-15	1.29E-04	0.9914	
	hyperfiltration			4674.7	15097.6	2.81E-09	1.66E-16	1.29E-04		
(4 ml/min)	re-flushing	84.4353		4520.8	23141.9	1.47E-09	1.37E-16	1.29E-04		0.025

Annex C

C 1: Pore size distribution for samples from experiments with Q_{hyp} = 2 ml/min

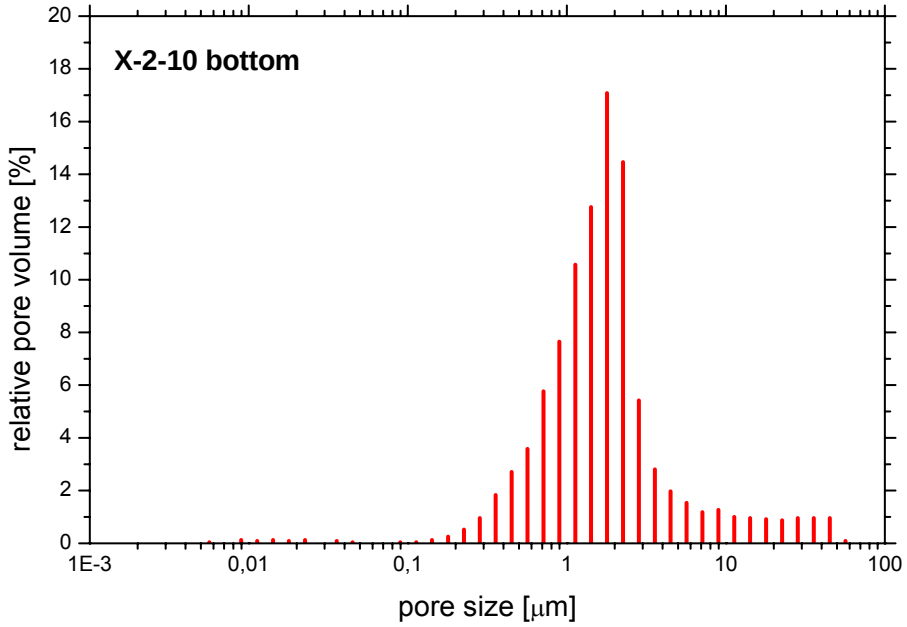

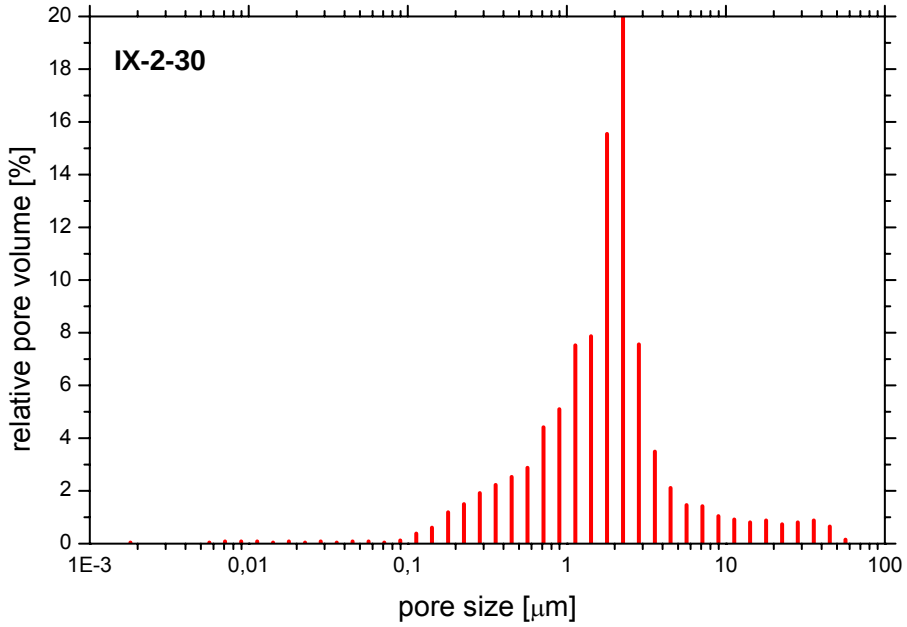

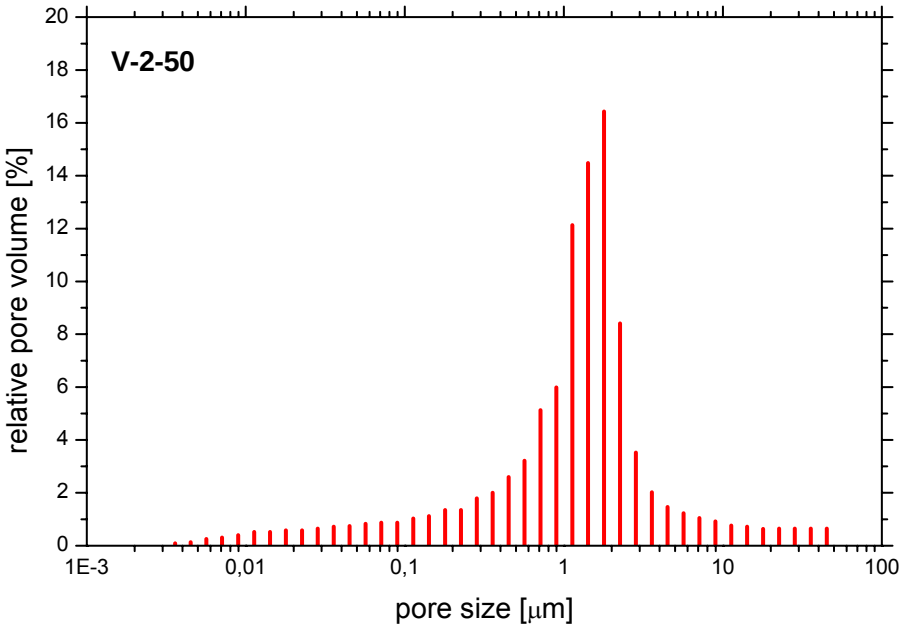
V-2-50
relative pore volume [%]
pore size [μm]
0
2
4
6
8
10
12
14
16
18
20
1E-3
0,01
0,1
1
10
100

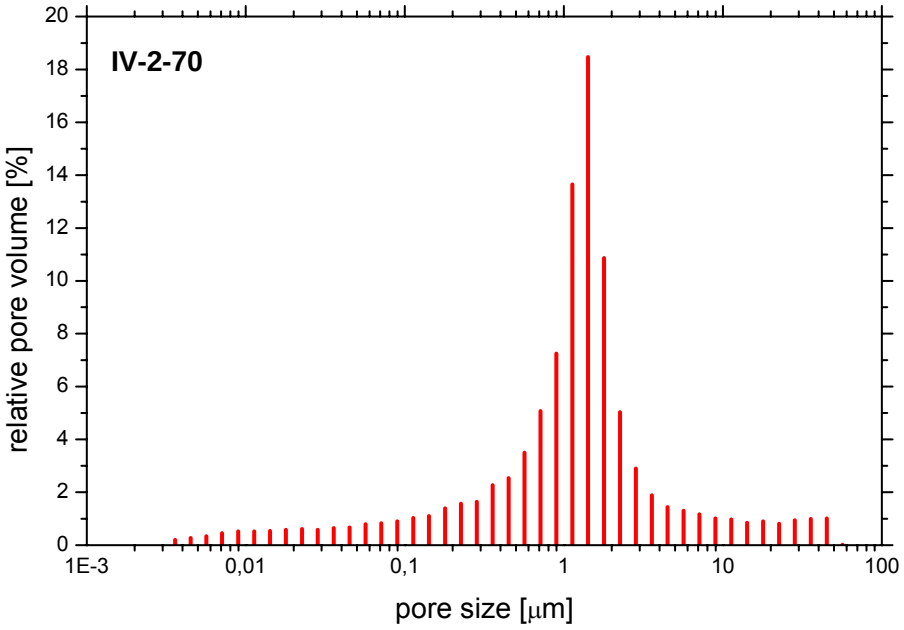
IV-2-70
relative pore volume [%]
pore size [μm]
0
2
4
6
8
10
12
14
16
18
20
1E-3
0,01
0,1
1
10
100

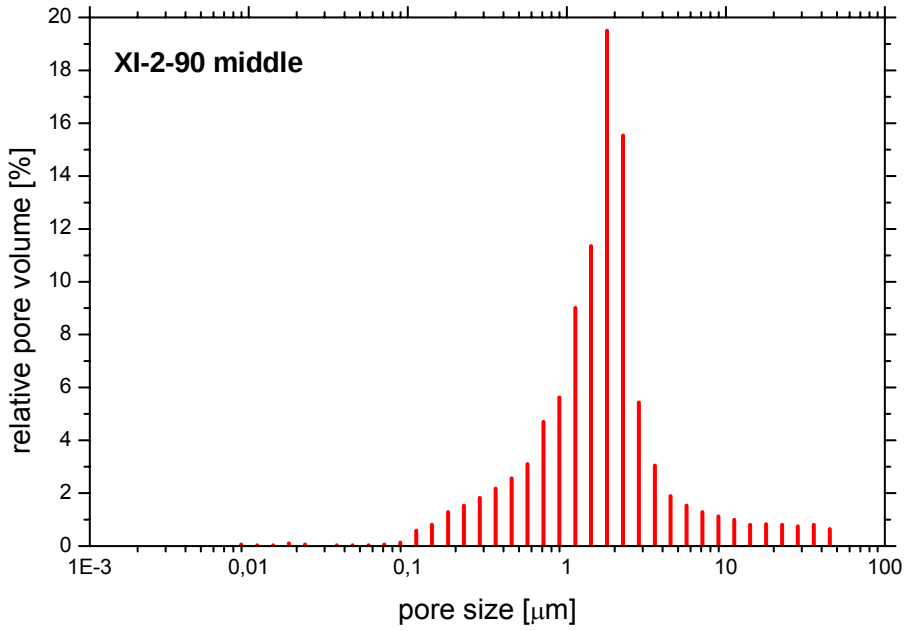
XI-2-90 middle
relative pore volume [%]
pore size [μm]
0
2
4
6
8
10
12
14
16
18
20
1E-3
0,01
0,1
1
10
100

C 2: Pore size distribution for samples from experiments with Q_{hyp} = 5 ml/min

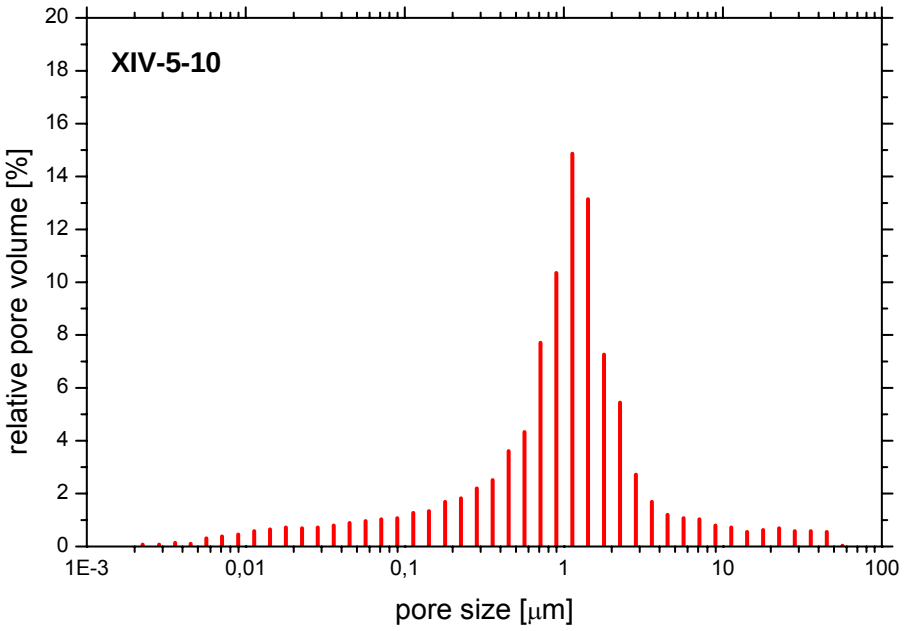

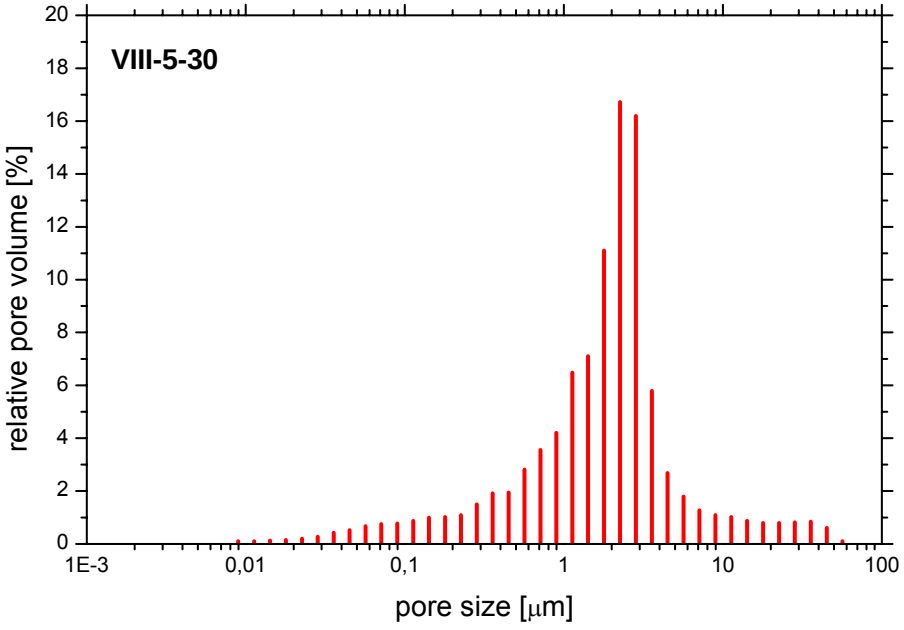

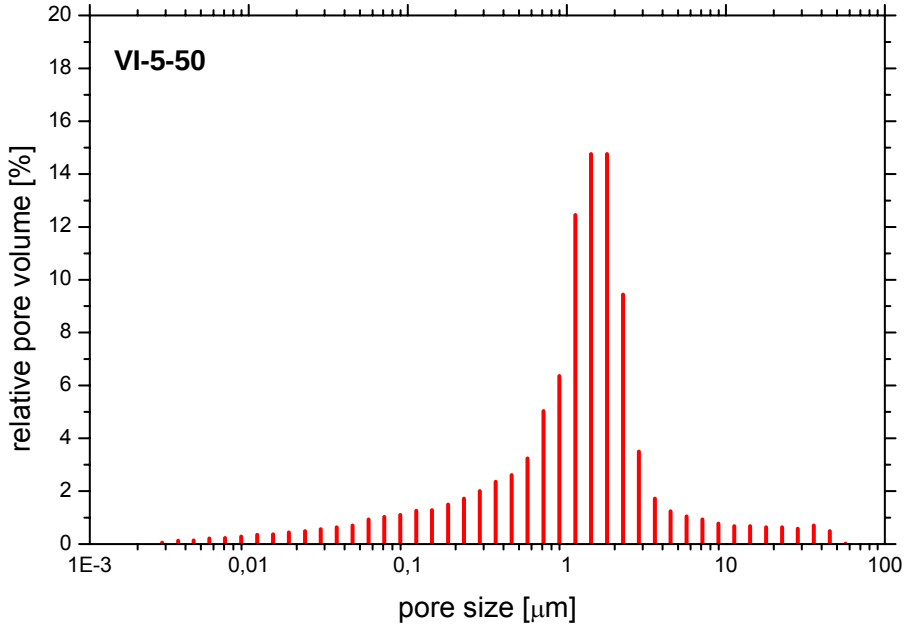
VI-5-50
relative pore volume [%]
pore size [μm]
0
2
4
6
8
10
12
14
16
18
20
1E-3
0,01
0,1
1
10
100

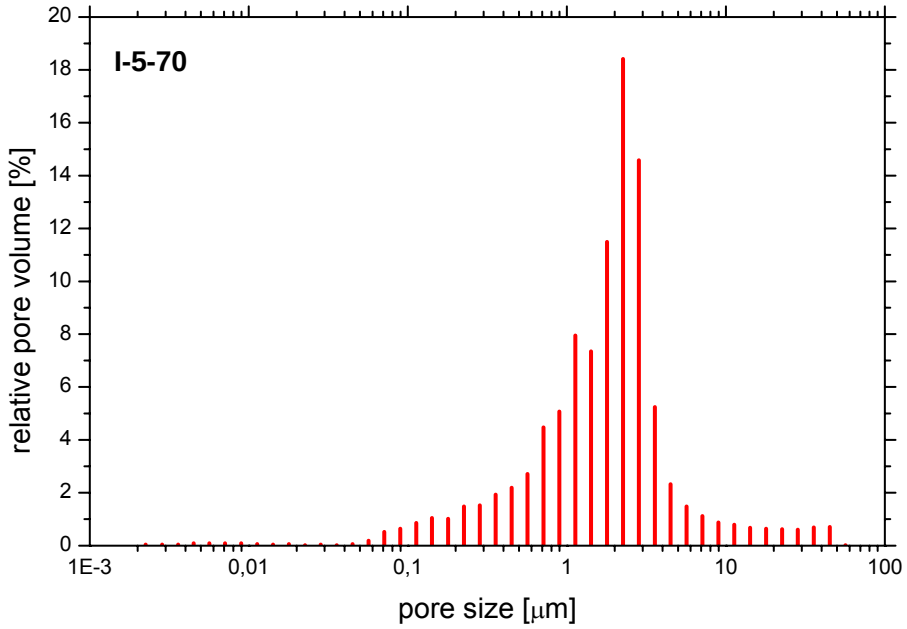
I-5-70
relative pore volume [%]
pore size [μm]
0
2
4
6
8
10
12
14
16
18
20
1E-3
0,01
0,1
1
10
100

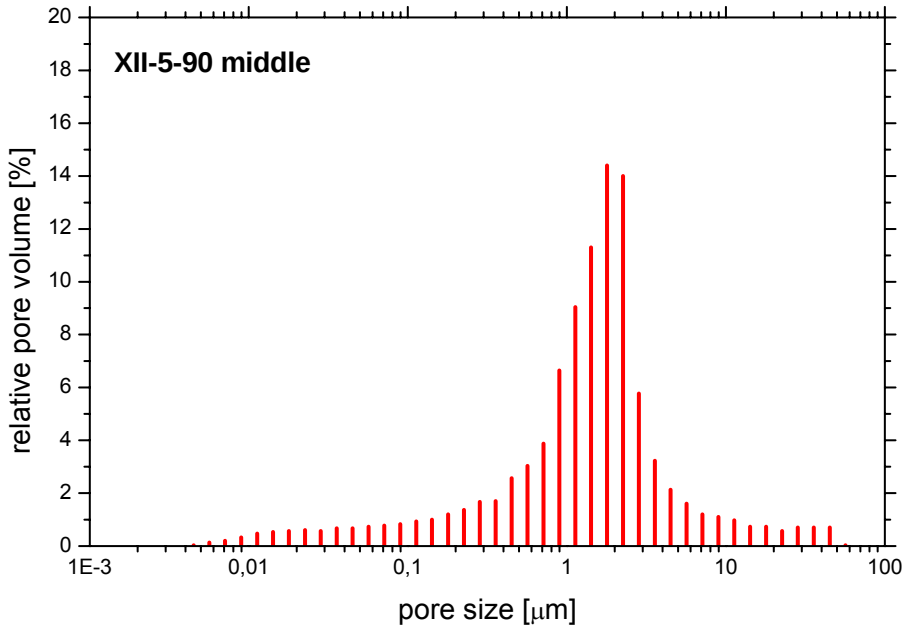
XII-5-90 middle
relative pore volume [%]
pore size [μm]
0
2
4
6
8
10
12
14
16
18
20
1E-3
0,01
0,1
1
10
100

C 3: Pore size distribution for samples from experiments with Q_{hyp} = 1 ml/min

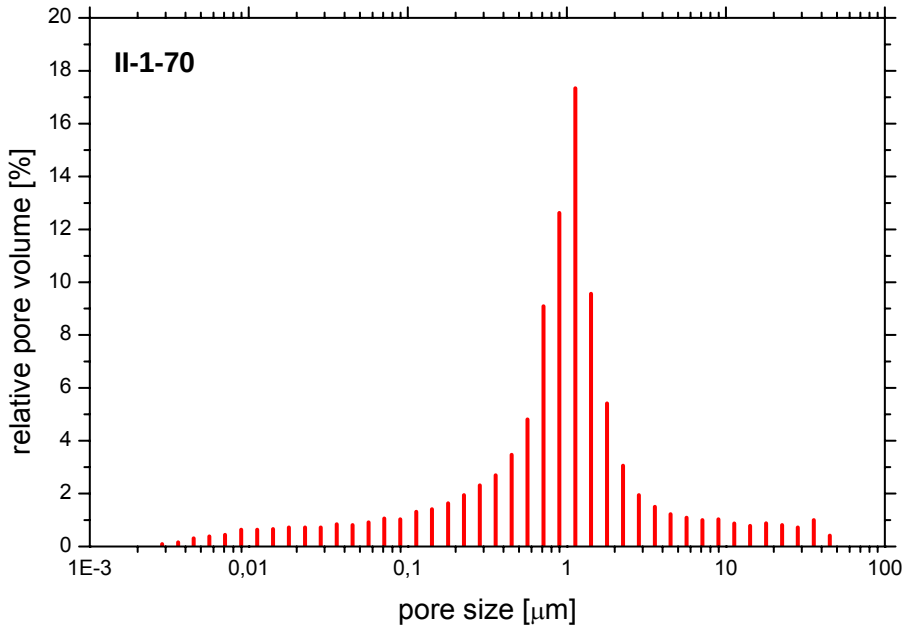

C 4: Pore size distribution for samples from experiments with Q_{hyp} = 3 ml/min

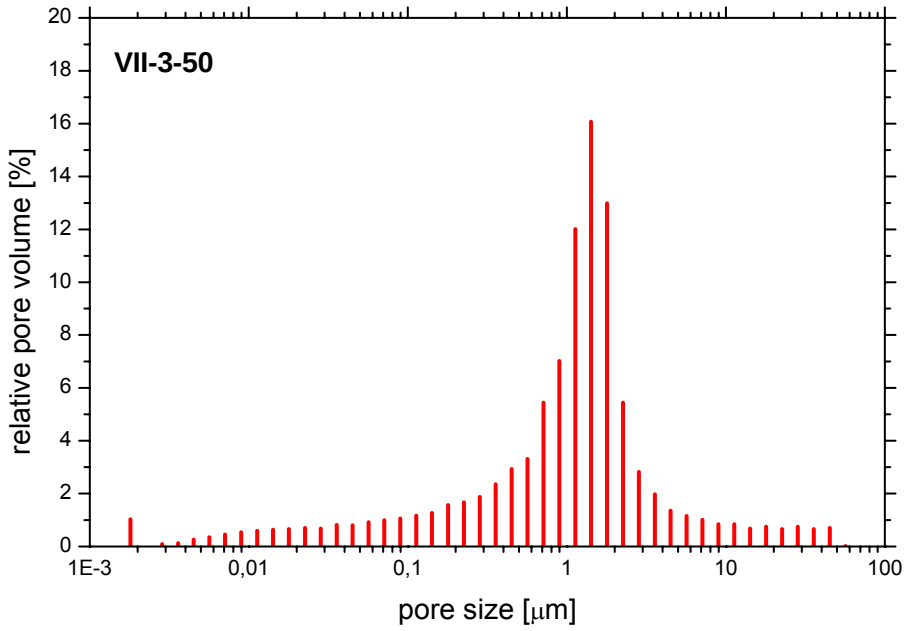

C 5: Pore size distribution for samples from experiments with Q_{hyp} = 10 ml/min